

Graphene-Cellulose Nanocrystals Composite as Electrode Material for Electrochemical Double-Layer Capacitors



Åbo Akademi University

Faculty of Science and Engineering

Hazzar Mohammed Reyes



Master's programme in Excellence in Analytical Chemistry

Degree project in Analytical Chemistry, 30 credits

Supervisor(s): Rose-Marie Latonen, Ph.D. (Åbo Akademi University),

Ann Laheäär, Ph.D. (University of Tartu)

Cosupervisor(s): Prof. Johan Bobacka (Åbo Akademi University)

MSc Sara Lund (Åbo Akademi University)

August, 2023

ABSTRACT

It has been a constant challenge to develop more sustainable and better-performing supercapacitors that meet the large-scale demands of hybrid electric vehicles, wearable microelectronics, and grid storage in the future. They require green, facile, and efficient production methods to realise their prospective applications. In this work, graphene-nanocellulose crystals (G-CNC) composites were evaluated as electrode active materials for symmetric, electrochemical double-layer capacitors (EDLCs). The G-CNC electrodes were fabricated through manual spray-coating of the composites, prepared by a green and facile high-shear, liquid-phase exfoliation of natural graphite flakes. The obtained G-CNC composites of high graphene ($>7 \text{ mg}\cdot\text{mL}^{-1}$) and CNC (11-32 % w/w) concentrations were identified to significantly reduce the composite's electronic conductivity, along with presence of partially exfoliated graphite in several dispersions. The G-CNC electrodes display decent energy storage capabilities, with an average specific capacitance of up to $\sim 40 \text{ F}\cdot\text{g}^{-1}$ in aqueous electrolyte solution (1.0 M NaClO_4). The 2D stacking arrangement of the graphene flakes in the G-CNC electrodes was determined to impede ion transport needed for double-layer capacitance formation. Low energy efficiencies ($<75 \%$) were obtained for these electrodes, which suggests that modifications in the G-CNC material, the electrode preparation, or the EDLC component materials are still needed for a better understanding of the G-CNC's full "capacity" as a promising material for energy storage applications.

ACKNOWLEDGEMENTS

I would like to thank everyone who have participated and supported the execution of this study, and more generally, at the stretch of my master's degree studies. First, thank you to my thesis supervisors for their guidance and patience. To Rose-Marie Latonen, for being always available and considerate of my inputs and ideas for this research. Our overall supervisor-supervisee rapport was positive and creative, an essential for a wonderful time doing research. To Ann Laheäär, many thanks for sharing her insights and expertise in energy storage research. We have all learned something new whenever we discuss with her, and hopefully the same goes for her. To Sara Lund, for her patience and for introducing me to research techniques which were relatively new to me. We have not just developed open communication, but also fostered a beautiful friendship. To Prof. Johan Bobacka, for his endless support to us EACH students, and for always lending an open ear regarding our concerns. Thank you, Johan, for the trust and consideration given to me on undertaking a relatively new topic within the Analytical Chemistry Group.

Next, I would like to dedicate this paragraph to those who provided support on matters outside the study. Thank you to the ÅAU Analytical Chemistry Group for making us feel welcome and for catering to our day-to-day activities in the lab. To Prof. Ivo Leito and Anu-Tearu-Ojakäär, our first-year experience in Tartu was lovely thanks to Ivo's admirable teaching styles and Anu's incessant concern for our welfare. I would also like to thank my fellow EACH-Åbo folks (Divisha, Ena, Juyeon, Merili, and Rodney), I'm so happy to have spent these past two years with you guys. The shared bonding moments and the endured hardships towards this endpoint will always be remembered. May we continue prospering in our life endeavours and strengthen our friendship after our master's journey, along with our other EACH folks. To my Turku CampusSport volleyball folks, our camaraderie is one of my best, helpful distractions from the stress of courses and thesis work. You guys made me realise the importance of study-life balance, so cheers to that and to our future adventures!

Finally, I will express gratitude to my Ma, Myrna, for her endless love, support, and wisdom. I am forever changed as a person because of this embarking outside of my comfort zone, and you are one of those who have shaped my identity and mindset. All these acknowledgements go

with my expression of optimism for what is in store for us in the future, and I am sure it will be super! The universe is immense and offers a lot of possibilities, and just by being part of its existence is something that is worth reminding every day. Whatever it brings upon you is worth accepting whole-heartedly. *Amor fati in omne tempus.*

Cheers!

TABLE OF CONTENTS

ABSTRACT	<i>i</i>
ACKNOWLEDGEMENTS	<i>ii</i>
TABLE OF CONTENTS	<i>iv</i>
LIST OF ACRONYMS, ABBREVIATIONS, AND UNITS	<i>vi</i>
1. INTRODUCTION	1
2. THEORY	3
2.1 Supercapacitors	3
2.2 Graphene	8
2.3 Nanocellulose	11
2.4 Material Characterisation Techniques	13
2.4.1 UV-Visible Spectroscopy	13
2.4.2 Raman Spectroscopy	14
2.4.3 Four-Point Probe Technique	15
2.5 Electrochemical Characterisation Techniques	16
2.5.1 Cyclic Voltammetry	16
2.5.2 Electrochemical Impedance Spectroscopy.....	18
2.5.3 Galvanostatic Charge-Discharge.....	21
3. METHODOLOGY	24
3.1 Preparation of G-CNC Dispersion	24
3.2 Preparation of G-CNC Electrodes	24
3.3 Physico-chemical Characterisation	25
3.3.1 Raman Spectroscopy.....	25
3.3.2 Thermogravimetric Analysis	25
3.3.3 Scanning Electron Microscopy and Elemental Analysis	26
3.3.4 Electrical Conductivity	26
3.4 Electrochemical Characterisation	27
3.4.1 Three-electrode system	27
3.4.2 Two-electrode system	27
4. RESULTS AND DISCUSSION	29
4.1 Preparation of Graphene-CNC Composite	29
4.2 Physico-chemical Characterisation	32
4.2.1 Evaluation of Quality of Exfoliated Graphene Sheets	32
4.2.2 Estimation of Relative Amount of Graphene and CNC.....	34
4.2.3 Surface Morphology and Elemental Composition.....	37
4.2.4 Determination of Electrical Conductivity	43

4.3 Electrochemical Properties of the G-CNC composites	44
4.3.1 Cyclic Voltammetry	44
4.3.2 Galvanostatic Charge-Discharge.....	50
4.3.3 Electrochemical Impedance Spectroscopy.....	54
5. CONCLUSIONS AND OUTLOOK	58
REFERENCES	60
APPENDIX.....	70
A. G-CNC Dispersion Preparation	70
B. G-CNC Electrode Preparation.....	71
C. Physico-chemical Characterisations of G-CNC Composite	72
D. Electrochemical Characterisations of G-CNC Electrodes	79

LIST OF ACRONYMS, ABBREVIATIONS, AND UNITS

% : percentage	24
$\times g$: Relative centrifugal force	24
$\frac{\Delta t}{\Delta V}$: Slope from the discharge curve	22
ΔV : potential difference.....	5
$^{\circ}C$: degrees Celsius.....	24
μA : microAmpere.....	26
μL : microlitres.....	25
μm : micrometre	27
2D : two-dimensional	8
3D : three-dimensional	13
A: Ampere	14
$A \cdot g^{-1}$: Ampere per gram	28
AC : Alternative Current	18
A_{CV} : area under CV curve	17
AFM : Atomic Force Microscopy	27
Ag : Silver	27
AgCl : Silver Chloride.....	27
Ar : Argon	25
B : Boron	10
b : Cell path length	14
c : Concentration of sample.....	14
C_{ideal} : Ideal double-layer capacitance	20
cm : centimetre	16
cm^{-1} : Inverse centimetre	14
cm^2 : Square centimetre	25
CNCs : Cellulose Nanocrystals	12
CV : Cyclic Voltammetry	16
CVD : Chemical Vapour Deposition	9
DC : Direct Current	28
E : Energy density	5
EDLCs : Electrochemical Double-Layer Capacitors	2
EDX : Energy-Dispersive X-ray Spectroscopy.....	26
EIS : Electrochemical Impedance Spectroscopy.....	18
ETD : Everhart-Thornley Detector.....	26
F : Farads.....	5
f_1 : Finite thickness correction factor	16
f_2 : Finite thickness correction factor	16
GCD : Galvanostatic Charge-Discharge	21
G-CNC: Graphene-Cellulose Nanocrystals	2
GO : Graphene Oxide.....	9
h : hour	5
Hz : Hertz	18
I : Current	5

IEA : International Energy Agency.....	1
IHP: Inner Helmholtz Plane	4
IoT : Internet of Things	1
iR : Voltage drop	51
j : Imaginary number	19
k : CV scan rate	17
kg : kilogram.....	5
kHz : kiloHertz	28
kV : kiloVolt	26
LPE : Liquid-Phase Exfoliation	9
M : Molar.....	27
mA : milliAmpere	26
mg : milligram	25
$mg \cdot mL^{-1}$: milligram per millilitre.....	24
mL : millilitre.....	25
mm : millimetre	24
m_{total} : Total active material mass	17
$mV \cdot s^{-1}$: millivolt per second	27
mW : milliWatt	25
N : Nitrogen.....	10
n : replicates of sample	25
N_2 : molecular nitrogen.....	25
nm : nanometre	24
OHP : Outer Helmholtz Plane	4
P : Power Density.....	5
pH : Power of Hydrogen	31
PTFE : Polytetrafluoroethylene.....	7
PVDF : Polyvinylidene Difluoride.....	7
Q : Charge	5
R_{ct} : Charge transfer resistance	20
rGO : Reduced Graphene Oxide	10
$R_{leakage}$: Leakage resistance	20
rpm : revolutions per minute	24
RSD : Relative standard deviation	50
s : Probe spacing.....	16
$S \cdot cm^{-1}$: Siemens·centimetres.....	16
SCs : Supercapacitors.....	1
SDD : Silicon-Drift Detector.....	26
SEM : Scanning Electron Microscope/Microscopy	26
Si : Silicon	25
SS : Stainless steel.....	8
TGA : Thermogravimetric analysis.....	25
$UV-Vis$: Ultraviolet-Visible Light Spectroscopy.....	13
V : Volt	5
V_0 : Wave amplitude.....	18
w : Film width	16
W : Watt.....	5

w/w : weight-to-weight ratio	31
$wt. \%$: relative weight composition	31
Z' : Real impedance.....	19
Z'' : Imaginary impedance.....	19
Z_{ω} : Impedance.....	18
Z_w : Warburg impedance	20
ÅAU : Åbo Akademi University.....	24
ϵ : Molar Absorptivity of sample.....	14
η_c : Coulombic efficiency	22
η_E : Energy efficiency.....	22
π : pi.....	9
ρ : Sheet resistivity	16
ϕ : Phase angle.....	18
ω : Angular frequency	18
$\Omega\text{-cm}$: ohm-centimetres	16

1. INTRODUCTION

Today's society and recent geopolitical events have prompted the acceleration of the transition to renewable energy technologies (energy security, climate commitments, and industrial policy). One of the key considerations in this discussion is to develop green and efficient energy storage/conversion systems. Some of these existing technologies would require larger production volumes with sustainable manufacturing practices and supply chains. Therefore, demands for improvement in these aspects are needed to reduce economic losses.

Sticking with sustainability aspects, the goal of integrating current, sustainable manufacturing practices to develop energy storage devices is a high focus. Currently, 85 % of Finland's renewable energy resources are derived from biomass (IEA Bioenergy 2021) and the aim is to increase their utilisation to achieve the 2030 energy and climate targets [1]. To achieve these targets, it is pragmatic to consider minimising the use of non-renewable raw materials such as precious metals and minerals [2]. Utilisation of carbon-based materials as alternative to some of the critical raw materials can permit cheaper production costs and wider availability whilst being equally functional. This is because of their high tunability and electrochemical stability [3, 4]. Moreover, some of these materials can be derived from biomasses, thereby promoting sustainable production. Such raw materials, like graphite and cellulose, are widely abundant, easily processed, and hugely able to provide desirable functionalities such as greater surface area and mechanical durability upon application.

One of the key energy storage devices greatly utilising carbon-based materials are **supercapacitors (SCs)**. They are currently used in electric and (mild) hybrid vehicles, public transport vehicles (buses, trams, trains), consumer electronics, power tools, Internet of things (IoT) devices, and energy management systems, with the latter in its use as an intermediate power buffer in conditions of power peaks in energy demand [5, 6]. They are of particular interest because of their functional properties like high power capability, excellent cyclability, and fast response. Particularly in e-mobility applications, SCs tend as well to be smaller, lighter, and more flexible than batteries. On the other hand, batteries have significantly higher energy density and lower self-discharge. The gaps of one device are supplemented by the other, and

the challenge is in bridging their capabilities together to obtain a hybrid system that contains high energy and releases it at high rates which can last for longer periods.

All things considered, this research aims to explore the capability of graphene-cellulose nanocrystals (G-CNC) composite as an electrode material for electrochemical double-layer capacitors (EDLCs). Specifically, the research aims to (1) prepare electrodes based on the G-CNC composite, (2) evaluate the surface and electrical properties of the G-CNC; and (3) determine its overall energy storage capacity, accounting for the magnitude of energy stored and the speed of charging and discharging.

It is expected that the G-CNC composite will have a well-developed, hierarchical structure with a high active surface area, which is crucial for the EDLC performance. This study tackles the challenges of efficient material preparation and performance improvement, necessary in upscaling of “greener” production methods for EDLCs.

2. THEORY

2.1 Supercapacitors

Supercapacitors (SCs) are devices which allow electrical energy storage by means of charge separation between two conductors, separated by a dielectric material. This definition is comparable to that of a conventional, electrostatic capacitor. However, in the case of SCs, the electrode material and the dielectric are different and are made up of two, high-surface area electrodes separated by a porous dielectric to allow movement of electrolyte ions between the two sides. (Figure 1).

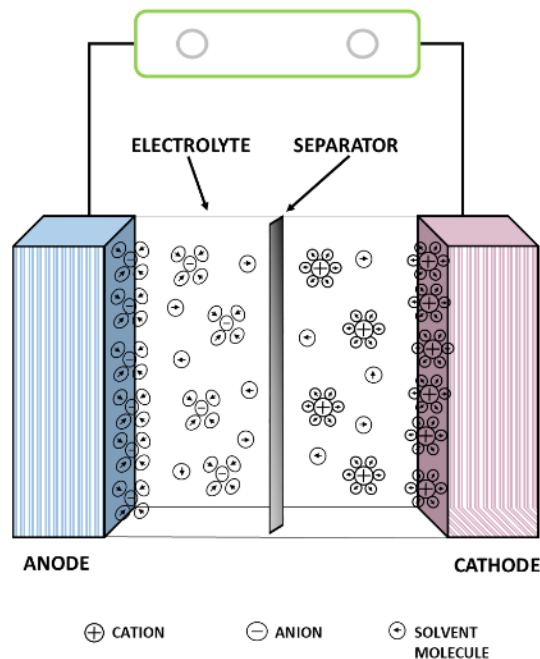


Figure 1. Schematic illustration of an electrical double-layer capacitor (EDLC), one type of supercapacitor (SC).

Classification of SCs can be subdivided into three (3) groups: (1) electrochemical double-layer capacitors (EDLCs), (2) pseudo-capacitors, and (3) hybrid supercapacitors. EDLCs are the most common SCs which rely on the conventional electrostatic charge-discharge mechanism wherein there is a reversible adsorption of the electrolyte ions on the electrode material's surface. Pseudocapacitors rely on both capacitive and fast, Faradaic, redox processes at the

electrode surface; and hybrid supercapacitors are asymmetric SCs that have a battery-like (Faradaic) electrode on one side and a capacitive electrode on the other. The contribution of Faradaic processes increases the specific capacitance in SCs but runs at an expense of device stability and cost.

The main principle of charge separation in EDLCs is based on *electrical double-layer capacitance*. The electrode-electrolyte interface is charged, with the electrolyte ions counterbalancing the excess charges present in the electrode as a function of distance from the electrode. This space forms the so-called *electrical double-layer* (Figure 2), where the electrode surface consists of adsorbed ions (in the *inner Helmholtz plane, IHP*), then there are solvated ions near the electrode surface (comprising the *outer Helmholtz plane, OHP*), and diffused ions of greater mobility. The charge separation is therefore achieved by usable work (or transferrable energy) in the form of current flow. In comparison to conventional capacitors, in SCs' a larger electrode surface area enables greater charge separation and energy storage, as it permits more sites for electrical double layer formation and lesser distance between the electrodes [5, 7, 8].

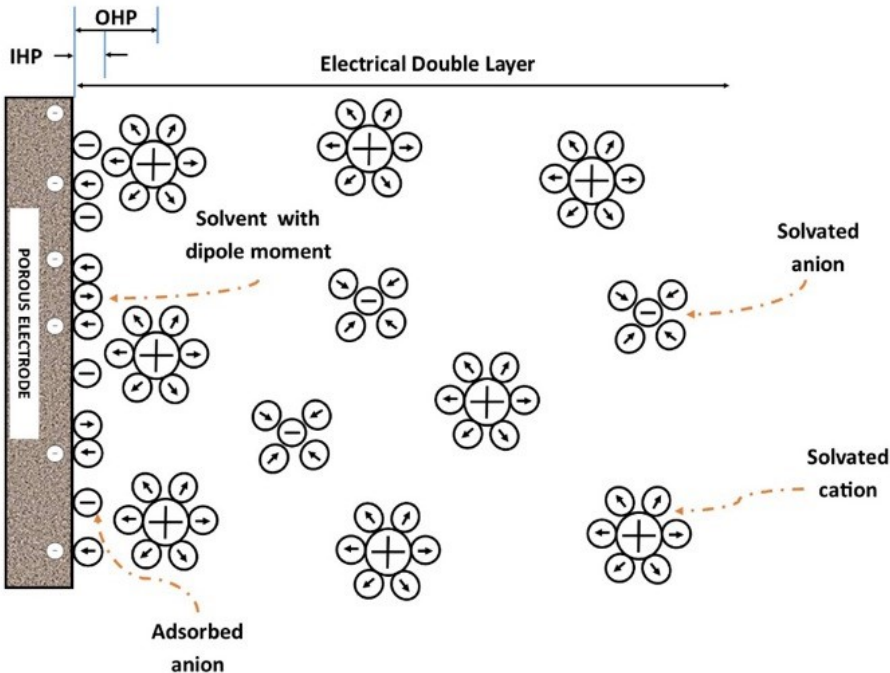


Figure 2. Model illustration of the electrical double layer formation on one side of a symmetric, EDLC electrode.

As with all capacitors, the amount of charge stored (Q , *Coulombs*) at a given cell potential (ΔV , V) is determined by the material's capacitance (C , F) (Equation 1):

$$C = \frac{Q}{\Delta V} \quad (1)$$

A greater capacitance would then translate to greater amount of energy stored, expressed by the cell's energy density (E , $W\text{-}h\text{ kg}^{-1}$) (Equation 2):

$$E = \frac{1}{2m} C(\Delta V)^2 \quad (2)$$

Wherein m is the mass of the active material.

As supercapacitors are used to provide significant amount of power to energy-dependent systems, the power density (P , $W\text{-}kg^{-1}$) is also considered:

$$P = \frac{\Delta VI}{m} = \frac{1}{4m} \cdot \frac{(\Delta V)^2}{R_{ESR}} \quad (3)$$

Wherein I is the applied current (in *Amperes*, A) and R_{ESR} is the equivalent series resistance, attributable to the cell assembly, the EDLC material components, and the set-up's electrical components. As a non-ideal capacitor, it is expected that it loses some of its energy and power during charge and discharge cycles because of the series resistance, and it typically manifests in the EDLC system as dissipated heat [9]. Moreover, EDLC systems tend to have a spontaneous loss in its capacity from its charged state (a.k.a. "self-discharge") at open circuit due to likely ohmic leakages, parasitic Faradaic reactions, or charge redistributions [10–12].

When comparing EDLCs against secondary (rechargeable) batteries, the former only relies on the physical charge separation for energy storage, which means that they do not exhibit Faradaic chemical reactions. The capacitance of EDLCs is, in principle, easier to determine because the state of charge is proportional to that of the voltage window. This generally gives EDLCs the following advantages: higher charge-discharge rates, longer cycle life, minimal thermal runaway, and cheaper average cost per cycle [13]. On the other hand, EDLCs have a lower cell potential, high self-discharge rate, poor voltage regulation, and high initial production costs per stored energy. Perhaps their most notable disadvantage is the lower energy density, best illustrated by the Ragone plot (Figure 3). Despite this setback, SCs, in general, are still useful devices for applications that would require short charging/discharging as well as the fast response for fluctuating currents.

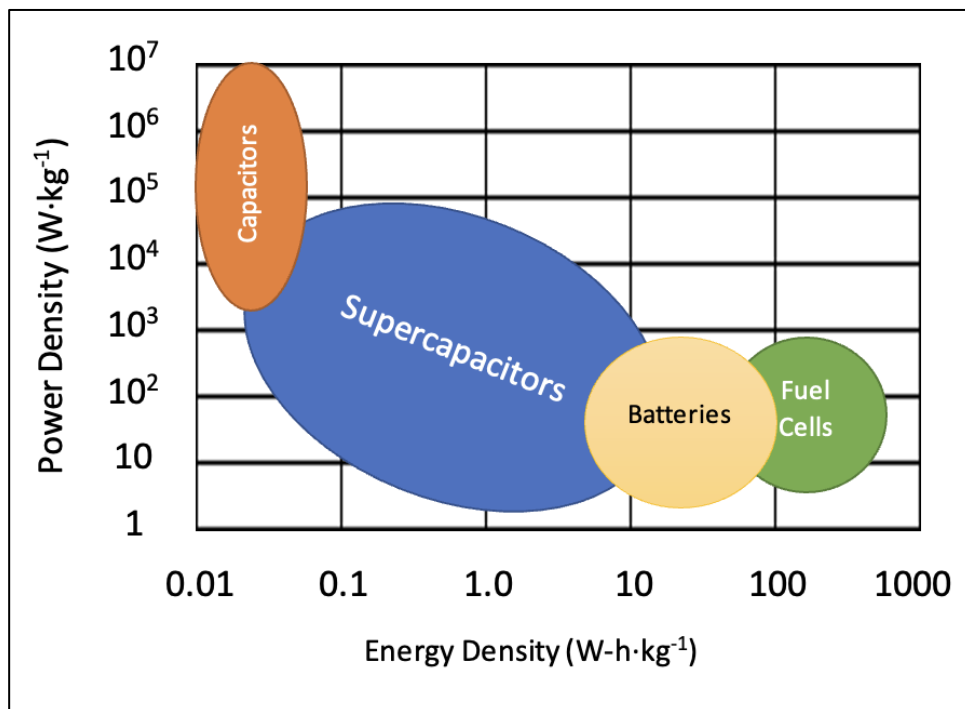


Figure 3. Ragone Plot for various energy storage and conversion devices.

The key components of supercapacitors include the following: (1) electrode material, (2) electrolyte, (3) separator, and (4) current collector. The electrode material is probably the most popular research interest in the field of SCs. That is because of the wide scope permitted for optimisation based on properties such as active surface area, material porosity, electrical and thermal conductivities, physicochemical stability, and processability. The most common

electrode materials are carbon-based due to their high surface area, low raw material cost, and cheap production [14–17]. These carbon materials can exist in various forms (e.g. activated microporous carbon, mesoporous carbon, carbon nanotubes, graphene), in which their electron configurations dictate their physical structure, chemical interactions created, and electronic properties [18, 19].

The electrolyte in EDLCs serves to provide mass transport of ions across the electrodes and provides the charge balance in the electric double layer that translates to stored energy. The electrolyte has an essential role in improving the energy and power density in EDLCs by enhancing the operating cell potential (ΔV), as shown to be exponentially dependent on cell potential (Equations 2.3). The electrolyte's interaction with the electrode material is also crucial for achieving maximal specific capacitance by choosing complementary ion that matches that of the electrode material's porosity parameters. Moreover, the stability of both the electrode material and the electrolyte must be considered, especially at higher operating potentials.

Aqueous electrolytes tend to have greater ionic conductivities and lower costs but suffer at the expense of limited operational temperature range (below water's boiling point and above its freezing point) and thermodynamic cell potential (~ 1.23 V). On the other hand, organic electrolytes are more commonly used due to their wider potential windows (up to 3.0 V) despite being more expensive and demanding to remove moisture and oxygen. Ionic liquids are also an alternative with stability (thermal, chemical, and electrochemical) as their main advantage, but the high cost and the low ionic conductivity provides a major drawback [15, 20, 21].

As electronic insulator, the separator acts as a barrier between the two EDLC electrodes to prevent their physical contact from short-circuiting the device whilst permitting electrolyte ion permeability. Thus, it should possess good wettability with the electrolyte as well as mechanical stability for easier processability and lower failure. They must also be chemically stable against possible side reactions with the electrolyte and electrochemically inert at the EDLC's operating cell potential. Different separator materials can be used, polyvinylidene difluoride (PVDF), polytetrafluoroethylene (PTFE), glass fibre, ceramics, and cellulose. PVDF and PTFE separators are used in activated carbon-based EDLCs, but cellulose is more commonly used on

large-scale due to its cheaper cost and good overall performance [15, 22]. In some cases, solid electrolytes and/or the electrode material substrate can serve as the separator material per se [23, 24].

Current collectors are one of the major EDLC components which constitutes ~15-20 % of the overall cell weight in SCs, in general. They are responsible for the current transfer from the EDLC cell's external source during charging and provides the stored energy to an EDLC-powered device upon discharge [25]. They can also act as the supporting substrate for electrode material loading, which emphasises its importance in an EDLC's capacity, rate capability, and long-term stability [26]. From a practical standpoint, current collectors should be made from a low-density, highly conductive material that is also cheap, stable, and processable [22]. Research in EDLCs typically use metal-based current collectors (e.g., aluminium, gold, or stainless steel (SS)) since they are mechanically stable and highly conductive. In the industry scale, aluminium is more commonly used as gold and stainless steel are expensive and highly dense, [22, 26]. Carbon-based current collectors can serve as an alternative due to their flexibility and lower interfacial resistance between them and the active electrode material [26]. Some examples include carbon fibre [27], graphite foil [28], carbon paper [29], conducting polymers [30, 31], carbon nanotubes [30, 32], and graphene derivatives [31–33], with the last three mentioned employing printing technologies for better immobilisation.

2.2 Graphene

As a diverse material, graphene has been one of the most promising materials to have been discovered. Having it to be pre-existent and conceived by scientists for decades, its isolation as a single, two-dimensional material only occurred when Andre Geim and Konstantin Novoselov used micromechanical cleavage or the “scotch-tape” technique on graphite flakes in 2004. During that time, they have characterised a single-atom-thick graphene layer (Figure 4) via an optical microscope. Graphene's discovery has led to further studies on 2D crystals and carbon nanostructures [16].

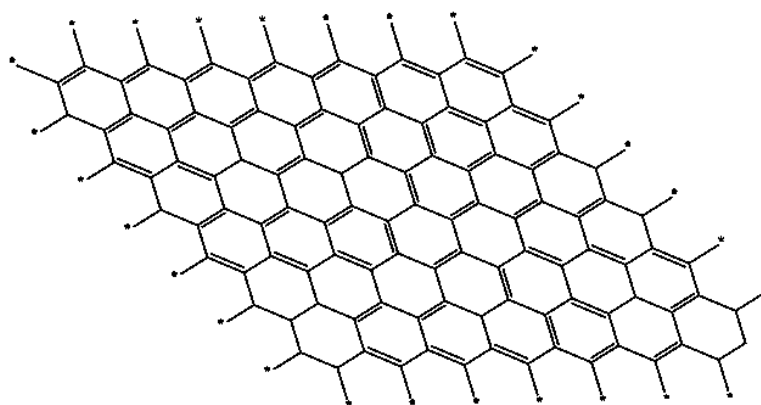


Figure 4. Molecular structure of single-layer graphene, showing its honeycomb-like lattice structure with sites for electron mobility via its pi-conjugation network.

Graphene has a hexagonal, honeycomb-like network of carbon atoms. Its lattice structure is stable as each carbon atom is sp^2 -hybridised with one free p-orbital electron, responsible for creating π -bonds or mobile electrons that can move around the network. This translates to an electronic band structure that allows semi-metallic characteristics, confirmed by tight binding theory or *ab initio* calculations. Moreover, the electronic properties of graphene are dependent on the number of layers and their stacking order, existing in single-, double-, or few-layer forms [16]. For this reason, graphene has provided a wide range of electronic and energy applications [16, 34, 35].

One of the significant challenges of utilising graphene in energy storage devices in general is its industrial up-scalability. The widespread usage of graphene-based materials would require an efficient lab-to-industry scaling and lower costs. Currently, some of the most used production methods are oxidation of graphite and subsequent exfoliation to form graphene oxide (GO) [36] and chemical vapour deposition (CVD) [37]. Both methods pose scalability challenges as the former requires usage of harmful chemical agents and extensive processing steps, while the latter involves high temperature conditions and lower overall yields [38–40]. A potential long-term alternative for these methods is liquid-phase exfoliation (LPE), wherein the graphite precursor is introduced to a stable, liquid exfoliation medium wherein physical transformation of graphite to graphene produces defect-free and fewer layers of graphene sheets for a claim of shorter processing, milder conditions, and cheaper cost [40–43].

Several LPE methods have been developed, involving different exfoliation media (e.g., aqueous and organic solvents, ionic liquids, and polymer-based/surfactant solutions) and different exfoliation techniques (e.g. sonication [41, 44], jet cavitation [45], high-shear mixing [40, 41], [46–48], wet ball milling [49–51], and microfluidisation [46]). Among these techniques, the high-shear mixing could offer a significant benefit of better preparation efficiency by obtaining higher graphene concentrations at lower energy consumption [52]. This typically involves the use of devices that can deliver controllable, high-shear forces wherein its magnitude should be sufficient to overcome the surface energies of the material for exfoliation [47, 48]. These devices include flow reactors [53, 54], rotor-stator mixers [40, 55, 56], and rotating-blade mixers [57–59]. Along with the choice of device set-up, the choice of exfoliation media and the exfoliation time are critical parameters that determine the yield of graphene sheets [47, 52].

In EDLCs, graphene has commonly been used as an electrode material due to its high electrical conductivity, surface area, and stability. It relies on the principle of the electrolyte ion adsorption on the surface of the graphene sheets, forming the electrical double layer. The cheapest, most widely developed preparation method of graphene for EDLCs is the acid oxidation of graphite, followed by chemical reduction to form reduced graphene oxide (rGO) [16, 60]. As the interlayer charge transfer through the graphene sheets translates to longer ion diffusion paths, proposed alternative methods have also been made to improve its efficiency. These include surface activation (chemical and electrochemical) [61, 62], heteroatom doping (N-, P-, or B-doping) [63–66], and self-assembly (hydrogel and aerogel) methods [64, 67].

2.3 Nanocellulose

Nanocellulose-based materials are becoming increasingly popular in the research field. Its precursor, cellulose, is one of the most abundant raw materials on Earth, with an estimate annual production of 10^{10} to 10^{11} tons [68]. Structure-wise, cellulose is composed of β (1,4)-D-glucopyranosyl (glucose) repeating units which are interlinked, forming elementary fibrils. These fibrils, when bundled, form the cellulose fibres that can be extracted from lignocellulosic sources like wood, agricultural residues, bacteria, or algae. Cellulose is a hydrophilic, water-insoluble, easily functionalised, chiral, and infusible polymer [69]. Moreover, cellulosic polymers possess different domains of varying crystallinity, depending on several factors such as degree of polymerisation, chain length, material origin, and extraction procedure. Crystalline cellulose is more resistant to functionalisation or degradation from processing treatments, whereas amorphous cellulose is more reaction-sensitive and less dense in its physical structure [70].

In its nanoscale, nanocellulose has the advantages of being more biocompatible, biodegradable, amphiphilic, chemically reactive for functionalisation, and mechanically durable, as well as having a higher surface area and being less toxic than its bulk precursor [71–73]. These benefits which can be tuned allow for extensive applications such as biomedicine, additive manufacturing, energy storage, etc. In general, nanocellulose can be classified as (1) cellulose-microstructured materials (cellulose microcrystals, cellulose microfibrils) or (2) cellulose nanofibers (cellulose nanofibrils) and (3) cellulose nanocrystals (bacterial cellulose), all of which are prepared mainly by first extracting the pure cellulose (partial/total elimination of extractives, hemicelluloses, and lignin), followed by conversion of cellulose to nanocellulose (e.g. acid hydrolysis, ball milling, chemical oxidation) [70, 74, 75].

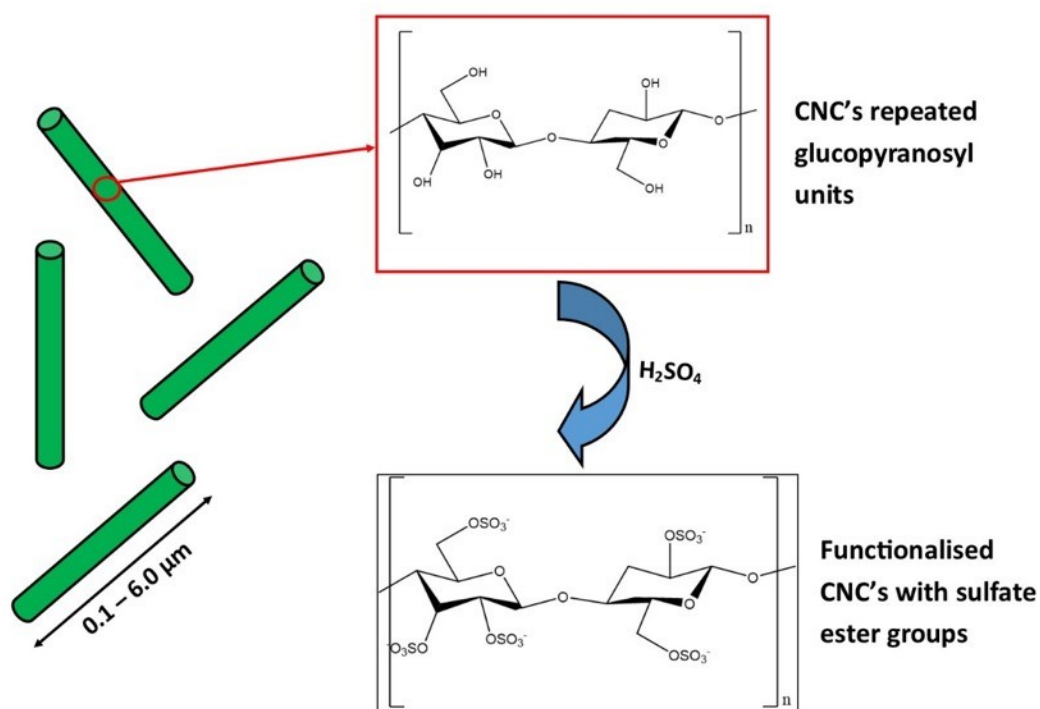


Figure 5. Sample illustration of the molecular structure of cellulose nanocrystals, along with the role of their hydroxyl groups in functionalisation showing the functionalisation of CNCs with sulphuric acid (H_2SO_4).

Cellulose nanocrystals (CNCs) are rod-like, semi-crystalline nanoparticles with a length of 100 – 6000 nm, a width of 4-70 nm, and a crystallinity index of 54-88 % (Figure 5) [76]. The most common way of producing CNCs is by acid hydrolysis with sulfuric acid, in which it eliminates the amorphous cellulose domains, and the disordered chain dislocations are prone to hydrolytic cleavage due to thermodynamic favourability of steric hindrance and kinetic factors. This in turn leaves the shorter, ordered CNC chains which are subject to post-treatment (drying, neutralisation, purification, dialysis, etc.) to recover the CNCs in their purest form. They now have the hydroxyl groups as the primary reactivity sites with a high surface area-to-volume ratio that can be chemically modified to add surface charges which distribute the nanocrystals and enhance their compatibility in composites. The effects of surface charge can also manifest in the CNC's physical properties such as viscosity of CNC aqueous suspensions wherein lower surface charge density translates into more viscous suspensions [77].

In terms of energy storage, utilising nanocellulose can address the key challenges of achieving high energy and power density in the devices, as well as rendering their processing to be more readily up-scalable thanks to its abundance, low cost, and favourable mechanical properties [72]. It has been studied for its use as electrode materials [78–81], current collectors [82], and separators [83]. As electrode material components in batteries and supercapacitors, nanocellulose provides a wider surface area and greater porosity on the thin films by creating conductive 3D networks with electroactive materials [72, 84]. In addition, its light weight makes it an attractive substrate for flexible electronic devices as it can cater large volumetric expansions to improve the cycling stability [85].

2.4 Material Characterisation Techniques

2.4.1 UV-Visible Spectroscopy

UV-Visible Spectroscopy (or simply, “*UV-Vis*”) is a widely used instrumental technique for qualitative and quantitative determination of molecular species that aids in the investigation of electronic properties of molecules and the monitoring of chemical reactions. Its principle is based on a molecule’s ability to absorb light, either in the ultraviolet and/or visible wavelength range, by which its electrons get excited from their ground state to higher energy states. The amount of light absorbed depends on the incident photon energy at a given wavelength and the energy difference between the molecule’s electronic states. [86–88]

This technique uses a spectrophotometer that measures the light intensity before and after passing through the sample. The sample is usually placed in a cuvette where a beam of light, corresponding to a specific wavelength or a range of wavelengths, passes through it. The attenuated light intensity is then detected and measured as a function of wavelength. This measurement is displayed as a spectrum consisting of peaks and troughs that is characteristic to that of the sample's composition. For quantification, UV-Visible spectroscopy is commonly employed to determine an analyte concentration by comparing the sample’s absorption spectrum to that of an analyte’s reference spectrum. The amount of analyte in the sample is proportional to the amount of light it absorbs and is described by the *Beer-Lambert’s Law* (Equation 4):

$$A = \epsilon bc \quad (44)$$

Wherein A is the absorbance of the sample, ϵ is the molar absorptivity of the analyte, b is the cell path length, and c is the analyte concentration [88].

2.4.2 Raman Spectroscopy

Raman Spectroscopy is another instrumental technique that is commonly used for elucidating molecular structures and chemical compositions. It relies on the principle of inelastic (or “Raman”) scattering of light wherein a shift in energy occurs for a fraction of the incident photons that interact with the sample. These energy shifts correspond to the different vibrational transitions in the molecules present in the sample and can shift towards a higher energy state (as “Stokes Raman shift”) or a lower energy state (as “Anti-Stokes Raman shift”) upon photon scattering [88, 89].

A Raman spectrum is collected by passing a monochromatic light source, such as a laser of given wavelength, to a sample. The intensity of scattered light is then detected and plotted as a function of the energy shift, usually expressed in wavenumbers (in cm^{-1}). The observed peaks in a Raman spectrum would correspond to different vibrational modes that are characteristic to the molecules present in the sample.

In terms of energy storage research, Raman spectroscopy is a useful tool for characterizing electrode materials and electrochemical processes in different systems such as batteries and SCs. It provides information on the structural properties of electrode materials such as their degree of crystallinity, the present phases, and the material’s defects or impurities. Moreover, electrochemical processes occurring at the electrode-electrolyte interface which can lead to phase transitions and degradation (of the electrodes and/or the electrolyte) can also be analysed. Overall, this supplemental information provides a better understanding of the energy storage system, allowing guidance to its current state of use and for improvements in the material preparation and device design [89].

2.4.3 Four-Point Probe Technique

The four-point probe is the most common technique employed for measuring the sheet resistivity or resistance of thin, semi-/conducting films as it provides fast and accurate measurements. In this technique, a set of four contact probes are equidistant to each other and arranged in a straight line (Figure 6). Current is passed through the two, outer probes, while the potential is measured across the two, inner probes. This separate I-V probe configuration permits minimal contact resistance due to potential drop at the contact points.

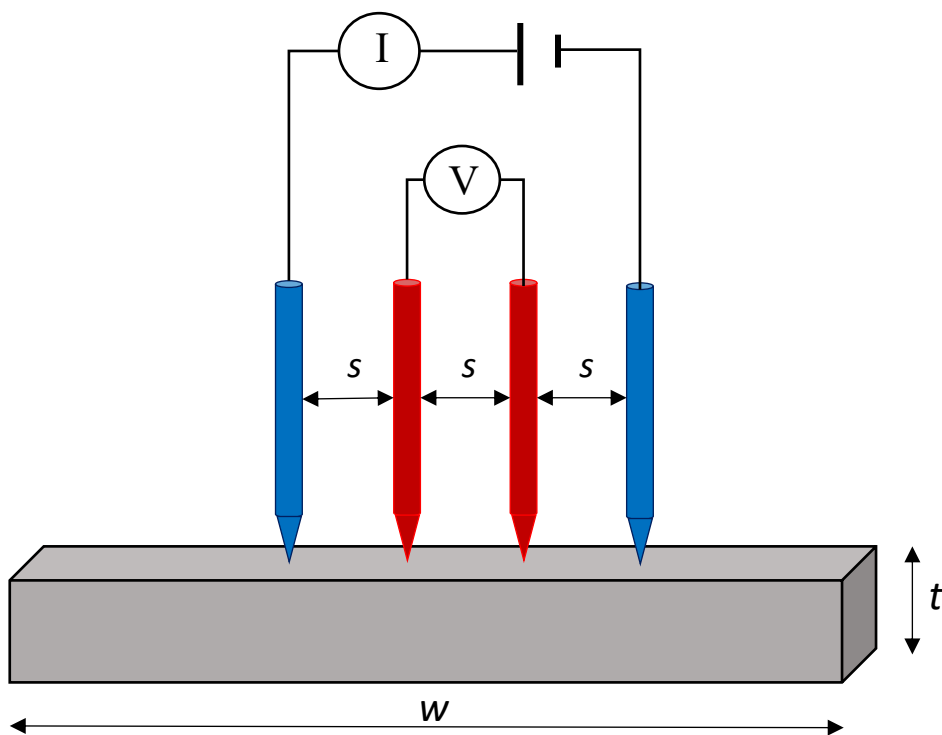


Figure 6. A simple illustration of the four-point probe electrical conductivity measurement technique. The variable current is applied on the two outer probes (blue) and the corresponding potential is measured from the two inner probes (red).

The average sheet resistivity of a thin film is based on Ohm's law (Equation 5) and is given by Equation 6:

$$V = I \cdot R \quad (55)$$

$$\rho = \frac{\pi}{\ln(2)} \cdot t \cdot \left(\frac{V}{I}\right) \quad (6)$$

Wherein ρ is the sheet resistivity ($\Omega \cdot cm$), t is the film thickness (cm), I is the applied current (A), and V is the measured voltage (V). It should be noted that Equation 6 is only valid for very thin films, meaning that their thickness is less than 40 % of the probe spacing (s in Figure 6), and the film width (w) is at least four times more than the spacing distance from the measurement point [90, 91]. Otherwise, thicker samples with a more finite width are calculated using the equation below:

$$\rho = \frac{\pi}{\ln(2)} \cdot t \cdot \left(\frac{V}{I}\right) \cdot f_1 f_2 \quad (77)$$

Wherein f_1 and f_2 are the finite thickness and width correction factors, respectively. From here, the electrical conductivity can be calculated as the reciprocal of the electrical resistivity value (expressed in $S \cdot cm^{-1}$).

2.5 Electrochemical Characterisation Techniques

2.5.1 Cyclic Voltammetry

Cyclic voltammetry (CV) is a textbook technique in electrochemistry that is based on varying the applied potential in a linear sweep over time at a fixed scan rate. The applied potential produces an output current which varies over a specified range, and repeated cycles of the voltage sweep are performed to determine the effects of electrochemical reversibility. The output current in an ideal capacitor is directly proportional to the applied voltage (Equation 8):

$$I(t) = \frac{dQ}{dt} = C \frac{dV}{dt} = Ck \quad (8)$$

The average specific capacitance of a single electrode can be calculated from the CV data based on the area under the CV curve (A_{CV}), the scan rate (k), and the total active material mass (m_{total}).

$$C_s = \frac{4A_{CV}}{\Delta V * k * m_{total}} = \frac{4I}{k * m_{total}} \quad (9)$$

Together, these relations translate to independence of scan rate with the determined capacitance that is also constant with the cell potential. But as EDLCs are mostly non-ideal, variations in the specific capacitance occur due to slow, Faradaic kinetics (for pseudocapacitors and hybrid capacitors, better expressed in terms of “capacity”) and/or transmission line behaviour due the electrodes’ porosity (Figure 5a, b) [13]. Analysing batteries with CV meanwhile provides a more apparent redox (Faradaic) response (Figure 5c).

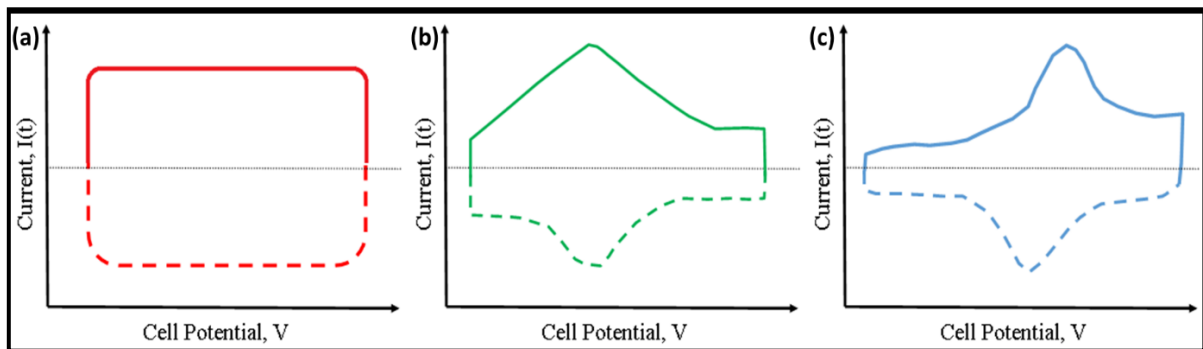


Figure 7. Schematic cyclic voltammogram profiles showing the output behaviour for various energy storage electrode materials, including (a, red) EDLCs, (b, green) pseudocapacitors, and (c, blue) batteries. The solid lines correspond to charging cycle whereas the dashed lines correspond to discharging cycle.

Profile-wise, EDLCs have an ideal rectangular response (Figure 7a), however, deviations from these curves are usually attributable to resistive elements from the experimental set-up [8, 92]. Aside from the specific capacitance, CV can also provide other essential information, such as the operational potential window and an estimate of the EDLC’s cycle life [13, 15, 93].

2.5.2 Electrochemical Impedance Spectroscopy

Electrochemical Impedance Spectroscopy (EIS) is useful for evaluating the processes occurring in one's electrochemical system under near-equilibrium conditions. These include mass transfer, diffusion, reaction kinetics, corrosion, etc. These processes can be expressed as elements of an equivalent, electrical circuit (e.g., resistor, capacitor, inductor, etc.). Moreover, combining these circuit elements is numerically expressed in terms of its *impedance* (Z_ω) against current flow that is dependent on a specific frequency (Equation 10). Thus, EIS utilises a small magnitude of sinusoidal (AC) perturbation of defined frequency, and its corresponding output response is measured for each frequency over a defined range ($\sim 10^{-4}$ to 10^6 Hz). [94, 95]

$$Z_\omega = \frac{V_\omega}{I_\omega} \quad (10)$$

The applied, sinusoidal perturbation is expressed as time-dependent, wavefunction that accounts for its amplitude (V_0) and the angular frequency (ω). Graphically, the perturbation is visualised as a rotating vector (X), wherein the vector length corresponds to the amplitude while the direction corresponds to the phase value. The same principle also applies to the output response that is out of phase with the perturbation. The difference in the input and output signal's phase value is called *phase angle* (ϕ , Figure 8). [15, 95]

$$X(t) = X_0 \sin(\omega t) \quad (11)$$

$$X(t) = X_0 \sin(\omega t + \phi) \quad (12)$$

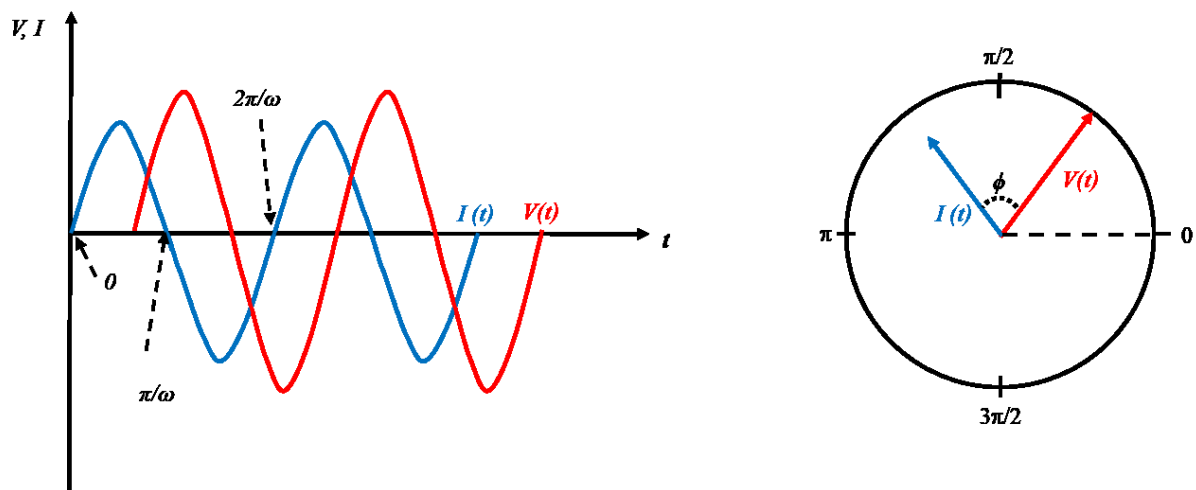


Figure 8. Phasor diagram illustrating the phase shift (ϕ) due to difference in angular frequencies and magnitude of rotating vectors for both alternating potential $V(t)$ and current $I(t)$.


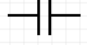

The two rotational vectors at a corresponding frequency can be expressed as a complex number, consisting of real (Z') and imaginary (Z'') parts. The phase angle can also be derived from both parts:

$$Z(\omega) = Z'(\omega) + jZ''(\omega) \quad (13)$$

$$\phi(\omega) = \tan^{-1} \frac{|Z'(\omega)|}{|Z''(\omega)|} \quad (14)$$

An electrochemical system can be modelled based on equivalent circuit elements (Table 1), but some systems may require additional, more complex elements. In most cases, the resistor and capacitor elements are modelled in series and/or parallel with each other, especially in the low-frequency region in which capacitive processes dominate. With EDLCs, the typical model used is a simplified Randles circuit (Figure 9). [7, 95]

Table 1. Basic electrical circuit elements conventionally used in EIS.

Element	$ Z $	Z'	Z''	ϕ
Resistor 	R	R	0	0
Capacitor 	$\frac{1}{\omega C}$	0	$\frac{1}{j\omega C}$	-90°
Inductor 	ωL	0	ωL	90°

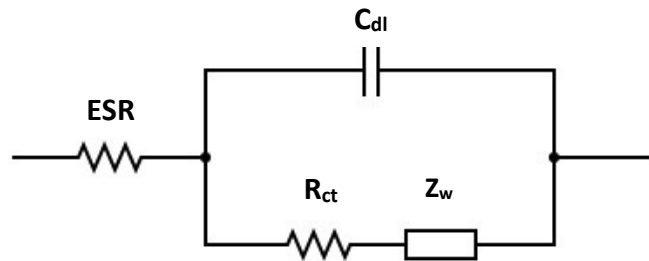


Figure 9. Randles equivalent circuit model for illustrating the processes present in an electrochemical system.

The Randles model circuit elements include the equivalent series resistance (*ESR*), leakage resistance (R_{leakage}), and ideal double-layer capacitance (C_{ideal}). The leakage resistance can be further specified, accounting for charge-transfer resistance (R_{ct}) and Warburg impedance (Z_{w}) for diffusion-related processes [8, 94, 95]. These elements are best illustrated using a Nyquist plot (Figure 10):

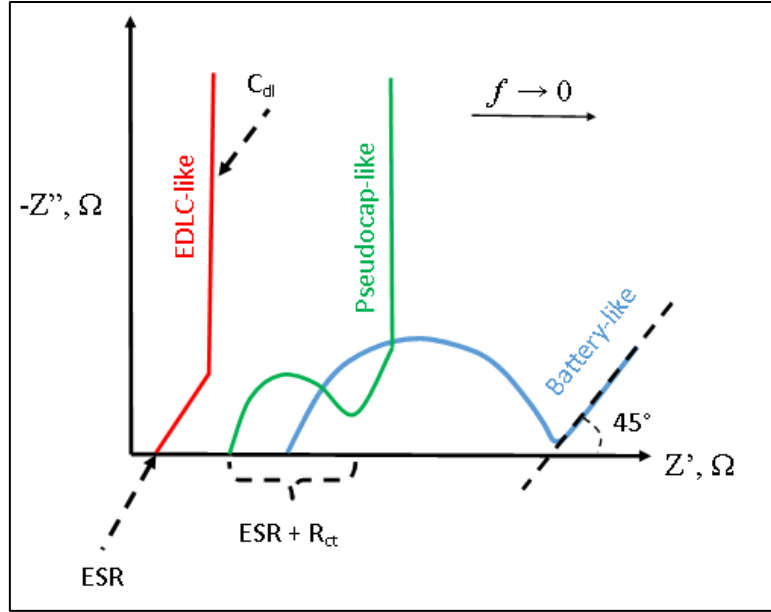


Figure 10. Nyquist plot representation for various energy storage materials, showing different Randles circuit elements modelled present for each device (red – EDLC, green – pseudocapacitor, blue – battery). Note that effect of charge transfer resistance is also present in batteries. The Warburg impedance can be extrapolated from the 45° region of the green and blue plots.

2.5.3 Galvanostatic Charge-Discharge

Galvanostatic Charge-Discharge (GCD), also known as the constant current method, is a technique that is commonly employed and generally accepted in both academia and industry for analysing battery and supercapacitor performance as it accurately depicts how the applied load is typically used in commercial applications [96, 97]. This involves application of constant current input to one's cell (two- or three-electrode system) during charging and discharging. This in turn provides a voltage output as a function of time, performed for several cycles to also determine the rate capability of the system. For calculating the (averaged) specific capacitance of a single electrode, the slope of the discharge curve (expressed now as *discharge capacitance*) is taken and is governed by the equation below:

$$C_s = \frac{4I}{m_{total}} \times \frac{\Delta t}{\Delta V} \quad (15)$$

Where I is the applied, constant current, m_{total} is the total active material mass of the two electrodes, and $\frac{\Delta t}{\Delta V}$ is the discharge curve slope. It is important to note that the GCD profile indicates the charging and discharging efficiency. This means that it also tells us the magnitude of the factors affecting the efficiency, such as equivalent series resistance and faradaic contributions, if present (Figure 9).

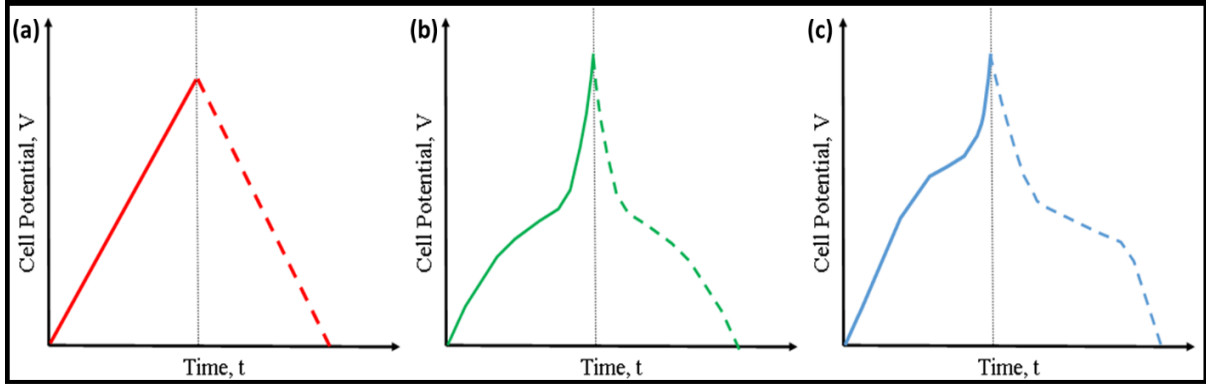


Figure 11. Schematic galvanostatic charge-discharge profiles showing the output behaviour for various energy storage electrode materials, including (a, red) EDLCs, (b, green) pseudocapacitors, and (c, blue) batteries. The solid lines correspond to charging cycle whereas the dashed lines correspond to discharging cycle.

The device efficiency is usually expressed in terms of Coulombic efficiency (η_c , Equation 16):

$$\eta_c = \frac{t_{discharge \text{ at cycle } n}}{t_{charge \text{ at cycle } n}} \quad (16)$$

Where both the time t for charge and discharge are of the same cycle n . This in turn assumes an ideal, linear response for charging and discharging, which is often not the case and leads to overestimation of the device performance. Therefore, a better parameter to use is energy efficiency (η_E , Equation 17):

$$\eta_E = \frac{E_{discharge \text{ at cycle } n}}{E_{charge \text{ at cycle } n}} = \frac{\int_{t(V_{\max})}^{t(V_{\min})} V(t) dt}{\int_{t(V_{\min})}^{t(V_{\max})} V(t) dt} \quad (17)$$

Wherein it is expressed as a ratio of discharging ($E_{discharge\ at\ cycle\ n}$) and charging ($E_{charge\ at\ cycle\ n}$) energies which is obtained by integrating the area under the charge and discharge curves. This would consider the non-idealities of the EDLC [8, 98].

3. METHODOLOGY

The work is divided into four parts: (1) Preparation of graphene-CNC (G-CNC) dispersion, (2) Preparation of G-CNC electrodes, (3) Physico-chemical characterisation, and (4) Electrochemical characterisation of electrode materials.

3.1 Preparation of G-CNC Dispersion

The procedure used in this work is in accordance with the preparation of Lund, et al. [55]. Natural flake graphite (Alfa Aesar, ~325 mesh, 99.8 %) was exfoliated directly in a suspension of cellulose nanocrystals to form a composite of graphene and CNC. Graphite flakes were “added” to the suspension of cellulose nanocrystals (produced at ÅAU, Laboratory of Natural Materials Technology) in various graphite-to-CNC weight ratios, with a graphite concentration of 100.0 mg/mL of the dispersion. The mixture underwent high-shear exfoliation using POLYTRON® immersion disperser with a PT 10-35 GT drive unit coupled with a PT-DA 20-dispersing aggregate with a rotor diameter of 15.0 mm and a rotor-stator gap of 0.30 mm. The exfoliation was set at 22000 rpm for 3 h in a water bath cooler (*Hetofrig, Denmark*) with a water bath circulator (*MGW Lauda MT*) that maintained a constant temperature of 18.0°C ($\pm 0.5^\circ\text{C}$).

The exfoliated dispersion was then allowed to stand overnight prior to removal of unexfoliated, graphite residue via two-cycle centrifugation (*Hermle Labortechnik Z36HK*) at a rotor speed of $270 \times g$ for 0.5 h. Graphene concentration was determined by UV-Visible spectroscopy (*Shimadzu UV-2501 PC*) at the absorption wavelength maximum of 660 nm. The molar absorptivity value (ϵ) used for the analysis was $65.90 \text{ mL}\cdot\text{mg}^{-1}\cdot\text{cm}^{-1}$, as previously determined [55, 99, 100].

3.2 Preparation of G-CNC Electrodes

The G-CNC dispersions were applied onto graphite foils (SGL Carbon Foil® SIGRAFLEX F, 200 mm x 270 mm x 0.25 mm) via spray-coating. The graphite foils were washed with N-Methyl pyrrolidone and acetone, then plasma-cleaned (*Harrick PDC-002 Expanded Plasma Cleaner*) prior to the spray-coating. The foils were then placed on a heating plate,

regulated at 100 °C. A standard airbrush pen was used, with an applied coating volume per unit area of 2.00 mL/6.25 cm² during the heating. Spray-coated foils were then punched into electrodes with an area of 0.75 cm² and 2.0 cm² for electrochemical measurements (Section 3.4). To determine the active material mass, the electrodes were weighed after punching. Average weight was taken on uncoated, punched electrodes ($n = 10$) to determine the substrate mass of similar areas.

3.3 Physico-chemical Characterisation

3.3.1 Raman Spectroscopy

To confirm the formation of the dispersed graphene sheets, different batches of the G-CNC dispersion were measured via Raman spectroscopy. About 10 µL of each dispersion was drop-casted onto a glass slide. These slides were oven-dried at 60 °C for 15 minutes and cooled afterwards for the sample analysis. Raman spectra were recorded using an Ar-ion laser with an excitation wavelength of 514 nm and a laser power of 25 mW in the 3500 to 500 cm⁻¹ wavenumber range (*Renishaw Ramascope imaging microscope with WireTM v1.3 Raman software*). The spectrometer was calibrated with a 520 cm⁻¹ Si standard as reference sample. Three (3) spectra were recorded of each dispersion. For comparison, Raman spectra were also taken of the graphite flakes applied on stainless steel substrate, without any pre- treatment.

3.3.2 Thermogravimetric Analysis

The relative amounts of the graphene and the CNC in the dispersions were determined through thermogravimetric analysis (TGA). The G-CNC dispersions were oven-dried at 60 °C overnight for the sample preparation. TGA was performed under an oxygen-free environment at a heating rate of 10 K·min⁻¹ up to 900 °C, with N₂ flow of 60 mL·min⁻¹ (*SDT Q600 apparatus from TA Instruments (New Castle, DE, USA)*). Two replicates of 10 mg sample amounts were used for each G-CNC batch analysed.

3.3.3 Scanning Electron Microscopy and Elemental Analysis

The surface morphologies of the G-CNC composite electrodes were evaluated with a scanning electron microscope (SEM). For the graphite foil substrate, the top surface was characterized using a LEO Gemini 1520 instrument (*Zeiss*), equipped with an Ultra Dry Silicon Drift Detector (*SDD, Thermo Scientific*) at Åbo Akademi. This SEM instrument model is integrated with an energy-dispersive X-ray (EDX) Spectrometer.

Additional sample preparation for the G-CNC electrodes were done using focused ion beam milling (*Hitachi ArBlade IM5000 CTC*) at an accelerating voltage of 5.5 kV and an extraction voltage of 1.5 kV. Representative samples were cut with a razor blade and the top surface was attached to a glass cover slip with carbon cement (*Leit-C, Plano GmbH*). The cover slip was attached to the cross-section holder with the same cement, with the ion beam cut starting from the backside of the sample. This backside was covered with a tungsten carbide mask.

The G-CNC electrodes' surface and cross-sectional morphologies were evaluated using an Apreo S field-emission scanning electron microscope (*Thermo Scientific*), equipped with an Everhart-Thornley detector (ETD) for sample topography and three in-lens detectors (T1-T3) for elemental contrast. EDX data was taken using an integrated UltimMax 100 Energy-dispersive X-ray spectrometer (*Oxford Instruments*). SEM-EDX characterisation of the G-CNC electrodes were conducted at the Industrial Physics Laboratory of University of Turku.

3.3.4 Electrical Conductivity

The four-point probe method was then used to determine the electrical conductivity of the G-CNC films on the thin glass substrates. Different batches of the G-CNC dispersion were spray-coated onto thin glass substrates of various coating volumes (0.10, 0.25, and 0.50 mL) per coating area of 6.25 cm². The set-up consists of probes that have a linear configuration with 1.82 mm tip spacing. Various bias currents (10.000 μ A – 2.0000 mA) were applied using a Keithley 2400 SourceMeter where

the output voltage was stable and reproducible. The film conductivities were calculated using correction factors for finite size when the thickness of the films was known [94]. The film thickness was estimated with atomic force microscopy (AFM).

Samples for AFM measurements were obtained from the four-point probe samples. The films were carefully scratched with a surgical knife for acquiring their corresponding line profiles. AFM images were taken with an NTEGRA PRIMA (NT-MDT, Moscow, Russia) instrument at tapping mode under ambient conditions, using silicon cantilevers with a nominal curvature tip radius of 8 nm (*Model: HQ:NSC18 / AI BS*) at a scan rate of 0.98 – 1.30 Hz. Image dimensions were 100 μm * 100 μm (256 * 256 pixels), and the film thickness was calculated as an average of the height data from the line profile images at ten (10) different lines of the scanned image.

3.4 Electrochemical Characterisation

3.4.1 Three-electrode system

Three-electrode measurements were carried out with a potentiostat/galvanostat (Gamry Instruments Reference 620) with the coated G-CNC electrodes (1.5 cm x 0.5 cm) as the working electrode. An Ag/AgCl single-junction electrode (*Redoxme AB, Sweden*) and a carbon rod wrapped with carbon cloth were used as the reference and counter electrodes, respectively (Figure 12, left). Cyclic voltammetry (CV) experiments were conducted in aqueous 1.0 M NaClO₄ electrolyte solution within a potential range of -0.6 V to +1.0 V for twenty (20) cycles at 50 mV·s⁻¹ scan rate.

3.4.2 Two-electrode system

Two-electrode measurements were carried out with a potentiostat/galvanostat (Gamry Instruments Reference 620) analyser using a two-electrode test cell system (HS Test Cell, Hohsen Corporation and Åbo Akademi University). The test cell contains two 2.0 cm² G-CNC electrodes filled with ~3.5 mL 1.0 M NaClO₄ electrolyte solution, with a 0.5 mm thick cellulose-based filter paper (Sartorius) as a separator between the G-CNC working electrodes.

Cyclic voltammetry (CV), electrochemical impedance spectroscopy (EIS), and galvanostatic charge-discharge (GCD) experiments were performed with the two-electrode set-up (Figure 12, right). CV scans were performed for twenty (20) cycles at different scan rates (2, 10, 50, and 250 $\text{mV}\cdot\text{s}^{-1}$). EIS measurements were recorded at a frequency range of 10 mHz to 500 kHz with an applied AC potential of 10 mV and a DC potential fixed at 0.0 V. GCD experiments were conducted at different constant current densities (0.1, 0.5, and 1.0 $\text{A}\cdot\text{g}^{-1}$) in the same potential windows as in the CV.

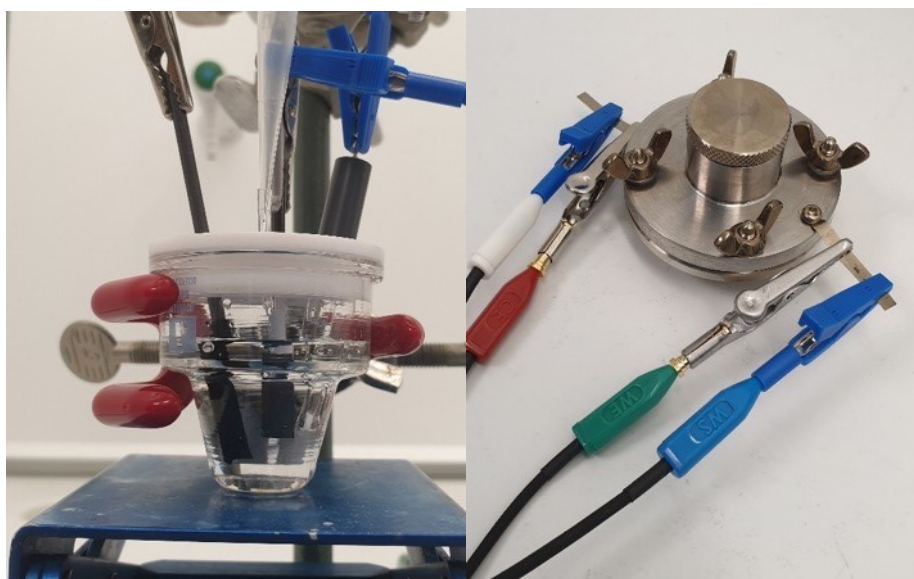


Figure 12. Experimental assemblies used for (a) three-electrode and (b) two-electrode electrochemical characterisations.

4. RESULTS AND DISCUSSION

4.1 Preparation of Graphene-CNC Composite

The high-shear exfoliation of graphite flakes with cellulose nanocrystals (CNC) as a stabilising agent can provide an up-scalable and greener approach for preparing few-layer graphene sheets [52, 53, 55]. The CNCs contain the hydrophobic -CH backbone which attracts the hydrophobic graphene, while its negatively charged sulphate ester (-OSO₃⁻) groups provides the surface charges needed for their electrostatic repulsion, allowing them to disperse the graphene sheets in aqueous media. For this research, it was imperative to maximise the amount of graphene present in the dispersion.

Table 2. Calculated graphene concentrations obtained after high-shear exfoliation of graphite in CNC aqueous suspension.

G-CNC Batch	Initial CNC Conc. (mg·mL ⁻¹)	Initial Graphite:CNC Ratio (w/w)	Graphene Conc. (mg·mL ⁻¹)
1, 4	6.71	50:1	0.054
3	6.71	40:1	0.056
6	1.9	52.6:1	0.070
7	11.6	50:1	0.011
8 - 9	11.6	8.6:1 (undiluted)	10.8
10	11.6	25:1	0.71
11	11.6	15:1	11.2
12	11.6	8.6:1 (undiluted)	14.4
15	11.6	20:1	1.1
*16	11.6	15:1	13.3
*19	11.6	15:1	6.1
20 - 21	11.6	15:1	0.071
22 - 30	12.5	15:1	0.83
31	12.5	15:1 (pH adjusted to 7.0)	10.9
32	12.5	8:1 (undiluted)	14.0

*Combination of multiple dispersion batches ($n = 2$; Batches 13+14 = 16 and 17+18 = 19); G-CNC Batches 2 and 5 were discontinued due to low graphene concentrations upon visual examination; G-CNC batches with similar initial precursor ratios are averaged for reporting purposes. These batches were not combined to make a high-volume dispersion. Text in orange correspond to the batches that have been used for further characterisations due to higher dispersion volumes collected.

Graphene-CNC dispersions were prepared using different graphite-to-CNC ratios (Table 2) to determine the optimal composition for the EDLC application. These ratios aim to maximise the dispersion of the graphene sheets with an optimal amount of CNC [59]. The graphene concentrations are estimated by UV-Vis Spectroscopy. The UV-Vis spectra of the G-CNC dispersions shown in Figure 13 were studied at two regions – the absorbance at $\lambda = 660$ nm for maximal absorbance at minimal interference and the absorption band at $\lambda_{\text{max}} = \sim 260$ nm corresponding to the π -plasmon resonance peak caused by the delocalisation of graphene's π – electrons [101, 102].

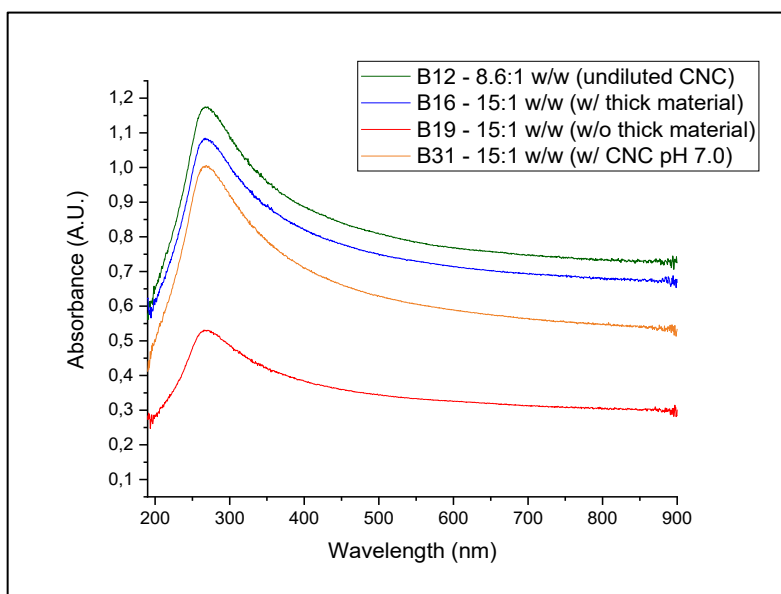


Figure 13. UV-Visible spectra for selected batches of the G-CNC dispersion, corresponding to different preparations and obtained graphene concentrations.

The graphene concentration changes with the mass ratio of the precursor materials, with the mass ratio of 15:1 w/w Graphite:CNC being most suitable by attaining concentrations above $4.0 \text{ mg} \cdot \text{mL}^{-1}$. Preparation using the previously optimised 50:1 graphite-to-CNC mass ratio by Lund et al. [56] produced low concentrations with unstable dispersions, in our case (Table 2). It is suspected that there are potential variations in the CNC stock suspension, specifically with the microcrystalline cellulose source. In initial G-CNC batches (1-6) CNC suspensions which were deemed unstable due to presence of aggregates in the suspension were used. In succeeding batches freshly prepared (<6 months from usage) CNC suspensions were used.

Even with the newer CNC suspension, a low graphene concentration was still obtained with the 50:1 initial mass ratio. It was also suspected that the relatively acidic pH (pH 3.0 – 4.0) of the stock CNC suspension had an impact on the surface charges needed to disperse the graphene sheets. Previous literature suggests that the CNC suspensions are maintained at pH above 6 [56]. For comparison, a different G-CNC batch was prepared where the pH of the CNC suspension was adjusted to neutral pH (Batch 31). This has originated from a different stock CNC suspension ($12.5 \text{ mg}\cdot\text{mL}^{-1}$) due to insufficient amount of CNC suspension left from the previous suspension used ($11.6 \text{ mg}\cdot\text{mL}^{-1}$). Moreover, all G-CNC batches yielded dispersion volumes of just about 50 % of the initial preparation volume before exfoliation. This is partly due to water evaporation during the mixing as well as a significant amount of trapped water in the unexfoliated graphene sheets.

What is also worth noting is that there are large differences in the graphene concentrations having a similar graphite-to-CNC mass ratio of 15:1. This is attributable to variations in the preparation step, such as the collection of the G-CNC dispersion during the centrifugation step as well as defects in the rotor during the high-shear exfoliation. It is also possible that some partially exfoliated graphite was collected in the dispersions. These differences were visually apparent during the electrode preparation (Section 3.2), as well as the yielded dispersion volumes. This was the case with the G-CNC Batch 16 having a thicker dispersion consistency than with G-CNC Batch 19.

Despite these instances, it was shown that the G-CNC dispersion using undiluted CNC suspension (1.16 wt. %, 8.6:1 w/w) had exfoliated the highest amount of graphene as there is more CNC available for stabilisation of the graphene sheets. Using undiluted CNC suspensions is expected to decrease the electrical conductivity of the dispersion due to the CNC's insulating nature. In addition to practical considerations of CNC consumption, it was still preferable to proceed with the G-CNC batches prepared using dilute CNC concentrations.

4.2 Physico-chemical Characterisation

As potential EDLC electrode materials, the G-CNC composite must exhibit sufficient surface area, porosity, and electrical conductivity. This is to increase the active sites for the electrical double layer formation within a material of low resistance. Thus, it is necessary to investigate the material's intrinsic properties as well as the EDLC electrode's microstructure and surface morphology.

4.2.1 Evaluation of Quality of Exfoliated Graphene Sheets

Characterisation of the G-CNC composite through Raman spectroscopy provides detailed information regarding the structure of the composite and the effectiveness of the exfoliation of the graphene sheets. Figure 14 illustrates the differences in the characteristic Raman bands of the graphitic structures for various G-CNC batches used. The most important features of the Raman spectrum for graphite are the G band ($\sim 1580\text{ cm}^{-1}$) and the 2D (or G') band ($\sim 2720\text{ cm}^{-1}$). The G band is characteristic to the in-plane vibrations of the sp^2 -hybridised carbon atoms in the individual graphene layers, while the 2D band is an overtone of the D band ($\sim 1350\text{ cm}^{-1}$) that corresponds to graphene's honeycomb ring breathing modes and are activated by structural defects (e.g., vacancies, sp^3 -hybridised carbon, flake edges). This D band is more intense as the flake size of the graphene layers decreases. [103–106]

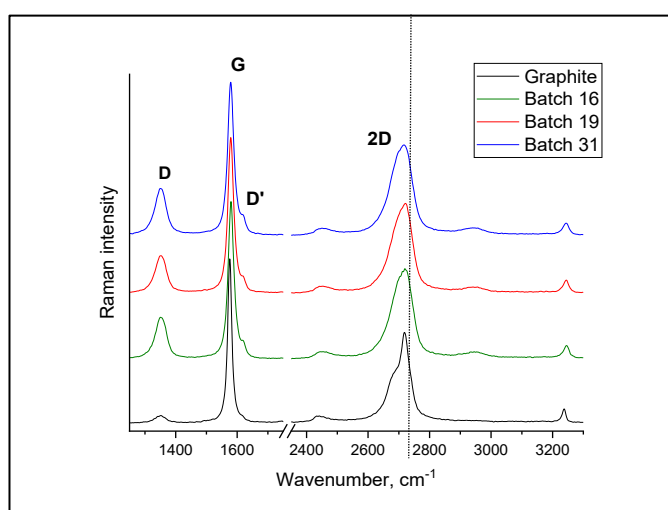


Figure 14. Representative Raman spectra for different batches of the G-CNC dispersions compared with the spectrum of the graphite flake ($<45\ \mu\text{m}$) precursor. Results are normalised to the 2D band intensity.

The G band's position heavily depends on the number of graphene layers and to some extent, on their crystallinity. In the prepared G-CNC's, the Raman shift of the G band position from graphite towards higher wavenumbers indicates the decrease in the number of graphene layers and a less amorphous microstructure [103, 105]. The observed shift was rather small (+ 4 cm⁻¹) for the three G-CNC batches tested.

A more reliable indication of the presence of few-layer graphene in the G-CNC is the downshift and the smoothening of the shouldered, 2D band of bulk graphite [56]. A narrow, symmetrical 2D band (~2700 cm⁻¹) is characteristic to single-layer graphene. While all the G-CNC dispersions had more symmetrical 2D bands, the downshift was more evident only for the G-CNC Batch 31. The downshifting was quantified by estimating the convoluted peak area ratios within the 2D signal (2D₂/2D₁) shown in Table 3, wherein the ratio was notably lower for G-CNC batch 31 than for the other G-CNC batches. This signifies that there is more of the few-layer graphene present in Batch 31 than the other batches. In addition, intensity ratios of the G and 2D band show the increase in intensity of the 2D band, characteristic to exfoliated graphene [107, 108]. Determining the exact number of layers is out of scope of this study but previous studies have demonstrated that the 2D band of graphite and of few-layer graphene with five to ten layers or more are almost indistinguishable and difficult to interpret [107, 109].

Table 3. Comparison of intensity and area ratios of different Raman bands for different batches of the G-CNC composite.

G-CNC Batch	Graphene Conc. (mg·mL ⁻¹)	2D ₂ /2D ₁ Area Ratio*	G/2D ₂ Intensity Ratio	D/G Intensity Ratio
Graphite	-	1.5	2.0	0.1
16	13.3	0.8	1.7	0.3
19	6.1	0.8	1.7	0.3
31	10.9	0.6	1.8	0.3

*2D₂ – band at ~2720 cm⁻¹; 2D₁ – band at ~2680 cm⁻¹
The ratios are mean values from three different spectra.

The D/G intensity ratio is also another useful indicator of the graphene exfoliation quality. Relative from graphite's ratio ($I_D/I_G \sim 0.07$), those of that for the three G-CNC batches ($I_D/I_G \sim 0.3$) are significantly higher because of the number of the edge defects introduced by the liquid-phase exfoliation with the decrease in flake size [55–57]. The absence of additional defect types can be confirmed by the D/D' intensity ratio wherein the three G-CNC samples have approximately similar values (2.0 – 2.1 vs. 1.1 for graphite). Higher ratios were obtained for defects such as sp^3 -type and on-site vacancies by previous studies [56], suggesting that the high-shear exfoliation have introduced mainly boundary-like defects in the graphene sheets.

4.2.2 Estimation of Relative Amount of Graphene and CNC

Thermogravimetric analysis of various G-CNC batches was conducted to get a rough estimate of the relative amounts of graphene and CNC in the obtained dispersions. As it was observed that there were variations in the graphene concentrations at similar precursor mass ratios, TGA would be able to roughly quantify these variations. The used graphite flakes and stock CNC suspensions were used as reference for the thermal profiles of G-CNC (Figure 15).

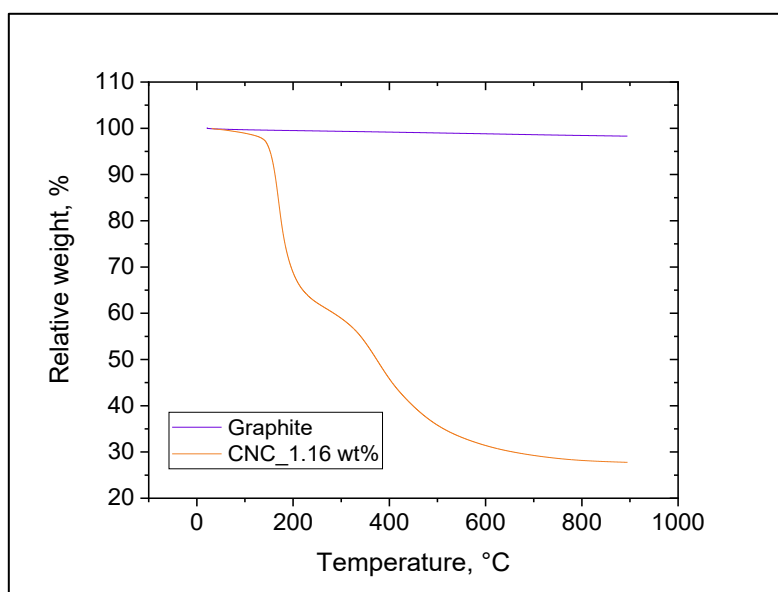


Figure 15. TGA thermograms taken from the graphite (in purple) and pure CNC (in orange) reference samples.

As an initial note, it is consistent in all the TGA profiles that the weight loss of foreign volatile components and moisture was observed at around 100 °C. The graphite precursor had minimal decomposition (1.7 %) with an almost linear weight loss profile. On the other hand, the pure CNC had a more pronounced profile, with two regions of major weight loss – (1) a ~30 % loss from 130 °C to 250 °C and (2) a ~35 % loss from 300 °C to 500 °C corresponding to the CNC’s low-molecular weight and amorphous components [110, 111]. These weight losses were apparent in the three G-CNC batches tested (Batches 16, 19 and 31) along with a batch using the undiluted CNC suspension (Batch 12). Their respective profiles are presented in Figure 16.

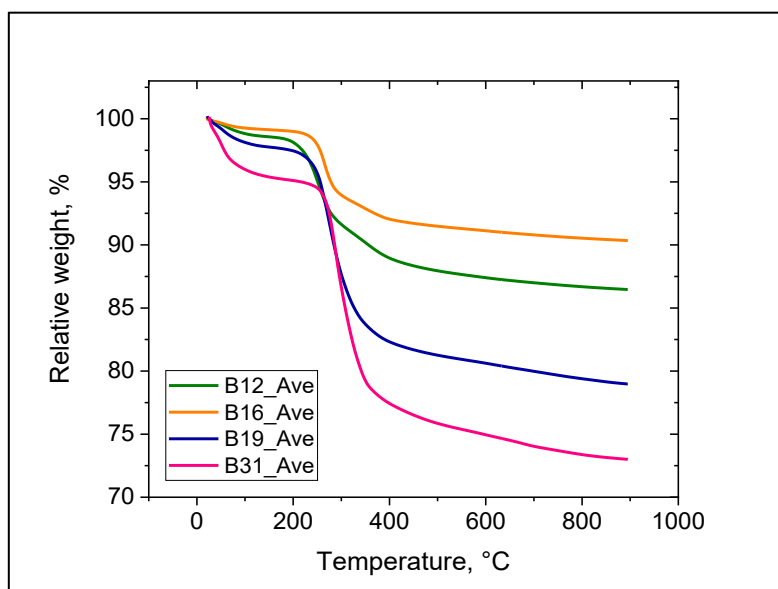


Figure 16. TGA thermograms for various batches of dried G-CNC dispersions. All batches (except Batch 12 in green) have similar starting mass ratios of graphite and CNC (15:1). The thermograms are taken as the average of two replicate measurements.

The proportionality of the CNC amounts in the G-CNC can be deduced from the magnitude of the weight losses. Figure 16 shows that G-CNC Batch 31 had the largest (relative) amount of CNC by having the largest total weight loss of ~26 %. This would correspond to a 68 % graphene composition in the dispersion. The determined relative compositions for each G-CNC batch are presented in Table 4. It is worth noting that the %wt. of graphene obtained for the G-CNC batches 19 and 31 are roughly comparable to those obtained by Lund, et al. at 60-70 % using more diluted CNC suspensions [56].

Table 4. Calculated average, relative amounts of graphene and CNC in their respective dispersion batches obtained from TGA analysis.

G-CNC Batch	%Weight loss (total)	% CNC (w/w)	%Graphene (w/w)	G:CNC Ratio (w/w)
12 (undiluted)	13.4	15.4	84.6	5.5:1
16	9.6	10.6	89.4	8.5:1
19	20.8	24.8	75.2	3.0:1
31	26.3	31.9	68.1	2.1:1

It was assumed beforehand that the undiluted G-CNC dispersion would have the highest amount of CNC recovered, but this was not the observed case. Moreover, the obtained relative amounts of graphene do not clearly coincide with the determined concentrations measured by UV-Visible spectroscopy. It is possible that the previously mentioned variations in the preparation conditions have impacted the exfoliation efficiency of the graphene sheets. It is also suspected that the relatively higher amount of CNC in the starting composition of the CNC and graphite mixture the Batch 12 dispersion because of the use of undiluted CNC suspension would have functioned as a binder and has bound the unexfoliated graphite during the high-shear mixing and was lost during the centrifugation step. Overall, the estimates of the graphene and CNC relative amounts have coincided well with the obtained surface morphologies on the electrodes (Next section).

4.2.3 Surface Morphology and Elemental Composition

Top-view SEM images of the different batches of the G-CNC composite permits visualisation of the EDLC electrode surface (Figure 17). The graphite foil substrate has a rather flat, non-porous surface (Figure 17a) due to graphite's compact structure. However, the surface morphologies of the electrodes with the G-CNC layer on top of the graphite foil were different, corresponding to the varying graphene concentrations measured by TGA. G-CNC Batch 16 which had a significantly higher graphene concentration according to UV-vis and TGA analysis have a grain-like, porous morphology with 3D aggregates on the surface (Figure 17b). This is suspected to be partially exfoliated graphite flakes that are densely bound by the CNCs, forming irregular, spherical microstructures. It should be noted that the porosity of these electrode batches does not necessarily translate to the efficiency of the double layer formation, as these illustrations are on the micro-scale of its elucidation. The degree of partial exfoliation is consistent with the TGA rough estimates and the Raman profiles, as the electrode prepared with G-CNC Batch 31 had a smoother surface and less aggregated material (Figure 17d). These differences were also evident upon visual examination of the electrodes, as the less concentrated G-CNC dispersions had a smoother surface and a pronounced luster on the graphite foil substrate (See Appendix B).

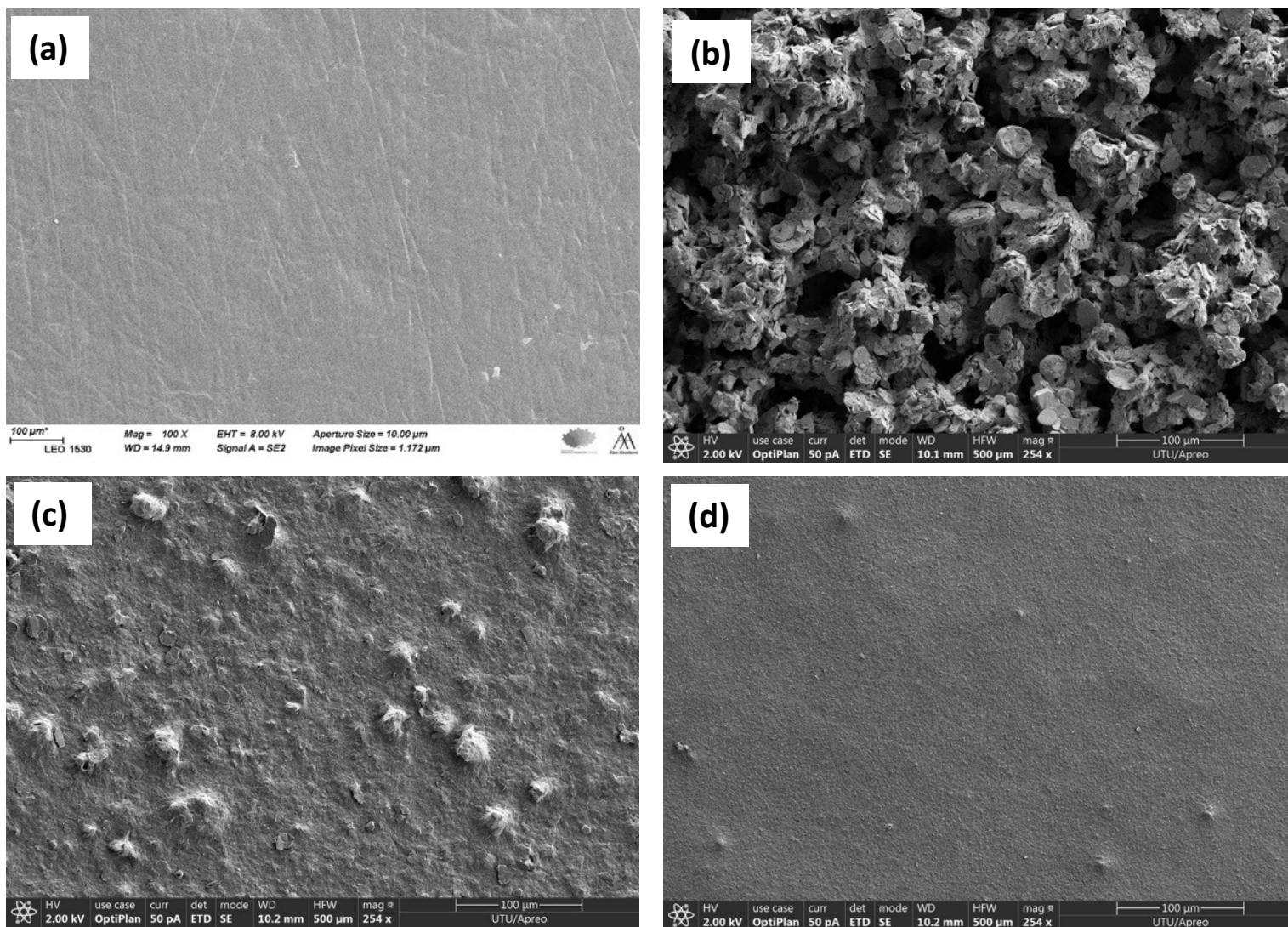


Figure 17. Low-magnification SEM images (top-view, 254 \times) corresponding to the surfaces of (a) the graphite foil substrate, (b) G-CNC Batch 16, (c) Batch 19, and (d) Batch 31.

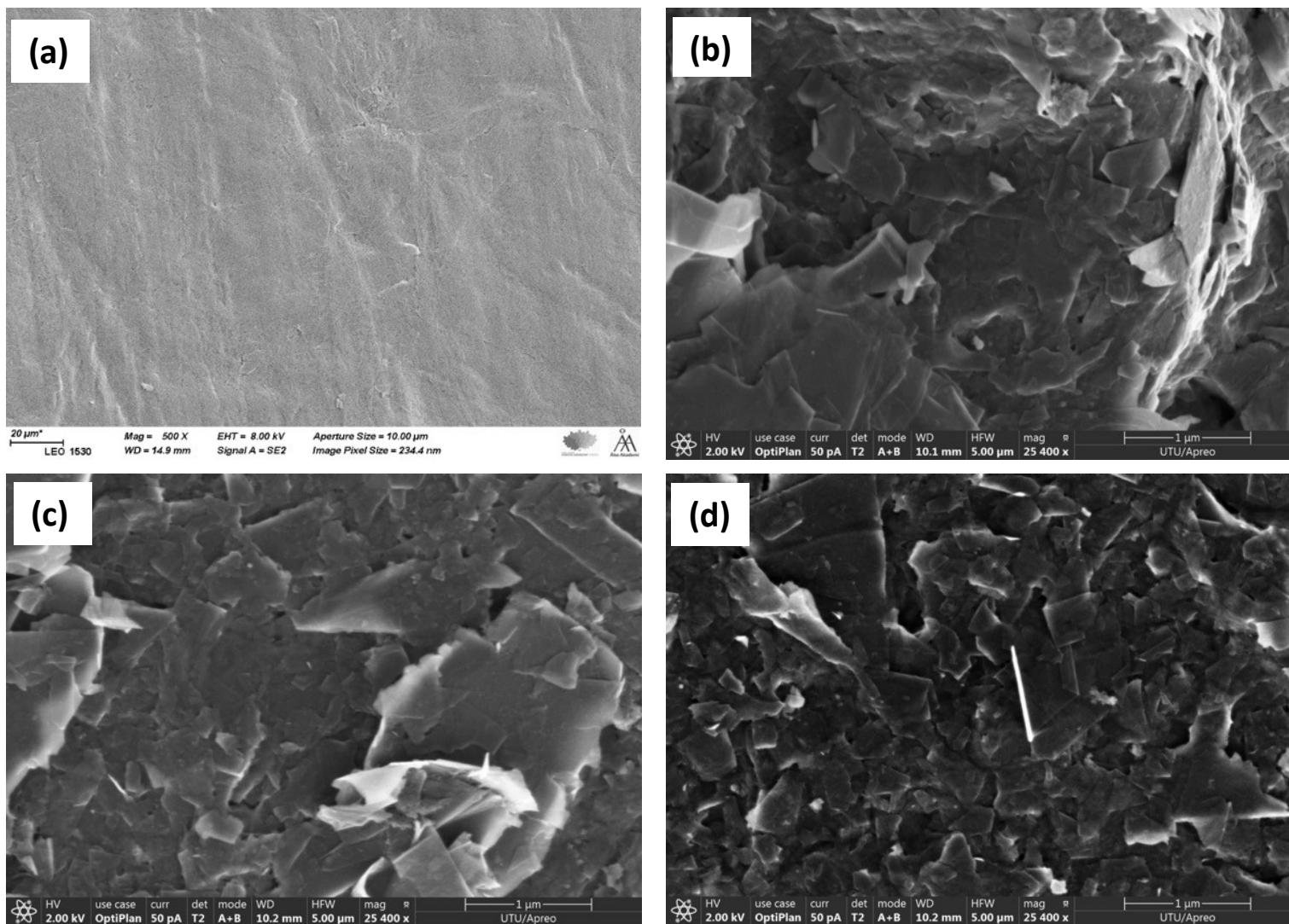


Figure 18. High-magnification SEM images (top-view, 25400×) corresponding to the surfaces of (a) the graphite foil substrate, (b) G-CNC Batch 16, (c) Batch 19, and (d) Batch 31. Image (a) was taken only at 500× magnification.

A closer look at the electrode surface morphologies reveals a sheet-like nature of graphene as the active material (Figure 18). The graphene flakes are of varying length from hundreds of nm to 1 μm . These large flakes can pose an issue towards the ion accessibility for charge storage [34, 60]. The wide range of sheet dimensions of graphene highlights the limitations in controlling the sheet size with the liquid-phase exfoliation process [52]. There also exists a risk of re-stacking of the graphene sheets, which is why an intricate balance of graphene and CNC amount is necessary for the long-term stability of the composite. To this date, there are no detailed studies regarding the long-term stability of G-CNC films.

The high-magnification SEM images (Figure 19) also display to some extent the cellulose nanocrystals as rod-like crystals with size less than 1 μm . It is expected that the visible crystals are minimal and that the actual crystals on the surface would be better characterised with other imaging techniques (e.g., Transmission Electron Microscopy). In addition, the CNCs are expected to intercalate between the graphene layers to keep them separated.

Cross-sectional SEM images illustrate the thicknesses of the G-CNC layers on the graphite foil to range from 5 to 80 μm (Figure 20). This thickness range is comparable to reported film thicknesses for EDLC electrodes [96, 112]. The thickest film was observed with the G-CNC Batch 16 ($\sim 80 \mu\text{m}$, see Appendix C) due to its 3D porous structure and high graphene concentration, whereas G-CNC Batches 19 ($\sim 5 \mu\text{m}$) and 31 ($\sim 10 \mu\text{m}$) had thinner and denser cross-sectional areas. Batch 31 had a 2D stacking orientation of the graphene sheets with fewer 3D defects. The film thicknesses relative to each G-CNC electrode vary throughout the electrode's area as a cause of manual variations in the G-CNC film application. The cross-section image in Figure 20c shows that the thinnest G-CNC film from Batch 19 had better contact with the graphite foil substrate compared to the other films. A good contact is essential to minimize the EDLC series resistance.

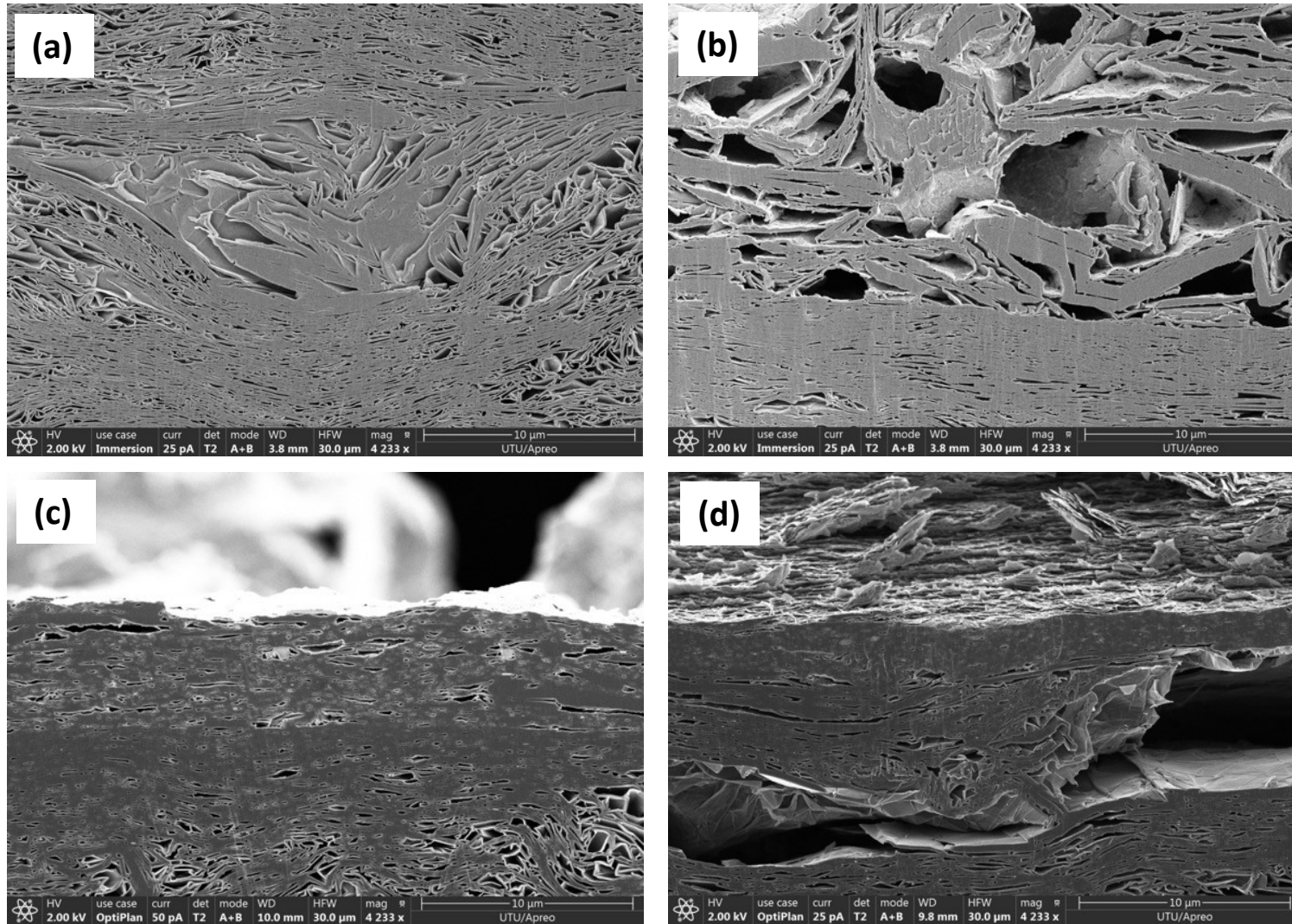


Figure 19. Cross-sectional SEM images (4233 \times) corresponding to (a) the graphite foil substrate, (b) G-CNC Batches 16, (c) Batch 19, and (d) Batch 31.

Elemental analysis of the G-CNC electrode's surface with EDX provides information regarding the G-CNC film purity (Appendix C). Elemental oxygen was the second most abundant element in the composite which can be linked to the nanocellulose hydroxyl groups. Carbon-to-oxygen ratios of G-CNC electrode surfaces were also determined from the EDX data (21.7 – Batch 16, 12.5 – Batch 19, 16.4 – Batch 31). When compared to the TGA results (Section 4.2.2), there is a discrepancy between the carbon:oxygen ratios and the amount of CNC obtained in the dispersion, particularly with Batches 19 and 31. However, such discrepancy remains to be determined if they are significant. Moreover, surface elemental composition does not entirely represent the G-CNC composition in the electrodes. The obtained ratios, however, can be linked to the obtained graphene concentrations via UV-Vis.

Traces of Si, Fe, Al, and other inorganic elements were also detected in all the films which appear as irregular particles (<1 μm) in the SEM images (represented in Figure 20). These impurities are suspected to originate from the high-shear exfoliation procedure or from the source of the natural graphite flakes as these particles were only observed on the G-CNC layer of the electrodes.

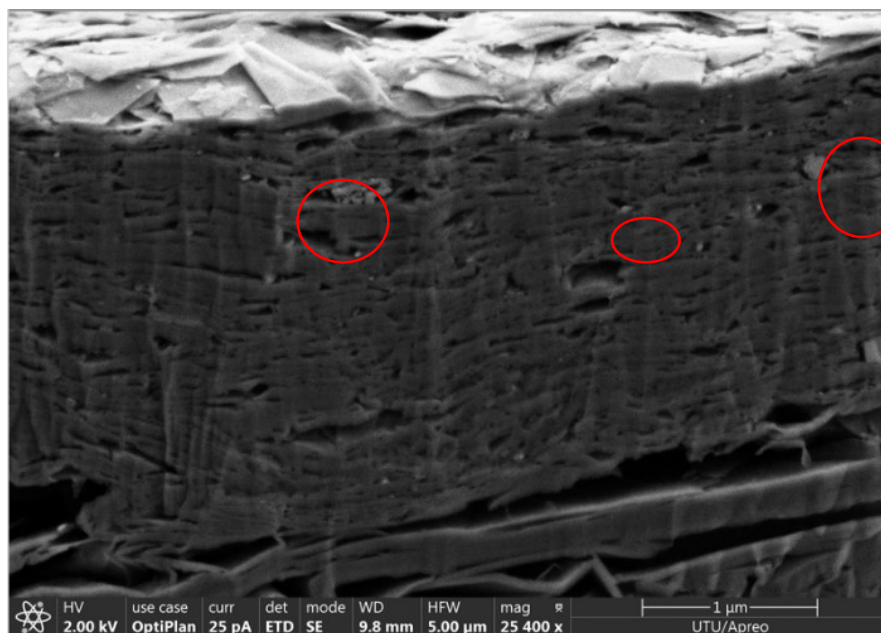


Figure 20. A representative, cross-sectional SEM image for visualisation of metal impurities in the G-CNC Batch 31 composite. Regions with some present impurities are encircled in red.

4.2.4 Determination of Electrical Conductivity

One of the important considerations for electrode materials for EDLCs is the material's electrical conductivity as this helps to provide the device with greater charge-discharge efficiency and power density [22]. The four-point probe technique is a typical tool for such kind of assessment. The electrical conductivity estimates for G-CNC films made by the different G-CNC dispersion batches are presented in Table 5:

Table 5. Electrical conductivity estimates of different G-CNC composite batches along with their corresponding film thicknesses, obtained via AFM.

G-CNC Batch	Initial graphite-to-CNC ratio (w/w)	Graphene Concentration (mg·mL⁻¹)	Film Thickness (nm)*	Electrical Conductivity (S·cm⁻¹)**
12	8.6:1 (undil.)	14.4	1140	10.1
16	15:1	13.3	1743	5.3
19	15:1	6.1	—	1.9
31	15:1	10.8	—	1.8

*Film thickness was estimated from AFM line profiles that have points which are less than 5 μm ; these are likely underestimated values.

**As there were no good representative AFM images, the electrical conductivities were calculated on the assumption of uniform thickness at the AFM thickness limit of 5 μm ; for comparison of between-batch variations only. $N = 2$ for the four-point probe measurements.

AFM was used to evaluate the G-CNC microstructure as well as to estimate the thickness of the G-CNC films on a glass substrate. The film thickness assessment was used for calculation of the electrical conductivity. However, AFM images acquired for the G-CNC batches have irregularities in the surface topography. These correspond to G-CNC film thicknesses greater than 5.0 μm , which is the AFM set-up's tolerance limit. It was difficult to estimate the film thicknesses from all G-CNC batches tested due to this reason, even at smaller spray-coating volumes (~ 0.05 mL per 6.25 cm^2). Therefore, it was not possible to acquire a reliable result for the electrical conductivity. Rough estimates of the parameter were still given under the assumption of uniform thickness, nonetheless (See Table 5 sidenote).

The obtained electrical conductivity estimates for all batches suggest that the G-CNC composites are conductive, despite the insulating nature of CNCs. The higher electrical conductivity of Batch 12 can be linked with the high graphene concentration, but the anomaly itself might reside on the reliability of the film thickness measurements. Even so, these results indicate that the films are sufficiently conductive to be applied as an electrode material in EDLCs and should only be taken as rough estimates. Furthermore, four-point probe measurements can also incur errors of up to 20 % when surrounded by a highly conductive material [90].

4.3 Electrochemical Properties of the G-CNC composites

The energy storage performance and electrochemical behaviour of the G-CNC dispersions as EDLC electrode materials were determined as the physico-chemical characterisations established, to some extent, the suitability of the G-CNC composite as an active material in EDLCs. The electrochemical performance of the electrodes made of G-CNC batches 16, 19, and 31 was studied.

4.3.1 Cyclic Voltammetry

Electrochemical characterisation via CV permits visualisation of the electrochemical processes present in the EDLC cell, with the assumption of no Faradaic processes taking place in the system. To fundamentally characterise the properties on a single, G-CNC electrode, the three-electrode set-up was used. The electrode mass loadings in these experiments ranged from 1.9 to 7.1 mg·cm⁻². Figure 21 illustrates the CV profile of the graphite foil substrate, compared to that of the G-CNC film (Batch 19) on graphite foil used as the working electrode.

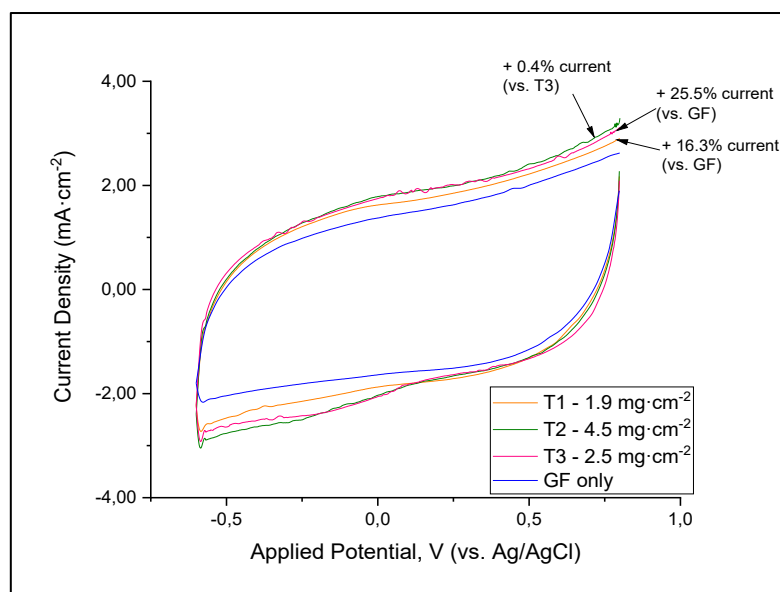


Figure 21. Comparative three-electrode CV profiles illustrating the effect of the G-CNC mass loading increase to the current density. The CV scans were performed at $50 \text{ mV}\cdot\text{s}^{-1}$ within a potential window of 1.2 V (vs. Ag/AgCl) for G-CNC Batch 19 electrodes.

The CV exhibits an almost rectangular profile, even at the wide potential window used (1.5 V). However, there is a steeper current increase at around +0.8 V vs. Ag/AgCl reference. This suggests that irreversible, electrochemical side reactions start to take place from that point and at higher voltage. It should be noted that this also occurred in the graphite foil substrate, eliminating the cause of G-CNC side reactions. Thus, the assignable cause was the water-splitting reaction in the electrolyte, which should theoretically occur at $\sim 1.02 \text{ V}$ vs. Ag/AgCl (1.23 V vs. normal hydrogen electrode). With those considerations, it can be established that the safe operational potential window for the G-CNC electrodes is 1.2 V.

Figure 21 also shows that the capacitive current due to the substrate has a significant contribution to the total current, when compared to that with the G-CNC layer. This indicates that the G-CNC composite had small impact on the double-layer capacitance. This effect is similar with G-CNC Batch 16, which generally had higher mass loadings ($\sim 2.4 - 2.7 \text{ mg}\cdot\text{cm}^{-2}$) for the same amount of coating volume on the substrate. The coating volume was limited by the yields obtained from the G-CNC preparation and the poor reproducibility of the preparation procedure in respect to the graphene and CNC relative concentrations. A G-CNC mass loading of 1.4 mg increases the current density by $\sim 16 \%$ with respect to pure graphite foil. Furthermore, a 36% increase in the initial mass load (T3 vs. T1) translates to current

increase by ~8% (estimated from the CV curve areas in Figure 21). The added current, however, reaches a limit where more G-CNC load does not significantly improve the current (+0.4% total current with T2 vs T3). This trend was later observed as well during the two-electrode experiments.

What was also noticeable in the CVs measured with the three-electrode set-up is the appearance of small, broad peaks at $\sim +0.2$ V (oxidation) and ~ -0.2 V (reduction) versus Ag/AgCl, particularly in Batch 16 (Figure 22). It is suspected that this is pseudocapacitive behaviour from the reaction of the perchlorate electrolyte with the CNCs. Previous studies have shown that sulfonic groups are prone to redox activity around the same potential range [118] and that the oxidation of hydroxyl groups in cellulose is possible in presence of perhalates, cleaving the anhydroglucose units and the sulphate half-ester groups, thereby decreasing the CNC's crystallinity [22, 112, 113]. However, this “pseudocapacitive” behaviour faded over increased number of cycles. These broad peaks were not apparent in G-CNC Batch 19 having a lower percentage of CNC in comparison to graphene.

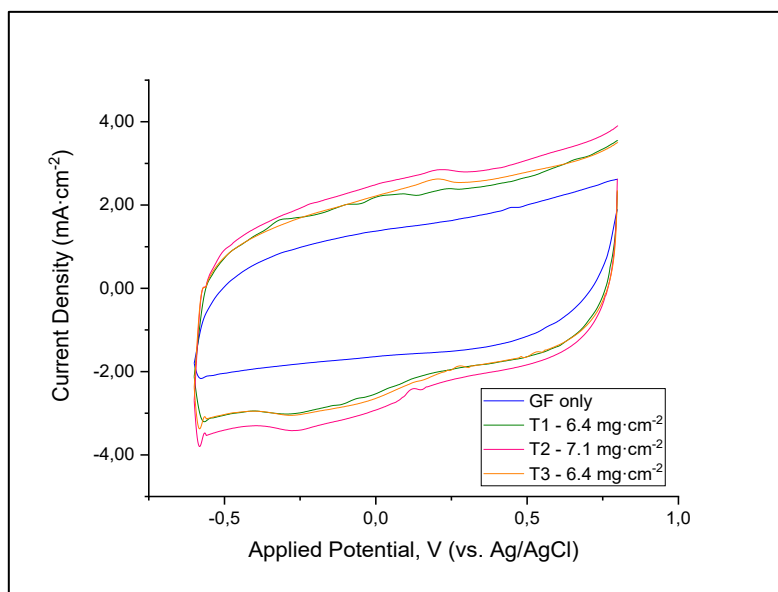


Figure 22. Three-electrode CV profiles of G-CNC Batch 16 electrodes exhibiting pseudocapacitive behaviour through the presence of broad, redox peaks at ± 0.2 V (vs. Ag/AgCl). The CV scans were performed at $50 \text{ mV}\cdot\text{s}^{-1}$.

Overall, the three-electrode CV experiments suggest that the G-CNC as an electrode material can sustain aqueous electrolyte-based EDLC systems of up to 1.2 V with some limitations. The surface functional groups on CNC may introduce irreversible reactions during initial charge-discharge cycles, depending on the amount of CNC present at the surface as well as the choice of electrolyte solution. Moreover, the increase in the G-CNC mass loading does not significantly increase the specific capacitance of a single electrode (Figure 21). This may be attributed to the relatively low mass loading of G-CNC or to the poor porosity of the graphene sheets on the electrode.

CV experiments with the two-electrode set-up were carried out for performance verification. Three (3) different batches (Batches 16, 19, and 31) of G-CNC have been used as electrode active materials and were considered for this analysis. The other batches have been used for electrochemical set-up optimisation or have been mixed to create a batch of higher volume. It must be said from here on that only one replicate of G-CNC Batch 19 using the all-stainless steel, two-electrode test cell was carried out due to limited availability of the G-CNC batch. For the purpose of having replicate measurements, one replicate from the previously tested, Al-SS test cell was used with slightly less (3 mL) amount of electrolyte to eliminate Al surface passivation effects.

Representative CVs of the experiments are provided in Figure 23, and it can be seen in Figure 23a and 23b that the current increases with increasing scan rate due to the greater ion flux towards the electrode surface. The effect is that smoother CV profiles are evident at higher scan rates, but at the expense of increased overall resistance. The increased resistance is shown as upward drifting of the current and the more pronounced curving of the CV profile for each cycle.

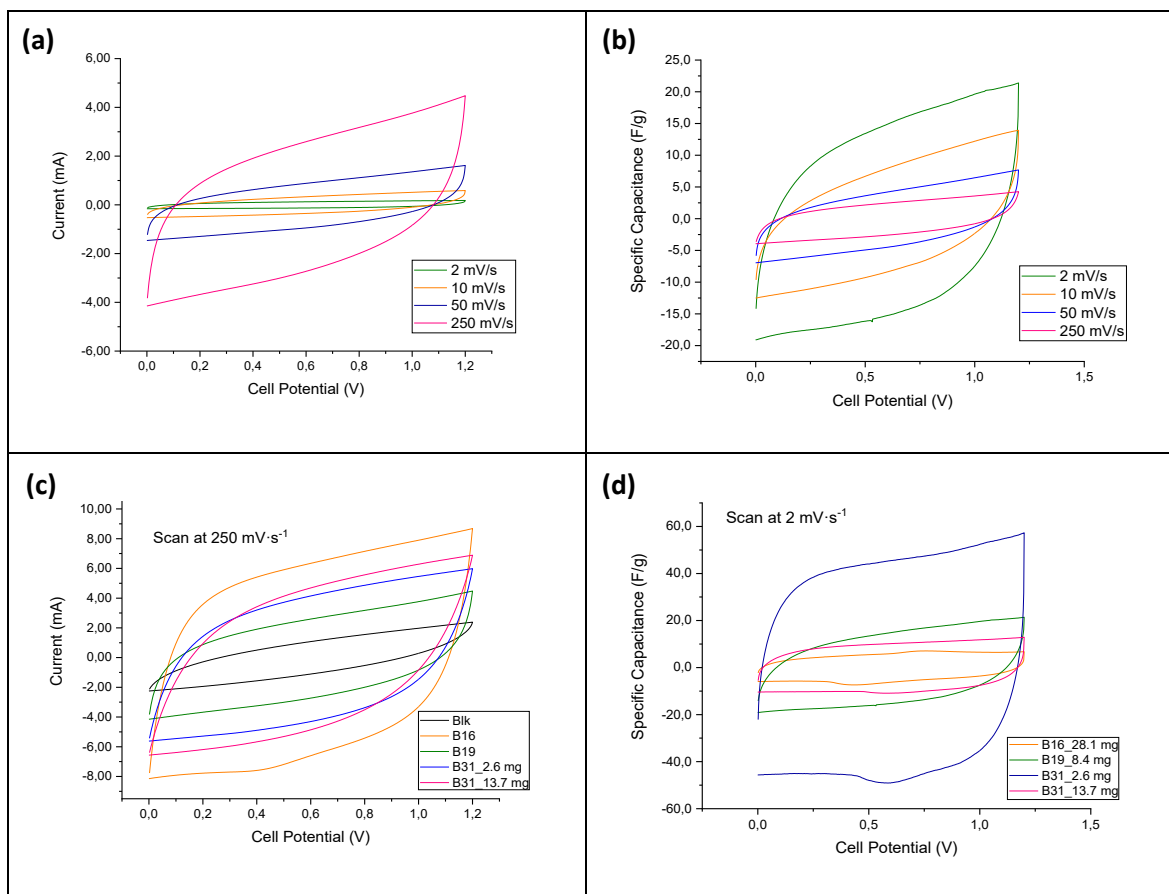


Figure 23. Representative two-electrode CV curves for G-CNC electrodes at (a, b) varying scan rates using G-CNC Batch 19 and its comparison against other G-CNC batches (c, d) as a function of current and specific capacitance. The plots are expressed as average of two replicates for each G-CNC batch, except for Batch 31.

Figure 23c illustrates the contribution of the G-CNC to the total current generated, as well as its effect due to differences in the graphene concentration. Here it is shown that the total current increases with the increase in graphene concentration. In this case, Batch 16 exhibited the highest current which can be assigned to its higher concentration of graphene and its relatively more porous, 3D structure compared to Batches 19 and 31. There is no clear impact of adjusting the pH of the CNC suspension for Batch 31 on the electrochemical performance, suggesting that the pH change would only have an indirect impact on the charge storage by changing the graphene concentration.

Profile-wise, Batches 19 and 31 exhibited a near-rectangular profile that closely resembles that of an ideal EDLC (Figure 23d). Batch 16 exhibited small Faradaic peaks observed at ~ 0.88 V (oxidation) and ~ 0.44 V (reduction). This suggests that there could be a

pseudocapacitive contribution from the nanocellulose present at the electrode surface. This can originate from the redox reaction of the hydroxyl groups on nanocellulose which have been previously shown to exhibit such phenomenon in the three-electrode experiments. It is likely that the number of Faradaic reaction sites are less apparent on the two other batches (Batch 19 and 31), with Batch 31 exhibiting irreversible, Faradaic reductions in the initial twenty (20) cycles.

The average specific capacitance of an EDLC electrode is highly dependent on the mass of the active material. It should be noted that the variations in the mass loadings are not regulated and depend on the graphene concentrations and the manual application of the spray-coating process. In the case of the graphene-CNC electrodes, a limit in the amount of charge that can be stored is apparent with the increase in the mass loading. This is shown in Figure 23d with Batch 31 giving the higher C_s value of $\sim 45 \text{ F}\cdot\text{g}^{-1}$ at $\sim 2 \text{ mg}$ G-CNC load compared to $\sim 9.0 \text{ F}\cdot\text{g}^{-1}$ at $\sim 13.7 \text{ mg}$ G-CNC load. Higher G-CNC loadings obtained for the other batches have significantly decreased the C_s values down to $< 10 \text{ F}\cdot\text{g}^{-1}$ at $2 \text{ mV}\cdot\text{s}^{-1}$ scan rate. The scan rate dependence of C_s would even exacerbate the C_s down to $< 1 \text{ F}\cdot\text{g}^{-1}$ for $250 \text{ mV}\cdot\text{s}^{-1}$ CV scans (Figure 24).

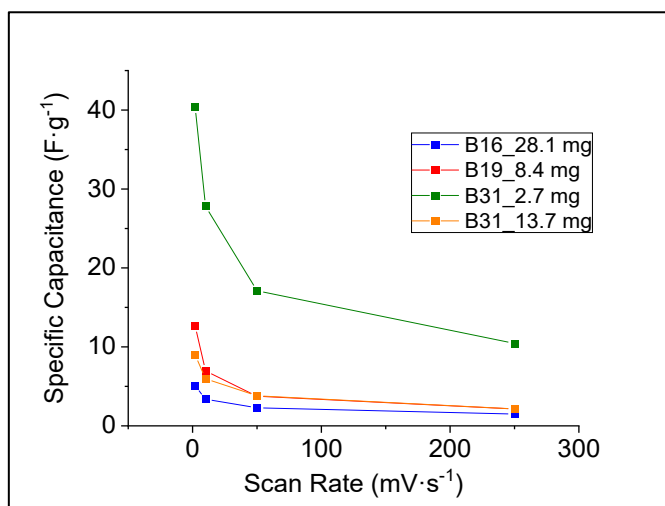


Figure 24. Capacitance retention curves for different batches of G-CNC electrodes as a function of CV scan rate. The calculated capacitance values are taken as average of two replicates, except for G-CNC Batch 31.

Several causes can be assigned for these results, one being the morphology of the G-CNC which is not porous enough for the ions to pass through, thus fewer sites for electrical double-layer formation. The G-CNC structure contains flat and dense graphene sheets which, when bound by CNC, lessen the available double-layer sites, and resemble that of re-stacked graphene sheets. This was also verified by the cross-sectional SEM images. Another reason is the low amount of G-CNC on the graphite foil (in Batch 31) which might have led to an overestimated C_s due to heightened mass measurement uncertainties. In addition, the large variations in the GF substrate weight (RSD = 4.4%) also puts into question the estimated active material weights. It has been recommended in practical applications that the active material mass loading should be sufficiently high to increase energy density [22, 112], with even a recommendation of orders around at least 10 mg [100] or between 1 to 10 mg·cm⁻² [114].

Finally, the significant scan rate dependence of C_s can be attributed to the contributions from the graphite foil substrate on the electrode's overall capacitance. As demonstrated by the three-electrode experiments, the graphite foil contributes largely to the total current, depending on the G-CNC mass loading. On the other hand, directly subtracting the amount of charge stored by the graphite foil substrate from the total charge obtained would lead to underestimations of the determined C_s .

4.3.2 Galvanostatic Charge-Discharge

The prepared G-CNC dispersions of the three different batches were characterised with twenty (20) cycles of GCD at three different current densities (0.1, 0.5, and 1.0 A·g⁻¹). The calculated specific (discharge) capacitances are calculated from the last charge-discharge cycle. In all batches, the GCD triangular profile was consistent from the second cycle onwards, suggesting its good cyclability. However, the profiles in general, vary between the three batches (Figure 25).

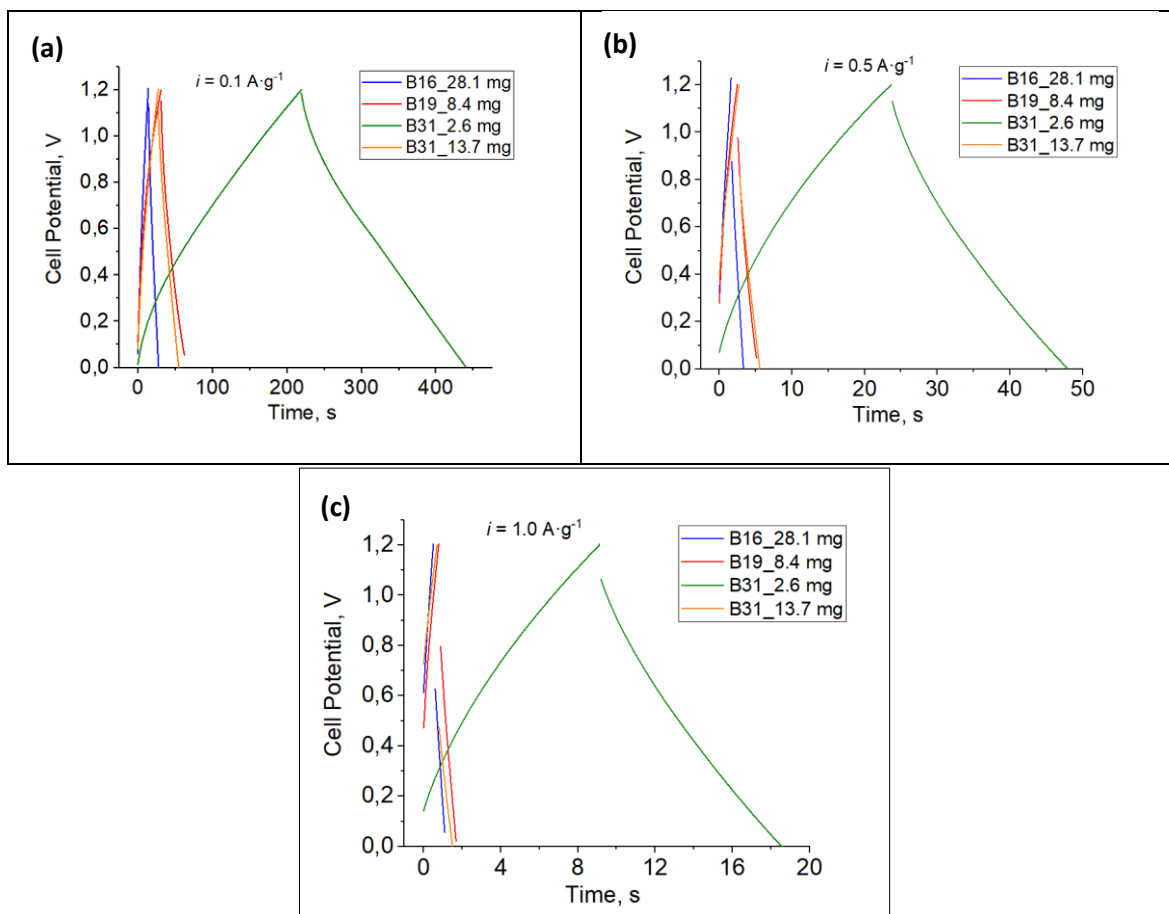


Figure 25. Galvanostatic charge-discharge cycles at three current densities, (a) $i = 0.1 \text{ A}\cdot\text{g}^{-1}$, (b) $i = 0.5 \text{ A}\cdot\text{g}^{-1}$, and (c) $i = 1.0 \text{ A}\cdot\text{g}^{-1}$ for three batches of G-CNC composite electrodes with their corresponding mass loadings. The 20th cycle was used for each run in this illustration.

What is worth noting between the batches are the differences in the symmetry of the charge-discharge profiles. The three batches, to some extent, exhibit an asymmetric profile which becomes more apparent from $0.5 \text{ A}\cdot\text{g}^{-1}$ where the iR drop becomes larger. These asymmetries would correspond to pseudocapacitive contributions from the electrode surface redox reactions brought by the CNCs. The large iR drop can be attributed to the internal resistance from the electrode-electrolyte interface wherein the electrolyte ion transport is dependent on the electrode's surface uniformity and wettability [115, 116]. It might also be that the overall conductivity of the electrode layer is compromised due to the surface irregularities on its surface. These effects were evident with the GCD profile of Batch 31 electrodes having the smallest iR drop since its surface in the macroscopic scale was more uniform than in the other batches (SEM images on Figure 17), and that the lower G-CNC load is expected to have better wettability to aid faster ion transport.

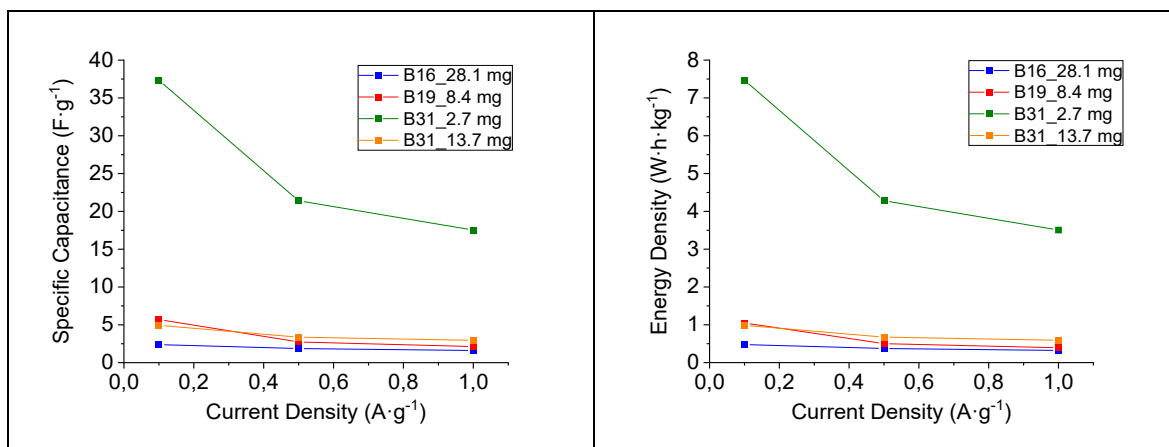


Figure 26. Capacitance retention (left) and energy density (right) plots as a function of current density for various G-CNC electrodes with their corresponding mass loadings.

In terms of specific capacitance, it is understandable that its value decreases at increasing current density as there is more significant contribution of the ohmic polarisation and smaller accessible capacity (charge stored) at higher discharge rates. The rate of decrease of the specific capacitance and energy density becomes more significant from 0.1 to 0.5 A·g⁻¹ (Figure 26). The obtained C_s values are comparable to those obtained with the two-electrode CV analysis, with the G-CNC Batch 31 at a lower mass loading of ~1 mg·cm⁻² having a significantly higher capacitance of ~37 F·g⁻¹ than the other G-CNC electrodes. These differences between the G-CNC batches were also observed in their respective power densities (Table 6). The power density calculations are reliable in magnitude under the assumption of zero (or minimal) *iR* drop.

Table 6. Calculated power densities of a single electrode for different G-CNC electrode batches tested with GCD in two-electrode set-up.

G-CNC Electrode Batch	<i>P</i> (kW·kg ⁻¹)
16	8.0
19	25.0
31_2.7 mg	86.2
31_13.7 mg	16.4

*R_{ESR} ~0.8 Ω for all electrodes, value obtained from EIS testing.

Determining the energy efficiency of an EDLC electrode allows us to determine if the charge and discharge mechanisms occur at the same rate. For the prepared G-CNC electrodes, energy efficiencies of less than 75 % at $0.1 \text{ A}\cdot\text{g}^{-1}$ are achieved (Figure 27). Likewise with the CV results, the increase in the mass loading decreases the energy efficiency. However, G-CNC Batch 16 electrodes had considerably greater efficiencies than Batch 19 electrode and 31 electrodes with a higher mass loading.

These obtained energy efficiencies are relatively low when compared to previously reported papers on graphene-based EDLC electrode materials [46, 63–66, 114, 117, 118]. From these results, one can see that the energy storage inefficiencies are greatly influenced by the G-CNC's intrinsic properties.

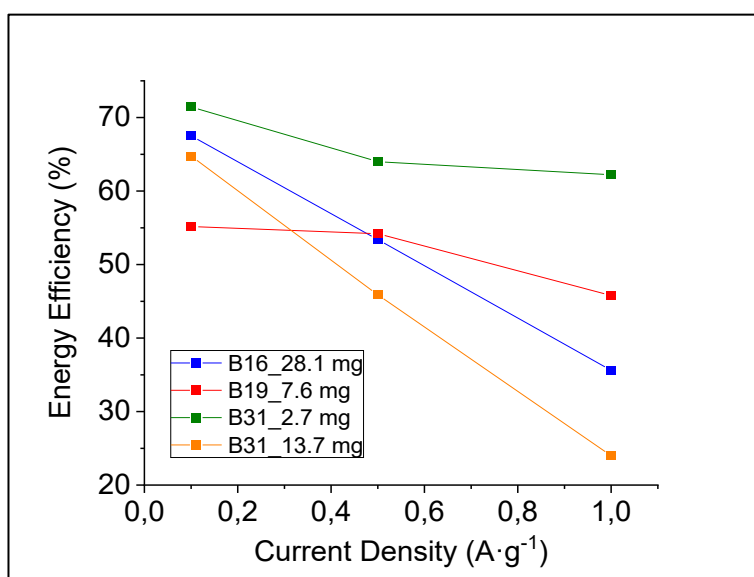


Figure 27. The energy efficiency plot against current density for different batches of G-CNC electrodes and their corresponding mass loadings. All batches tested for GCD are included in this figure for better comparison.

4.3.3 Electrochemical Impedance Spectroscopy

The modelling of the electrochemical system is characterised by EIS. Experimental Nyquist plots were obtained from a single, two-electrode cell set-up at fixed cell potential of 0.0 V at 10 mV AC perturbation. EIS was performed at different stages of the electrochemical measurements – (1) before initial charging-discharging with CV (at near-equilibrium), (2) after CV run, and (3) after GCD run [Overall scheme: EIS -> CV -> EIS -> GCD -> EIS]. This was made in order to be able to monitor any significant changes to the electrode material's stability after applying high-magnitude perturbations.

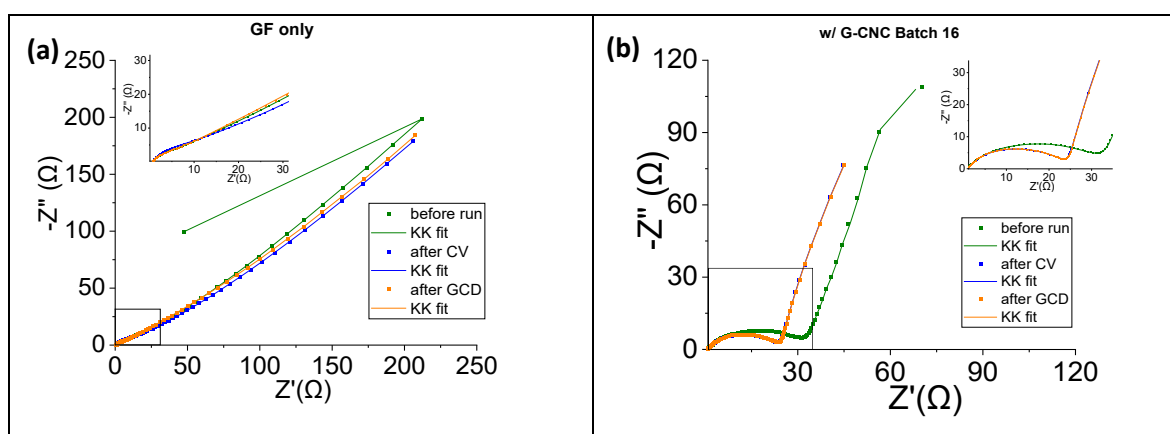


Figure 28. Nyquist plots at different stages of the electrochemical measurements for (a) the graphite foil substrate and (b) with the added G-CNC composite Batch 16 (for representation). The inset shows a close-up image of the high-frequency impedance values and their corresponding Kramers-Kronig (KK) fits. The last data point corresponds to AC frequency of 0.1 Hz.

Figure 28 illustrates the differences on the impedance profile with the addition of the G-CNC composite. In general, the system impedance had reduced upon the applying charge-discharge potential/currents to the cell, with minimal differences after running both the CV and the GCD. This indicates that the G-CNC electrodes are sufficiently conditioned for the regulated passage of ions through the G-CNC microstructure. This was also evident on the larger deviations with the Kramers-Kronig (KK) fitting at the low-frequency regions.

When it comes to elucidating electrochemical processes, the total internal resistance (ESR) of the cell is relatively low, $<1.0 \Omega$, for both the GF substrate and the substrate with the G-

CNC composite. This is important as the ESR should be as low as possible as this affects the distribution of the stored energy and thereby affects the energy efficiency and the power performance [8, 119]. The G-CNC composite addition had increased the system ESR by 20 % due to the added physical barrier by the G-CNC. This, however, is compensated by a lower overall impedance with the G-CNC by more than 50 %.

Both the GF substrate and the G-CNC electrodes exhibit semi-infinite diffusion-impedance, as shown by the 45° line towards lower AC frequencies. What is noticeable upon the addition of the different batches of G-CNC is the semi-circle formation in the intermediate frequency region which would correspond to charge transfer resistance (R_{ct}) from the G-CNC surface redox reactions. This is consistent with the observation from the CV experiments wherein small, Faradaic peaks were observed.

The semi-circle formation can also be attributed to the interfacial contact resistance between the graphite foil and the G-CNC composite. The contact resistance could arise from the surface passivation on the GF current collector which limits the ohmic coupling with the G-CNC. However, this phenomenon can only be confirmed by applying various DC potentials to the test cell, which has not been performed in this study. A constant magnitude of the semi-circle radius at various DC potentials would indicate that it is due to contact resistance, rather than an actual charge transfer process [8]. This contact resistance could then be minimised by ensuring a more uniform electrode surface and a thinner substrate/current collector. In this study, one should also consider the surface uniformity of the separators used, as the cellulose filter papers used had creases, per commercial specifications.

Another region to consider is the <90° line of semi-infinite length observed from the $f = 5-8$ Hz which is a profile that is typical to ideal double-layer capacitance. This can be designated as a constant phase element (CPE) in the system where the phase angle is frequency-dependent in the measurements and represents the non-ideal behaviour in an electrochemical system element to be independent of the frequency [94]. This occurs because of multiple factors such as the CPE behaviour inherent from the graphite foil itself (Figure 28a) or the inhomogeneity of the electrode surface due to the surface roughness and the degree of

crystallinity of the composite. Typically, rougher electrode surfaces deviate more from the ideal capacitive behaviour as it involves uneven current density distributions which limits the effective local solution resistance at the surfaces [120, 121]. The exact source(s) of the CPE in the case of the G-CNC electrodes is/are unknown and is outside of the research scope of this study.

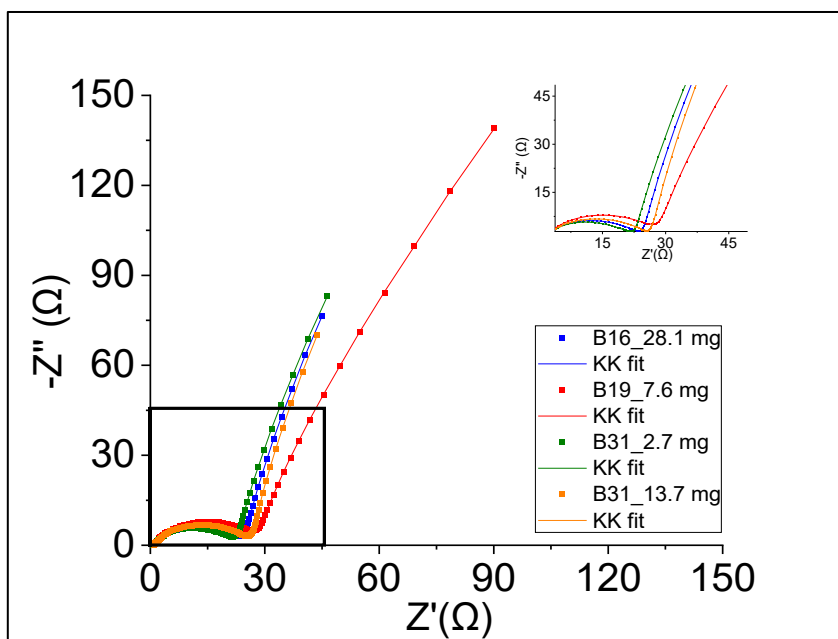


Figure 29. Experimental Nyquist plots for G-CNC electrodes from the different batches tested with an all-SS, two-electrode test cell. Measurements were obtained after GCD run. The inset shows a close-up image of the high-frequency impedance values and their corresponding fits. The last data point corresponds to AC frequency of 0.1 Hz.

Along with the approximately similar ESR values, the charge transfer (Faradaic) resistance contribution for one of the Batch 19 electrodes was different than in the other two batches (Figure 29). The first reason is the varied set-up for one replicate of the Batch 19 with the Al-SS test cell (see Appendix D) and smaller electrolyte amount (~3 mL), which translated to lower R_{ct} ~6 Ω (vs. 25 Ω for all-SS test cell at 3.5 mL 1.0 M NaClO₄). The other reason can be attributed to the lower concentration of the graphene sheets (Table 2, page 26) on the composite's surface in Batch 19. This effect reflects on the other Batch 19 replicate, wherein it has a slightly higher R_{ct} (26 Ω) than the other G-CNC batches tested with the all-SS test cell. These differences in the R_{ct} between the different batches do not vary by a large magnitude (21-26 Ω for all G-CNC batches).

The average specific capacitance values determined from the three electrochemical techniques are compared and presented in Table 7. Variations in the values obtained with the three different techniques are mostly due to assumptions of ideal EDLC behaviour. Generally, the G-CNC Batch 31 electrodes exhibited the largest C_s , but at the dependence of the G-CNC mass loading. Increasing the active material mass on the electrode does not necessarily increase the amount of charge stored as this is limited by the stacking arrangements of the graphene sheets. It is therefore critical that the application of the G-CNC is controlled in an ordered manner that permits better ion transport. Nevertheless, the electrochemical characterisations have demonstrated that the G-CNC composite can act as an EDLC electrode material.

Table 7. Calculated average specific capacitance values for different G-CNC electrode batches for various electrochemical characterisation techniques.

G-CNC Electrode Batch	C_s, CV ($F \cdot g^{-1}$)	C_s, GCD ($F \cdot g^{-1}$)	C_s, EIS ($F \cdot g^{-1}$)
16	5.1	2.4	2.1
19	12.7	5.7	3.1
31	40.4 (2.7 mg)	37.3 (2.7 mg)	14.7 (2.7 mg)
	8.9 (13.7 mg)	4.9 (13.7 mg)	3.3 (13.7 mg)

C_s calculation via CV - taken at $2 \text{ mV} \cdot \text{s}^{-1}$ scan rate; C_s calculation via GCD – taken at $0.1 \text{ A} \cdot \text{g}^{-1}$ current density; C_s calculation via EIS – taken after CV run at 0.1 Hz AC frequency.

5. CONCLUSIONS AND OUTLOOK

The formulation of graphene-cellulose nanocrystal composites (G-CNC) and its evaluation as an electrode material for electrochemical double-layer capacitors (EDLCs) has been reported. The graphene sheets were prepared by high-shear exfoliation of graphite flakes, in which cellulose nanocrystals acts as the dispersant via their negatively charged sulphate ester groups and their hydrophobic moieties. The prepared G-CNC dispersions were then spray-coated onto graphite foil substrates and served as the EDLC electrodes.

Analysing the G-CNC material's morphology and composition reveal the differences in the obtained dispersions using the same amounts of the composite precursors. These differences are assignable to the variations in the conditions of the high-shear exfoliation, thereby producing some G-CNC dispersions with partially exfoliated graphite present along with the composite. These impurities, along with the elemental impurities, have added porosity to the G-CNC's microstructure, at the expense of the overall conductivity of the electrodes. The prepared G-CNC electrodes that have a smooth, uniform surface show the 2D stacking arrangement of the graphene flakes which impedes ion transport needed for double-layer capacitance.

All these material-related influences have manifested in the electrochemical evaluation of the EDLC electrodes. The magnitude of charge storage is limited by the high G-CNC mass loadings, which are comparable to those applied by current EDLC industries ($\sim 1-10 \text{ mg}\cdot\text{cm}^{-2}$) [114]. The G-CNC electrodes were demonstrated to exhibit a maximum specific capacitance of $\sim 40 \text{ F}\cdot\text{g}^{-1}$, with an energy density of $\sim 8 \text{ W}\cdot\text{h}\cdot\text{kg}^{-1}$ and a power density of $\sim 86 \text{ kW}\cdot\text{kg}^{-1}$. These obtained values come with a low energy efficiency of $\sim 75 \%$, signifying that improvements in developing the G-CNC as an electrode material are still needed. Divergence from ideal EDLC behaviour is a result of significant contact resistance between the substrate and the film, defects and impurities at the electrode surface, and surface redox activity from the CNCs and the electrolyte solution used.

Overall, the suitability of the G-CNC composite as an EDLC electrode material would still require further optimisation in its processing and electrode preparation. From this study, it is known that modifications in the EDLC test cell components (e.g., thinner substrate, electrolyte of choice, mass loading) as well as in the spray-coating process could potentially improve the capacitance of the material and its energy efficiency.

It is still of significant challenge in industry-scale applications to use graphene and its derivatives as an active material for EDLCs due to the detrimental effects of its re-stacking, its horizontally aligned, sheet-like nature, and currently, more expensive production [34]. However, graphene's high conductivity can still be harnessed for its integration with more porous materials to achieve the suitable balance of porosity and conductivity needed for commercial EDLCs. Projections show graphene's potential commercial use as "micro-supercapacitors" for applications in wearable microelectronics [122, 123]. It is therefore worthwhile to consider the production of the G-CNC composite through high-shear exfoliation as a key step towards greener production of EDLCs.

REFERENCES

- [1] ‘Country Reports’, Accessed: Mar. 24, 2023. [Online]. Available: <https://ym.fi/en/climate-neutral-finland-2035>
- [2] ‘Critical raw materials’. https://single-market-economy.ec.europa.eu/sectors/raw-materials/areas-specific-interest/critical-raw-materials_en (accessed Jun. 22, 2023).
- [3] Z. L. Wang, D. Xu, H. X. Zhong, J. Wang, F. L. Meng, and X. B. Zhang, ‘Gelatin-derived sustainable carbon-based functional materials for energy conversion and storage with controllability of structure and component’, *Sci Adv*, vol. 1, no. 1, Feb. 2015, doi: 10.1126/SCIADV.1400035/SUPPL_FILE/1400035_SM.PDF.
- [4] Q. Ma, Y. Yu, M. Sindoro, A. G. Fane, R. Wang, and H. Zhang, ‘Carbon-Based Functional Materials Derived from Waste for Water Remediation and Energy Storage’, *Advanced Materials*, vol. 29, no. 13, p. 1605361, Apr. 2017, doi: 10.1002/ADMA.201605361.
- [5] J. Libich, J. Máca, J. Vondrák, O. Čech, and M. Sedlaříková, ‘Supercapacitors: Properties and applications’, *J Energy Storage*, vol. 17, pp. 224–227, Jun. 2018, doi: 10.1016/J.EST.2018.03.012.
- [6] F. Naseri, S. Karimi, E. Farjah, and E. Schaltz, ‘Supercapacitor management system: A comprehensive review of modeling, estimation, balancing, and protection techniques’, *Renewable and Sustainable Energy Reviews*, vol. 155, p. 111913, Mar. 2022, doi: 10.1016/J.RSER.2021.111913.
- [7] T. F. Fuller and J. N. Harb, *Electrochemical Engineering*, 1st ed. Hoboken, NJ, USA: John Wiley & Sons, Inc., 2018.
- [8] T. S. Mathis, N. Kurra, X. Wang, D. Pinto, P. Simon, and Y. Gogotsi, ‘Energy Storage Data Reporting in Perspective—Guidelines for Interpreting the Performance of Electrochemical Energy Storage Systems’, *Adv Energy Mater*, vol. 9, no. 39, Aug. 2019, doi: 10.1002/AENM.201902007.
- [9] W. Zhang, J. Liu, and B. A. Mei, ‘Analysis of Energy Loss and Heat Generation Characteristics of Supercapacitors’, *Lecture Notes in Electrical Engineering*, vol. 1016 LNEE, pp. 272–280, 2023, doi: 10.1007/978-981-99-1027-4_29/COVER.
- [10] W. Shang *et al.*, ‘Insight into the self-discharge suppression of electrochemical capacitors: Progress and challenges’, *Advanced Powder Materials*, vol. 2, no. 1, p. 100075, 2022, doi: 10.1016/j.apmate.2022.100075.
- [11] I. S. Ike, I. Sigalas, and S. Iyuke, ‘Understanding performance limitation and suppression of leakage current or self-discharge in electrochemical capacitors: a review’, *Physical Chemistry Chemical Physics*, vol. 18, no. 2, pp. 661–680, Dec. 2015, doi: 10.1039/C5CP05459A.
- [12] H. Yang and Y. Zhang, ‘Analysis of supercapacitor energy loss for power management in environmentally powered wireless sensor nodes’, *IEEE Trans Power Electron*, vol. 28, no. 11, pp. 5391–5403, 2013, doi: 10.1109/TPEL.2013.2238683.

- [13] ‘Cyclic Voltammetry, EIS, Leakage Current-Testing Electrochemical Capacitors Gamry Instruments’. <https://www.gamry.com/application-notes/battery-research/testing-electrochemical-capacitors-cyclic-voltammetry-leakage-current/> (accessed May 03, 2023).
- [14] A. Laheäär, ‘Electrochemical characterization of alkali metal salt based non-aqueous electrolytes for supercapacitors’, Jun. 2013, Accessed: May 08, 2023. [Online]. Available: <https://dspace.ut.ee/handle/10062/31461>
- [15] M. Härmas, ‘Impact of activated carbon microstructure and porosity on electrochemical performance of electrical double-layer capacitors’, Jul. 2020, Accessed: May 08, 2023. [Online]. Available: <https://dspace.ut.ee/handle/10062/68504>
- [16] F. D’Souza and K. M. Kadish, *Handbook of Carbon Nano Materials*, vol. 5: Graphene-Funda.... in World Scientific Series on Carbon Nanoscience, vol. 5: Graphene-Funda.... WORLD SCIENTIFIC, 2014. doi: 10.1142/8979.
- [17] J. Yan *et al.*, ‘Rational Design of Nanostructured Electrode Materials toward Multifunctional Supercapacitors’, *Adv Funct Mater*, vol. 30, no. 2, p. 1902564, Jan. 2020, doi: 10.1002/ADFM.201902564.
- [18] P. Ratajczak, M. E. Suss, F. Kaasik, and F. Béguin, ‘Carbon electrodes for capacitive technologies’, *Energy Storage Mater*, vol. 16, pp. 126–145, Jan. 2019, doi: 10.1016/J.ENSM.2018.04.031.
- [19] R. S. Dhillon, ‘CRC Handbook of Chemistry and Physics, 88th ed Editor-in-Chief: David R. Lide (National Institute of Standards and Technology) CRC Press/Taylor & Francis Group: Boca Raton, FL. 2007. 2640 pp. \$139.95. ISBN 0-8493-0488-1.’, *J Am Chem Soc*, vol. 130, no. 1, pp. 382–382, Jan. 2007, doi: 10.1021/JA077011D.
- [20] C. Zhong, Y. Deng, W. Hu, J. Qiao, L. Zhang, and J. Zhang, ‘A review of electrolyte materials and compositions for electrochemical supercapacitors’, *Chem Soc Rev*, vol. 44, no. 21, pp. 7484–7539, Oct. 2015, doi: 10.1039/C5CS00303B.
- [21] T. S. Bhat, P. S. Patil, and R. B. Rakhi, ‘Recent trends in electrolytes for supercapacitors’, *J Energy Storage*, vol. 50, p. 104222, Jun. 2022, doi: 10.1016/J.EST.2022.104222.
- [22] C. Schütter, S. Pohlmann, and A. Balducci, ‘Industrial Requirements of Materials for Electrical Double Layer Capacitors: Impact on Current and Future Applications’, *Adv Energy Mater*, vol. 9, no. 25, p. 1900334, Jul. 2019, doi: 10.1002/AENM.201900334.
- [23] J. M. Baptista, J. S. Sagu, U. W. KG, and K. Lobato, ‘State-of-the-art materials for high power and high energy supercapacitors: Performance metrics and obstacles for the transition from lab to industrial scale – A critical approach’, *Chemical Engineering Journal*, vol. 374, pp. 1153–1179, Oct. 2019, doi: 10.1016/J.CEJ.2019.05.207.
- [24] L. Hu, H. Wu, Y. Cui, A. Phys Lett, and A. Mater, ‘Printed energy storage devices by integration of electrodes and separators into single sheets of paper’, *Appl Phys Lett*, vol. 96, no. 18, p. 183502, May 2010, doi: 10.1063/1.3425767.

- [25] N. Kumar, L. Pradhan, and B. K. Jena, 'Recent progress on novel current collector electrodes for energy storage devices: Supercapacitors', *Wiley Interdiscip Rev Energy Environ*, vol. 11, no. 1, p. e415, Jan. 2022, doi: 10.1002/WENE.415.
- [26] A. Abdisattar *et al.*, 'Recent advances and challenges of current collectors for supercapacitors', *Electrochem commun*, vol. 142, p. 107373, Sep. 2022, doi: 10.1016/J.ELECOM.2022.107373.
- [27] E. Josef, R. Yan, R. Guterman, and M. Oschatz, 'Electrospun Carbon Fibers Replace Metals as a Current Collector in Supercapacitors', *ACS Appl Energy Mater*, vol. 2, no. 8, pp. 5724–5733, Aug. 2019, doi: 10.1021/ACSAEM.9B00854/ASSET/IMAGES/MEDIUM/AE-2019-00854F_M002.GIF.
- [28] M. Arvani, J. Keskinen, D. Lupo, and M. Honkanen, 'Current collectors for low resistance aqueous flexible printed supercapacitors', *J Energy Storage*, vol. 29, p. 101384, Jun. 2020, doi: 10.1016/J.EST.2020.101384.
- [29] P. Luo and L. Huang, 'Carbon Paper as Current Collectors in Graphene Hydrogel Electrodes for High-Performance Supercapacitors', *Nanomaterials 2020, Vol. 10, Page 746*, vol. 10, no. 4, p. 746, Apr. 2020, doi: 10.3390/NANO10040746.
- [30] M. dos S. Klem, R. M. Morais, R. J. G. Rubira, and N. Alves, 'Paper-based supercapacitor with screen-printed poly (3, 4-ethylene dioxythiophene)-poly (styrene sulfonate)/multiwall carbon nanotube films actuating both as electrodes and current collectors', *Thin Solid Films*, vol. 669, pp. 96–102, Jan. 2019, doi: 10.1016/J.TSF.2018.10.029.
- [31] X. Shi *et al.*, 'Graphene-Based Linear Tandem Micro-Supercapacitors with Metal-Free Current Collectors and High-Voltage Output', *Advanced Materials*, vol. 29, no. 44, p. 1703034, Nov. 2017, doi: 10.1002/ADMA.201703034.
- [32] S. Baskakov *et al.*, 'Fabrication of current collector using a composite of polylactic acid and carbon nano-material for metal-free supercapacitors with graphene oxide separators and microwave exfoliated graphite oxide electrodes', *Electrochim Acta*, vol. 260, pp. 557–563, Jan. 2018, doi: 10.1016/J.ELECTACTA.2017.12.102.
- [33] A. Pourjavadi, M. Doroudian, A. Ahadpour, and B. Pourbadiiei, 'Preparation of flexible and free-standing graphene-based current collector via a new and facile self-assembly approach: Leading to a high performance porous graphene/polyaniline supercapacitor', *Energy*, vol. 152, pp. 178–189, Jun. 2018, doi: 10.1016/J.ENERGY.2018.03.138.
- [34] R. Raccichini, A. Varzi, S. Passerini, and B. Scrosati, 'The role of graphene for electrochemical energy storage', *Nature Materials 2014 14:3*, vol. 14, no. 3, pp. 271–279, Dec. 2014, doi: 10.1038/nmat4170.
- [35] E. L. Wolf, *SPRINGER BRIEFS IN MATERIALS: Applications of Graphene - An Overview*, vol. 1. Springer, 2014. doi: 10.1007/978-3-319-03946-6.
- [36] D. R. Dreyer, S. Park, C. W. Bielawski, and R. S. Ruoff, 'The chemistry of graphene oxide', *Chem Soc Rev*, vol. 39, no. 1, pp. 228–240, Dec. 2009, doi: 10.1039/B917103G.

- [37] J. W. Suk *et al.*, ‘Transfer of CVD-grown monolayer graphene onto arbitrary substrates’, *ACS Nano*, vol. 5, no. 9, pp. 6916–6924, Sep. 2011, doi: 10.1021/NN201207C/ASSET/IMAGES/LARGE/NN-2011-01207C_0001.JPEG.
- [38] Z. Sun, Y. Hu, [Z Sun, and H. Hu, ‘Ultrafast, Low-Cost, and Mass Production of High-Quality Graphene’, *Angewandte Chemie International Edition*, vol. 59, no. 24, pp. 9232–9234, Jun. 2020, doi: 10.1002/ANIE.202002256.
- [39] Z. Shi *et al.*, ‘Bubble-Mediated Mass Production of Graphene: A Review’, *Adv Funct Mater*, vol. 32, no. 42, p. 2203124, Oct. 2022, doi: 10.1002/ADFM.202203124.
- [40] K. R. Paton *et al.*, ‘Scalable production of large quantities of defect-free few-layer graphene by shear exfoliation in liquids’, *Nat Mater*, vol. 13, no. 6, pp. 624–630, 2014, doi: 10.1038/NMAT3944.
- [41] Y. Hernandez *et al.*, ‘High-yield production of graphene by liquid-phase exfoliation of graphite’, *Nature Nanotechnology 2008 3:9*, vol. 3, no. 9, pp. 563–568, Aug. 2008, doi: 10.1038/nnano.2008.215.
- [42] W. Du, X. Jiang, and L. Zhu, ‘From graphite to graphene : direct liquid-phase exfoliation of graphite to produce single- and few-layered pristine graphene’, *J Mater Chem A Mater*, vol. 1, no. 36, pp. 10592–10606, Aug. 2013, doi: 10.1039/C3TA12212C.
- [43] Y. Wei and Z. Sun, ‘Liquid-phase exfoliation of graphite for mass production of pristine few-layer graphene’, *Curr Opin Colloid Interface Sci*, vol. 20, no. 5–6, pp. 311–321, Oct. 2015, doi: 10.1016/J.COCIS.2015.10.010.
- [44] U. Khan, A. O’Neill, M. Lotya, S. De, and J. N. Coleman, ‘High-Concentration Solvent Exfoliation of Graphene’, *Small*, vol. 6, no. 7, pp. 864–871, Apr. 2010, doi: 10.1002/SMLL.200902066.
- [45] Z. Shen, J. Li, M. Yi, X. Zhang, and S. Ma, ‘Preparation of graphene by jet cavitation’, *Nanotechnology*, vol. 22, pp. 365306–365313, 2011, doi: 10.1088/0957-4484/22/36/365306.
- [46] K. Zhang *et al.*, ‘Production of few-layer graphene via enhanced high-pressure shear exfoliation in liquid for supercapacitor applications’, *ACS Appl Nano Mater*, vol. 1, no. 6, pp. 2877–2884, Jun. 2018, doi: 10.1021/ACSANM.8B00515/ASSET/IMAGES/LARGE/AN-2018-00515X_0007.JPEG.
- [47] R. Narayan and S. O. Kim, ‘Surfactant mediated liquid phase exfoliation of graphene’, *Nano Converg*, vol. 2, no. 1, Dec. 2015, doi: 10.1186/S40580-015-0050-X.
- [48] S. Biccai *et al.*, ‘Exfoliation of 2D materials by high shear mixing’, *2d Mater*, vol. 6, no. 1, p. 015008, Oct. 2018, doi: 10.1088/2053-1583/AAE7E3.
- [49] C. Teng *et al.*, ‘Ultrahigh Conductive Graphene Paper Based on Ball-Milling Exfoliated Graphene’, *Adv Funct Mater*, vol. 27, no. 20, p. 1700240, May 2017, doi: 10.1002/ADFM.201700240.

- [50] W. Zhao, M. Fang, F. Wu, H. Wu, L. Wang, and G. Chen, 'Preparation of graphene by exfoliation of graphite using wet ball milling', *J Mater Chem*, vol. 20, no. 28, pp. 5817–5819, Jul. 2010, doi: 10.1039/C0JM01354D.
- [51] A. S. Al-Sherbini, M. Bakr, I. Ghoneim, and M. Saad, 'Exfoliation of graphene sheets via high energy wet milling of graphite in 2-ethylhexanol and kerosene', *J Adv Res*, vol. 8, no. 3, pp. 209–215, May 2017, doi: 10.1016/J.JARE.2017.01.004.
- [52] Y. Xu, H. Cao, Y. Xue, B. Li, and W. Cai, 'Liquid-Phase Exfoliation of Graphene: An Overview on Exfoliation Media, Techniques, and Challenges', *Nanomaterials 2018, Vol. 8, Page 942*, vol. 8, no. 11, p. 942, Nov. 2018, doi: 10.3390/NANO8110942.
- [53] X. Chen, J. F. Dobson, and C. L. Raston, 'Vortex fluidic exfoliation of graphite and boron nitride', *Chemical Communications*, vol. 48, no. 31, pp. 3703–3705, Mar. 2012, doi: 10.1039/C2CC17611D.
- [54] M. Alamer, A. R. Lim, and Y. L. Joo, 'Continuous Synthesis of Structurally Uniform Graphene Oxide Materials in a Model Taylor-Couette Flow Reactor', *Ind Eng Chem Res*, vol. 58, no. 3, pp. 1167–1176, Jan. 2019, doi: 10.1021/ACS.IECR.8B04428/ASSET/IMAGES/LARGE/IE-2018-04428F_0009.JPEG.
- [55] S. Lund *et al.*, 'Fast high-shear exfoliation of natural flake graphite with temperature control and high yield', *Carbon N Y*, vol. 174, pp. 123–131, Apr. 2021, doi: 10.1016/J.CARBON.2020.11.094.
- [56] S. Lund *et al.*, 'Shear exfoliated few-layer graphene and cellulose nanocrystal composite as biocompatible anode with efficient charge transfer', *Carbon Trends*, vol. 9, p. 100210, Oct. 2022, doi: 10.1016/J.CARTRE.2022.100210.
- [57] E. Varrla *et al.*, 'Turbulence-assisted shear exfoliation of graphene using household detergent and a kitchen blender', *Nanoscale*, vol. 6, no. 20, pp. 11810–11819, Sep. 2014, doi: 10.1039/C4NR03560G.
- [58] M. Yi and Z. Shen, 'Kitchen blender for producing high-quality few-layer graphene', *Carbon N Y*, vol. 78, pp. 622–626, Nov. 2014, doi: 10.1016/J.CARBON.2014.07.035.
- [59] M. Yi and Z. Shen, 'Fluid dynamics: an emerging route for the scalable production of graphene in the last five years', *RSC Adv*, vol. 6, no. 76, pp. 72525–72536, Aug. 2016, doi: 10.1039/C6RA15269D.
- [60] X. Chen, R. Paul, and L. Dai, 'Carbon-based supercapacitors for efficient energy storage', *Natl Sci Rev*, vol. 4, no. 3, pp. 453–489, May 2017, doi: 10.1093/NSR/NWX009.
- [61] L. Jiang *et al.*, 'Activated carbon/graphene composites with high-rate performance as electrode materials for electrochemical capacitors', *Journal of Solid State Electrochemistry*, vol. 17, no. 11, pp. 2949–2958, Nov. 2013, doi: 10.1007/S10008-013-2217-X/FIGURES/7.
- [62] D. J. Hsu, Y. W. Chi, K. P. Huang, and C. C. Hu, 'Electrochemical activation of vertically grown graphene nanowalls synthesized by plasma-enhanced chemical vapor

- deposition for high-voltage supercapacitors', *Electrochim Acta*, vol. 300, pp. 324–332, Mar. 2019, doi: 10.1016/J.ELECTACTA.2019.01.134.
- [63] S. Suresh Balaji, M. Sandhiya, and M. Sathish, 'Enhanced electrochemical performance of supercritical fluid aided P-doped graphene nanoflakes by I³–/I[–] redox couple', *J Energy Storage*, vol. 33, p. 102085, Jan. 2021, doi: 10.1016/J.EST.2020.102085.
- [64] M. Wang and Y. Ma, 'Nitrogen-doped graphene forests as electrodes for high-performance wearable supercapacitors', *Electrochim Acta*, vol. 250, pp. 320–326, Oct. 2017, doi: 10.1016/J.ELECTACTA.2017.08.073.
- [65] K. Xia *et al.*, 'Facile and controllable synthesis of N/P co-doped graphene for high-performance supercapacitors', *J Power Sources*, vol. 365, pp. 380–388, Oct. 2017, doi: 10.1016/J.JPOWSOUR.2017.09.008.
- [66] S. S. Balaji, M. Karnan, P. Anandhaganesh, S. M. Tauquir, and M. Sathish, 'Performance evaluation of B-doped graphene prepared via two different methods in symmetric supercapacitor using various electrolytes', *Appl Surf Sci*, vol. 491, pp. 560–569, Oct. 2019, doi: 10.1016/J.APSUSC.2019.06.151.
- [67] Y. Shabangoli *et al.*, 'Thionine Functionalized 3D Graphene Aerogel: Combining Simplicity and Efficiency in Fabrication of a Metal-Free Redox Supercapacitor', *Adv Energy Mater*, vol. 8, no. 34, p. 1802869, Dec. 2018, doi: 10.1002/AENM.201802869.
- [68] D. Trache, A. F. Tarchoun, M. Derradji, O. Mehelli, M. H. Hussin, and W. Bessa, 'Cellulose Fibers and Nanocrystals: Preparation, Characterization, and Surface Modification', *Functionalized Nanomaterials I*, pp. 171–190, Aug. 2020, doi: 10.1201/9781351021623-11.
- [69] Y. Habibi, L. A. Lucia, and O. J. Rojas, 'Cellulose nanocrystals: Chemistry, self-assembly, and applications', *Chem Rev*, vol. 110, no. 6, pp. 3479–3500, Jun. 2010, doi: 10.1021/CR900339W/ASSET/IMAGES/MEDIUM/CR-2009-00339W_0022.GIF.
- [70] D. Trache *et al.*, 'Nanocellulose: From Fundamentals to Advanced Applications', *Front Chem*, vol. 8, p. 392, May 2020, doi: 10.3389/FCHEM.2020.00392/BIBTEX.
- [71] T. Xu *et al.*, 'Advanced Nanocellulose-Based Composites for Flexible Functional Energy Storage Devices', *Advanced Materials*, vol. 33, no. 48, p. 2101368, Dec. 2021, doi: 10.1002/ADMA.202101368.
- [72] Z. Wang and L. Nyholm, 'Energy Storage Applications', in *Emerging Nanotechnologies in Nanocellulose*, L. Hu, F. Jiang, and C. Chen, Eds., Cham: Springer International Publishing, 2023, pp. 237–265. doi: 10.1007/978-3-031-14043-3_8.
- [73] S. Dong, A. A. Hirani, K. R. Colacino, Y. Woo Lee, and M. Roman, 'CYTOTOXICITY AND CELLULAR UPTAKE OF CELLULOSE NANOCRYSTALS', *Nano Life*, vol. 2, no. 3, p. 1241006, 2012, doi: 10.1142/S1793984412410061.
- [74] H. Kargarzadeh *et al.*, 'Advances in cellulose nanomaterials', *Cellulose 2018 25:4*, vol. 25, no. 4, pp. 2151–2189, Feb. 2018, doi: 10.1007/S10570-018-1723-5.
- [75] A. Dufresne, 'Cellulose nanomaterial reinforced polymer nanocomposites', *Curr Opin Colloid Interface Sci*, vol. 29, pp. 1–8, May 2017, doi: 10.1016/J.COCIS.2017.01.004.

- [76] S. Naz, J. S. Ali, and M. Zia, ‘Nanocellulose isolation characterization and applications: a journey from non-remedial to biomedical claims’, *Biodes Manuf*, vol. 2, no. 3, pp. 187–212, Sep. 2019, doi: 10.1007/S42242-019-00049-4/TABLES/5.
- [77] T. Abitbol, D. Kam, Y. Levi-Kalisman, D. G. Gray, and O. Shoseyov, ‘Surface Charge Influence on the Phase Separation and Viscosity of Cellulose Nanocrystals’, *Langmuir*, vol. 34, no. 13, pp. 3925–3933, Apr. 2018, doi: 10.1021/ACS.LANGMUIR.7B04127/ASSET/IMAGES/MEDIUM/LA-2017-041276_M002.GIF.
- [78] X. Wu, V. L. Chabot, B. K. Kim, A. Yu, R. M. Berry, and K. C. Tam, ‘Cost-effective and Scalable Chemical Synthesis of Conductive Cellulose Nanocrystals for High-performance Supercapacitors’, *Electrochim Acta*, vol. 138, pp. 139–147, Aug. 2014, doi: 10.1016/J.ELECTACTA.2014.06.089.
- [79] Y. Chen, J. Zhu, H. Y. Yu, and Y. Li, ‘Fabricating robust soft-hard network of self-healable polyvinyl alcohol composite films with functionalized cellulose nanocrystals’, *Compos Sci Technol*, vol. 194, p. 108165, Jul. 2020, doi: 10.1016/J.COMPSCITECH.2020.108165.
- [80] Z. J. Zhang and X. Y. Chen, ‘Carbon nanofibers derived from bacterial cellulose: Surface modification by polydopamine and the use of ferrous ion as electrolyte additive for collaboratively increasing the supercapacitor performance’, *Appl Surf Sci*, vol. 519, p. 146252, Jul. 2020, doi: 10.1016/J.APSUSC.2020.146252.
- [81] N. Sheng *et al.*, ‘Polypyrrole@TEMPO-oxidized bacterial cellulose/reduced graphene oxide macrofibers for flexible all-solid-state supercapacitors’, *Chemical Engineering Journal*, vol. 368, pp. 1022–1032, Jul. 2019, doi: 10.1016/J.CEJ.2019.02.173.
- [82] C. Chen and L. Hu, ‘Nanocellulose toward Advanced Energy Storage Devices: Structure and Electrochemistry’, *Acc Chem Res*, vol. 51, no. 12, pp. 3154–3165, Dec. 2018, doi: 10.1021/ACS.ACCOUNTS.8B00391/ASSET/IMAGES/LARGE/AR-2018-00391J_0009.JPEG.
- [83] R. Pan *et al.*, ‘Mesoporous Cladophora cellulose separators for lithium-ion batteries’, *J Power Sources*, vol. 321, pp. 185–192, Jul. 2016, doi: 10.1016/J.JPOWSOUR.2016.04.115.
- [84] N. A. A. Sezali, H. L. Ong, N. Jullok, A. R. Villagracia, and R. A. Doong, ‘A Review on Nanocellulose and Its Application in Supercapacitors’, *Macromol Mater Eng*, vol. 306, no. 12, Dec. 2021, doi: 10.1002/MAME.202100556.
- [85] L. Nyholm, G. Nyström, A. Mihranyan, and M. Strømme, ‘Toward flexible polymer and paper-based energy storage devices’, *Adv Mater*, vol. 23, no. 33, pp. 3751–3769, Sep. 2011, doi: 10.1002/ADMA.201004134.
- [86] D. Harvey, *Modern Analytical Chemistry*, 1st ed., vol. 1. McGraw-Hill, 2000.
- [87] D. C. Harris, *Quantitative Chemical Analysis 8th Ed.*, W. H. Freeman and Company, New York, vol. 58, no. 22. 2010.

- [88] D. A. Skoog, D. M. West, F. J. Holler, and S. R. Crouch, *Fundamentals of analytical chemistry, 9th edition*. 2014.
- [89] R. S. Das and Y. K. Agrawal, ‘Raman spectroscopy: Recent advancements, techniques and applications’, *Vib Spectrosc*, vol. 57, no. 2, pp. 163–176, Nov. 2011, doi: 10.1016/J.VIBSPEC.2011.08.003.
- [90] C. A. Bishop, ‘Process Diagnostics and Coating Characteristics’, *Vacuum Deposition Onto Webs, Films and Foils*, pp. 85–128, Jan. 2015, doi: 10.1016/B978-0-323-29644-1.00005-0.
- [91] F. M. Smits, ‘Measurement of Sheet Resistivities with the Four-Point Probe’, *Bell System Technical Journal*, vol. 37, no. 3, pp. 711–718, May 1958, doi: 10.1002/J.1538-7305.1958.TB03883.X.
- [92] D. Boonpakdee, C. F. Guajardo Yévenes, W. Surareunghai, and C. La-O-Vorakiat, ‘Exploring non-linearities of carbon-based microsupercapacitors from an equivalent circuit perspective’, *J Mater Chem A Mater*, vol. 6, no. 16, pp. 7162–7167, Apr. 2018, doi: 10.1039/C8TA01995A.
- [93] T. Schoetz, L. W. Gordon, S. Ivanov, A. Bund, D. Mandler, and R. J. Messinger, ‘Disentangling faradaic, pseudocapacitive, and capacitive charge storage: A tutorial for the characterization of batteries, supercapacitors, and hybrid systems’, *Electrochim Acta*, vol. 412, p. 140072, Apr. 2022, doi: 10.1016/J.ELECTACTA.2022.140072.
- [94] N. Bonanos *et al.*, ‘Applications of Impedance Spectroscopy’, *Impedance Spectroscopy: Theory, Experiment, and Applications, Second Edition*, pp. 205–537, Jan. 2005, doi: 10.1002/0471716243.CH4.
- [95] ‘Basics of EIS: Electrochemical Research-Impedance Gamry Instruments’. <https://www.gamry.com/application-notes/EIS/basics-of-electrochemical-impedance-spectroscopy/> (accessed Jun. 28, 2023).
- [96] M. D. Stoller and R. S. Ruoff, ‘Best practice methods for determining an electrode material’s performance for ultracapacitors’, *Energy Environ Sci*, vol. 3, no. 9, pp. 1294–1301, Aug. 2010, doi: 10.1039/C0EE00074D.
- [97] ‘Testing Electrochemical Capacitors: Cyclic Charge-Discharge-Stacks Gamry Instruments’. <https://www.gamry.com/application-notes/battery-research/electrochemical-capacitors-cyclic-charge-discharge-and-stacks/> (accessed May 03, 2023).
- [98] A. Laheäär, P. Przygocki, Q. Abbas, and F. Béguin, ‘Appropriate methods for evaluating the efficiency and capacitive behavior of different types of supercapacitors’, *Electrochem commun*, vol. 60, pp. 21–25, Nov. 2015, doi: 10.1016/J.ELECOM.2015.07.022.
- [99] M. Lotya, P. J. King, U. Khan, S. De, and J. N. Coleman, ‘High-concentration, surfactant-stabilized graphene dispersions’, *ACS Nano*, vol. 4, no. 6, pp. 3155–3162, Jun. 2010, doi: 10.1021/NN1005304/SUPPL_FILE/NN1005304_SI_001.PDF.

- [100] J. W. T. Seo, A. A. Green, A. L. Antaris, and M. C. Hersam, ‘High-concentration aqueous dispersions of graphene using nonionic, biocompatible block copolymers’, *Journal of Physical Chemistry Letters*, vol. 2, no. 9, pp. 1004–1008, May 2011, doi: 10.1021/JZ2003556/SUPPL_FILE/JZ2003556_SI_001.PDF.
- [101] R. R. Nair *et al.*, ‘Fine structure constant defines visual transparency of graphene’, *Science (1979)*, vol. 320, no. 5881, p. 1308, Jun. 2008, doi: 10.1126/SCIENCE.1156965/SUPPL_FILE/NAIR.SOM.PDF.
- [102] F. Rana, ‘Graphene Terahertz Plasmon Oscillators’, *IEEE Trans Nanotechnol*, vol. 7, no. 1, pp. 91–99, Oct. 2007, doi: 10.1109/TNANO.2007.910334.
- [103] J. Palosaari, R. M. Latonen, J. H. Smått, R. Blomqvist, and O. Eklund, ‘High-quality flake graphite occurrences in a high-grade metamorphic region in Sortland, Vesterålen, northern Norway’, *Norwegian Journal of Geology*, vol. 96, no. 1, pp. 19–26, 2016, doi: 10.17850/NJG96-1-03.
- [104] A. C. Ferrari, ‘Raman spectroscopy of graphene and graphite: Disorder, electron–phonon coupling, doping and nonadiabatic effects’, *Solid State Commun*, vol. 143, no. 1–2, pp. 47–57, Jul. 2007, doi: 10.1016/J.SSC.2007.03.052.
- [105] M. Wall, ‘Raman Spectroscopy Optimizes Graphene Characterization’, *AM&P Technical Articles*, vol. 170, no. 4, pp. 35–38, Apr. 2012, doi: 10.31399/ASM.AMP.2012-04.P035.
- [106] A. Eckmann *et al.*, ‘Probing the nature of defects in graphene by Raman spectroscopy’, *Nano Lett*, vol. 12, no. 8, pp. 3925–3930, Aug. 2012, doi: 10.1021/NL300901A/SUPPL_FILE/NL300901A_SI_001.PDF.
- [107] S. Roscher, R. Hoffmann, and O. Ambacher, ‘Determination of the graphene–graphite ratio of graphene powder by Raman 2D band symmetry analysis’, *Analytical Methods*, vol. 11, no. 9, pp. 1224–1228, Feb. 2019, doi: 10.1039/C8AY02619J.
- [108] D. Graf *et al.*, ‘Spatially resolved raman spectroscopy of single- and few-layer graphene’, *Nano Lett*, vol. 7, no. 2, pp. 238–242, Feb. 2007, doi: 10.1021/NL061702A/ASSET/IMAGES/LARGE/NL061702AF00006.JPEG.
- [109] D. Yoon, H. Moon, H. Cheong, J. S. Choi, J. A. Choi, and B. H. Park, ‘Variations in the Raman Spectrum as a Function of the Number of Graphene Layers’, *Journal of the Korean Physical Society*, vol. 55, no. 3, pp. 1299–1303, Sep. 2009, doi: 10.3938/JKPS.55.1299.
- [110] N. Pandi, S. H. Sonawane, and K. Anand Kishore, ‘Synthesis of cellulose nanocrystals (CNCs) from cotton using ultrasound-assisted acid hydrolysis’, *Ultrason Sonochem*, vol. 70, p. 105353, Jan. 2021, doi: 10.1016/J.ULTSONCH.2020.105353.
- [111] H. Kargarzadeh, I. Ahmad, I. Abdullah, A. Dufresne, S. Y. Zainudin, and R. M. Sheltami, ‘Effects of hydrolysis conditions on the morphology, crystallinity, and thermal stability of cellulose nanocrystals extracted from kenaf bast fibers’, *Cellulose*, vol. 19, no. 3, pp. 855–866, Jun. 2012, doi: 10.1007/S10570-012-9684-6/FIGURES/5.

- [112] G. F. Hawes, S. Rehman, Y. Rangom, and M. A. Pope, ‘Advanced manufacturing approaches for electrochemical energy storage devices’, *International Materials Reviews*, 2022, doi: 10.1080/09506608.2022.2086388/SUPPL_FILE/YIMR_A_2086388_SM7326.DOCX.
- [113] M. Jana *et al.*, ‘Non-covalent functionalization of reduced graphene oxide using sulfanilic acid azocromotrop and its application as supercapacitor electrode material’, *J. Name*, vol. 00, pp. 1–3, 2013, doi: 10.1039/x0xx00000x.
- [114] M. A. Garakani *et al.*, ‘Scalable spray-coated graphene-based electrodes for high-power electrochemical double-layer capacitors operating over a wide range of temperature’, *Energy Storage Mater*, vol. 34, pp. 1–11, Jan. 2021, doi: 10.1016/J.ENSM.2020.08.036.
- [115] B.-A. Mei, O. Munteshari, J. Lau, B. Dunn, and L. Pilon, ‘Physical Interpretations of Nyquist Plots for EDLC Electrodes and Devices’, *J. Phys. Chem. C*, vol. 122, p. 206, 2018, doi: 10.1021/acs.jpcc.7b10582.
- [116] B. Fang and L. Binder, ‘A novel carbon electrode material for highly improved EDLC performance’, *Journal of Physical Chemistry B*, vol. 110, no. 15, pp. 7877–7882, Apr. 2006, doi: 10.1021/JP060110D/ASSET/IMAGES/LARGE/JP060110DF00006.JPEG.
- [117] L. Chang and Y. H. Hu, ‘Breakthroughs in Designing Commercial-Level Mass-Loading Graphene Electrodes for Electrochemical Double-Layer Capacitors’, *Matter*, vol. 1, no. 3, pp. 596–620, Sep. 2019, doi: 10.1016/J.MATT.2019.06.016.
- [118] Q. Wu, Y. Sun, H. Bai, and G. Shi, ‘High-performance supercapacitor electrodes based on graphene hydrogels modified with 2-aminoanthraquinone moieties’, *Physical Chemistry Chemical Physics*, vol. 13, no. 23, pp. 11193–11198, May 2011, doi: 10.1039/C1CP20980A.
- [119] K. B. Li *et al.*, ‘Studies on the equivalent serial resistance of carbon supercapacitor’, *Electrochim Acta*, vol. 174, pp. 596–600, Aug. 2015, doi: 10.1016/J.ELECTACTA.2015.06.008.
- [120] G. J. Brug, A. L. G. van den Eeden, M. Sluyters-Rehbach, and J. H. Sluyters, ‘The analysis of electrode impedances complicated by the presence of a constant phase element’, *J Electroanal Chem Interfacial Electrochem*, vol. 176, no. 1–2, pp. 275–295, Sep. 1984, doi: 10.1016/S0022-0728(84)80324-1.
- [121] T. Pajkossy, ‘Impedance of rough capacitive electrodes’, *Journal of Electroanalytical Chemistry*, vol. 364, no. 1–2, pp. 111–125, Jan. 1994, doi: 10.1016/0022-0728(93)02949-I.
- [122] M. Beidaghi and Y. Gogotsi, ‘Capacitive energy storage in micro-scale devices: recent advances in design and fabrication of micro-supercapacitors’, *Energy Environ Sci*, vol. 7, no. 3, pp. 867–884, Feb. 2014, doi: 10.1039/C3EE43526A.
- [123] J. Wang *et al.*, ‘Recent Progress in Micro-Supercapacitor Design, Integration, and Functionalization’, *Small Methods*, vol. 3, no. 8, p. 1800367, Aug. 2019, doi: 10.1002/SMTD.201800367.

APPENDIX

A. G-CNC Dispersion Preparation

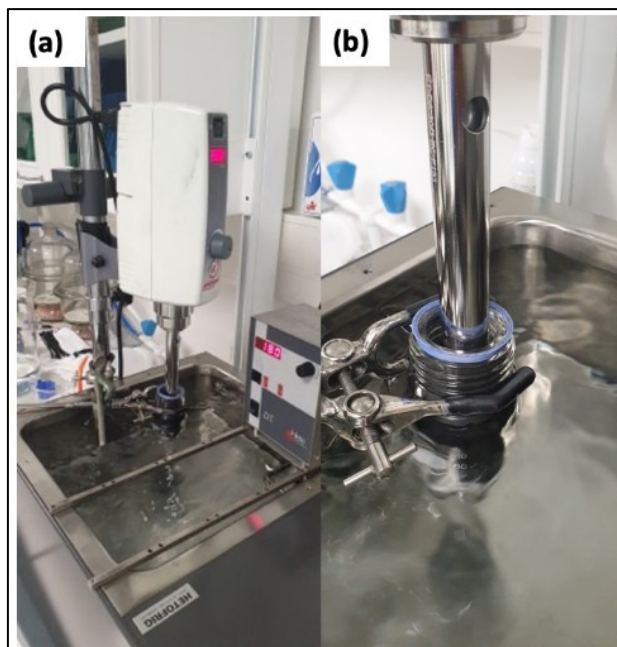


Figure A - 1. Experimental set-up (a) for the high-shear, liquid-phase exfoliation of graphene with CNC suspension. A close-up image of the set-up is shown in (b).

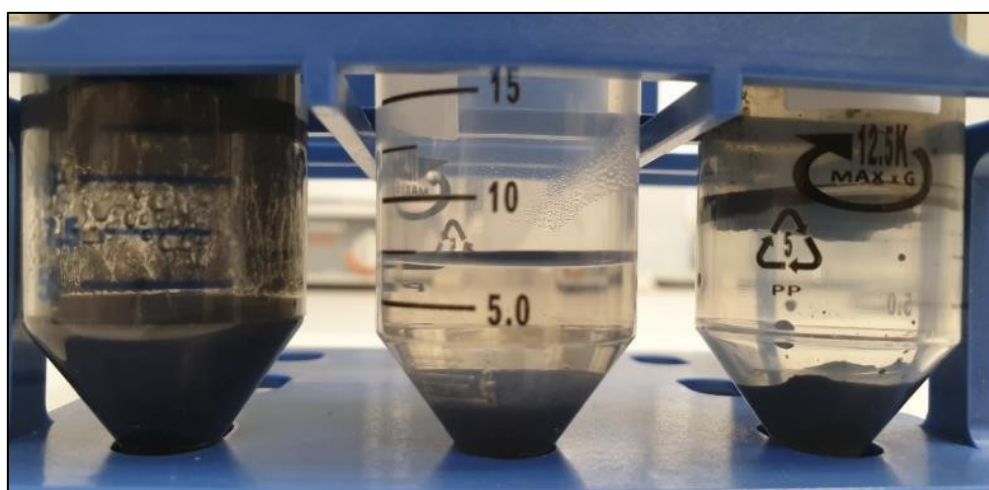


Figure A - 2. Visual comparisons of different batches of the G-CNC dispersion (left - Batch 16, middle - Batch 20, right - Batch 31). Only Batch 20 in this image has a different graphite-to-CNC mass ratio (20:1 vs 15:1), showing the instability of the dispersion.

B. G-CNC Electrode Preparation

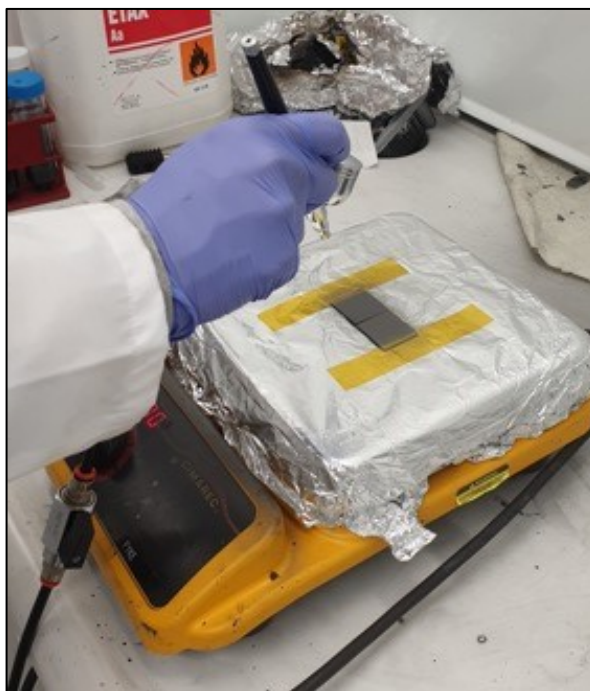


Figure A - 3. Experimental set-up for the manual spray-coating of the G-CNC dispersions on graphite foil substrate.

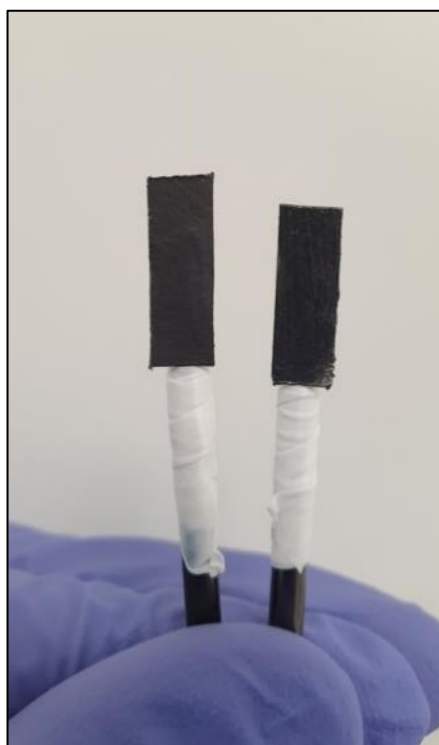


Figure A - 4. G-CNC Batch 19 electrodes used for the three-electrode CV experiments. Electrode area is 0.75 cm^2 .

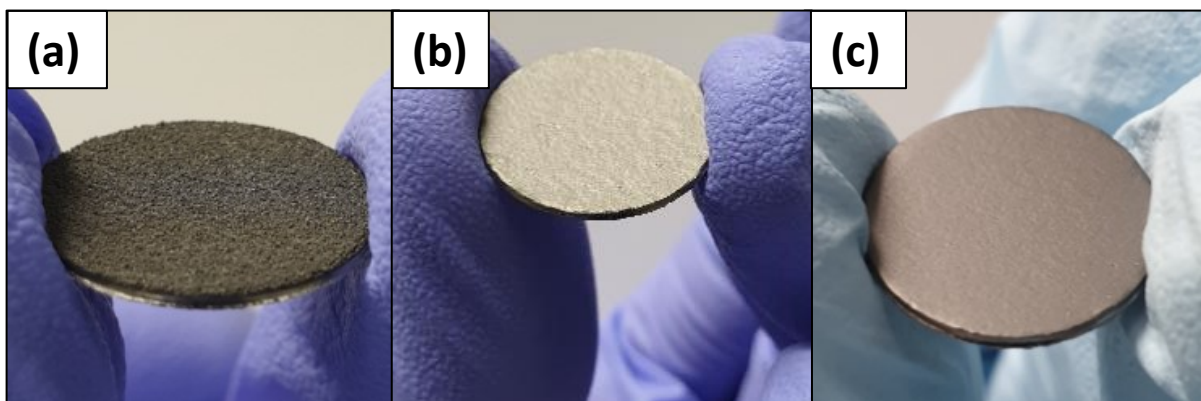


Figure A - 5. Visual comparison of the G-CNC electrode surfaces for Batch 16 (a), Batch 19 (b), and Batch 31(c). Batch 16 electrodes tend to have a rougher surface due to the presence of partially exfoliated graphite, whereas Batches 19 and 31 had a smoother surface with zero (minimal) traces of the partially exfoliated graphite.

C. Physicochemical Characterisations of G-CNC Composite

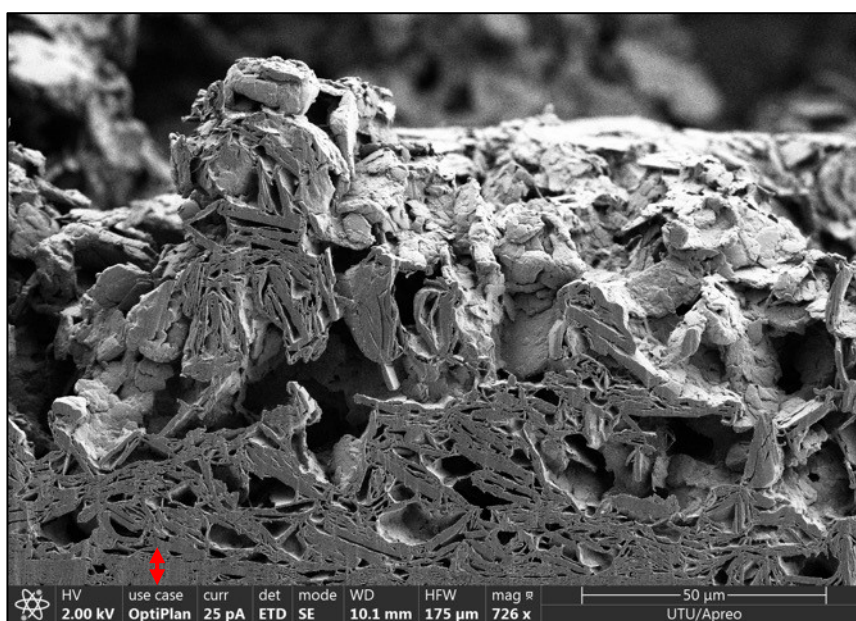


Figure A - 6. A cross-sectional image of a G-CNC Batch 16 electrode with a film thickness estimate of 80 μm. It is seen from the image that the agglomeration of the partially exfoliated graphite closely resembles the morphology of the graphite foil substrate (substrate layer thickness estimated by the red arrow).

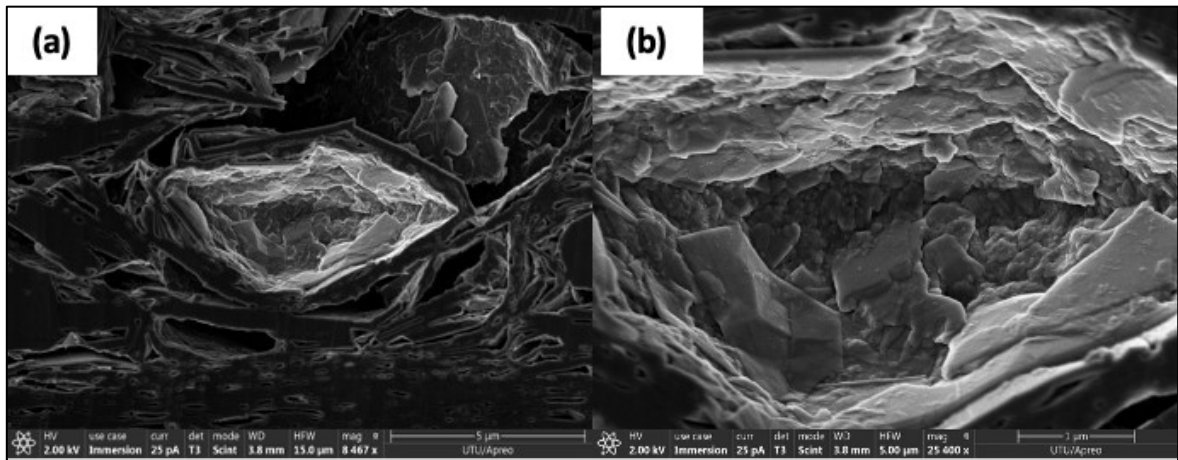


Figure A - 7. A contrast image of exfoliated graphene sheets (in lighter contrast) intercalated in the graphite foil substrate (a). A close-up image of the graphene sheets are shown in (b).

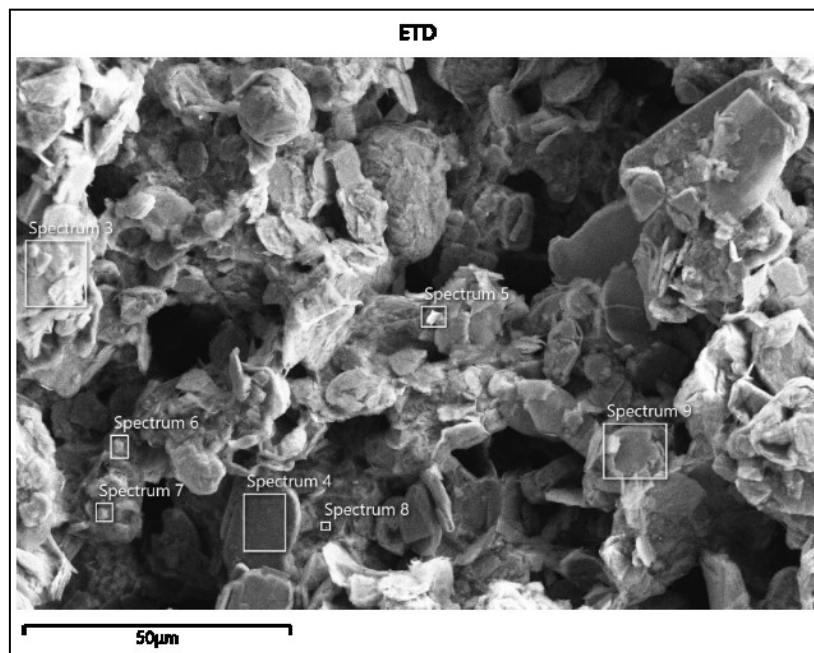


Figure A - 8. Surface SEM image of G-CNC Batch 16 electrode used for representative EDX analysis. EDX Spectra were taken from different points as shown by the boxed areas in the figure (Spectra in Figure A - 9).

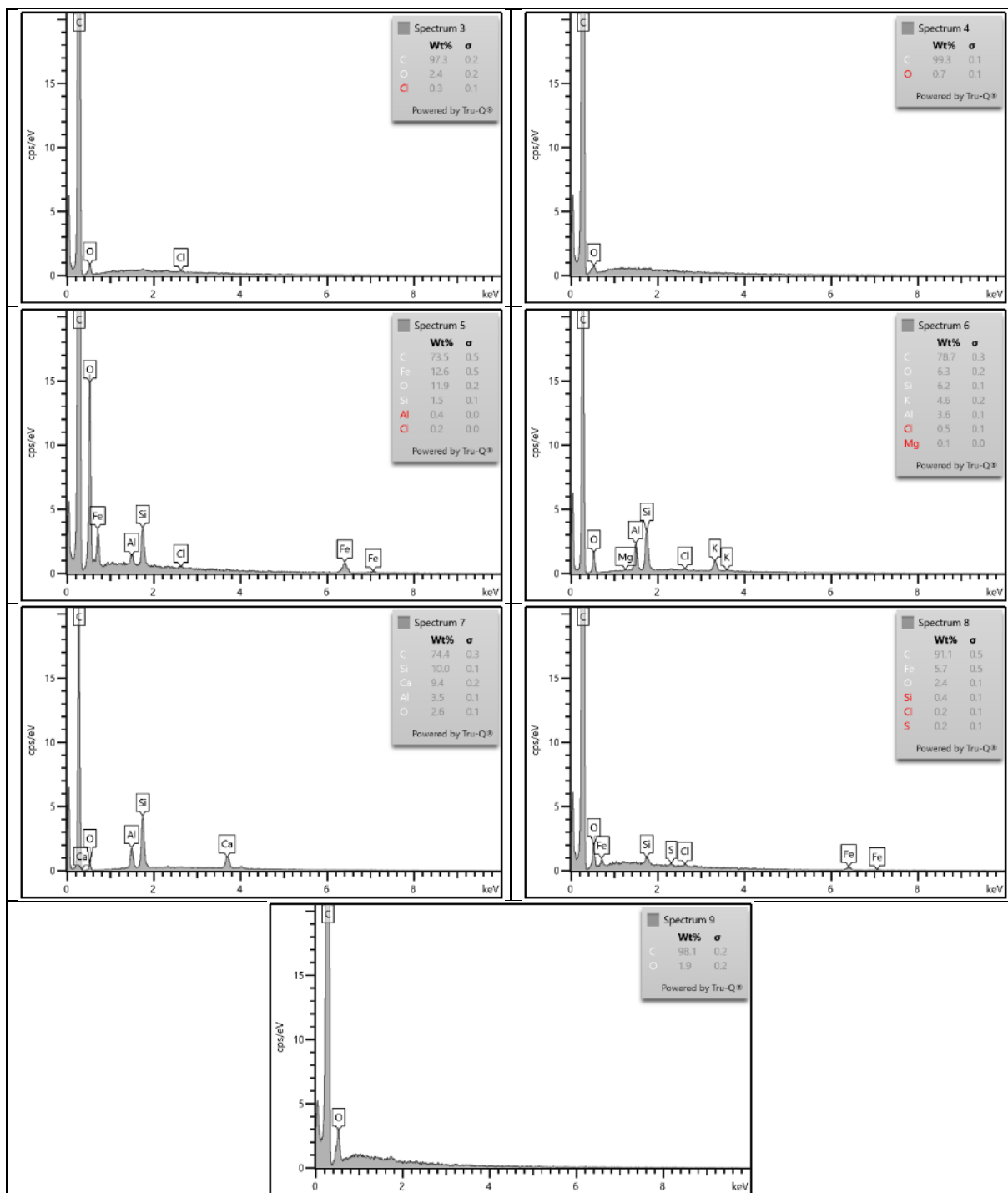


Figure A - 9. EDX Spectra collected at different points of the G-CNC Batch 16 electrode surface (Image in Figure A - 8).

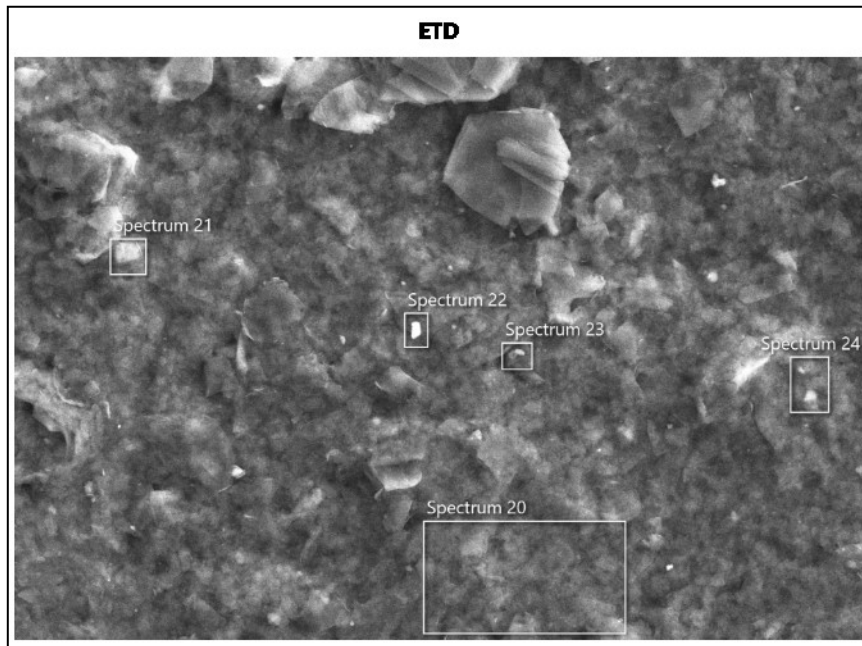


Figure A - 10. Surface SEM image of G-CNC Batch 19 electrode used for representative EDX analysis. EDX Spectra were taken from different points as shown by the boxed areas in the figure (Spectra in Figures A – 11 and A – 12).

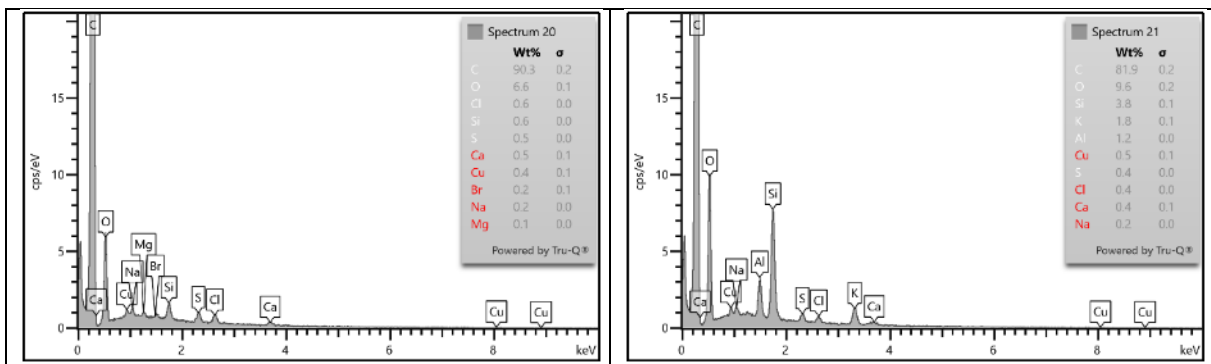


Figure A - 11. EDX Spectra collected at different points of the G-CNC Batch 19 electrode surface (Image in Figure A - 10). The first two spectra are only shown here; the remaining are presented in Figure A – 12.

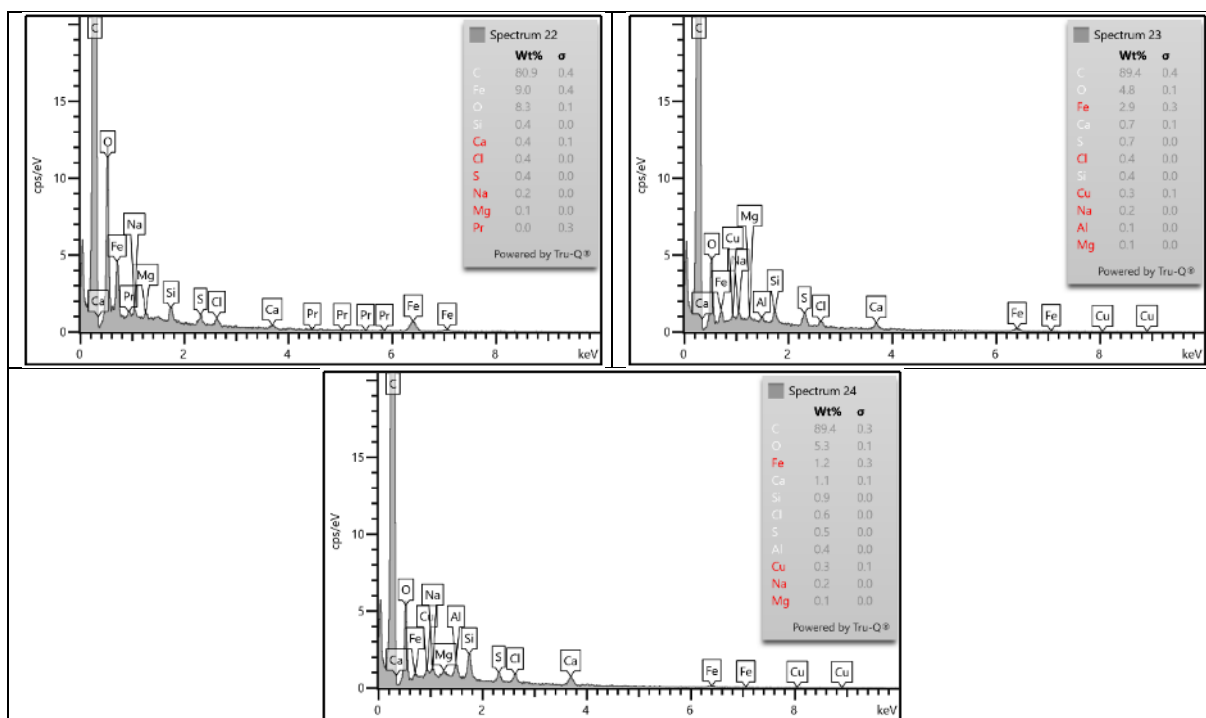


Figure A - 12. EDX Spectra collected at different points of the G-CNC Batch 19 electrode surface (Image in Figure A - 10). The remaining three spectra are only shown here; the first two spectra are presented in Figure A – 11.

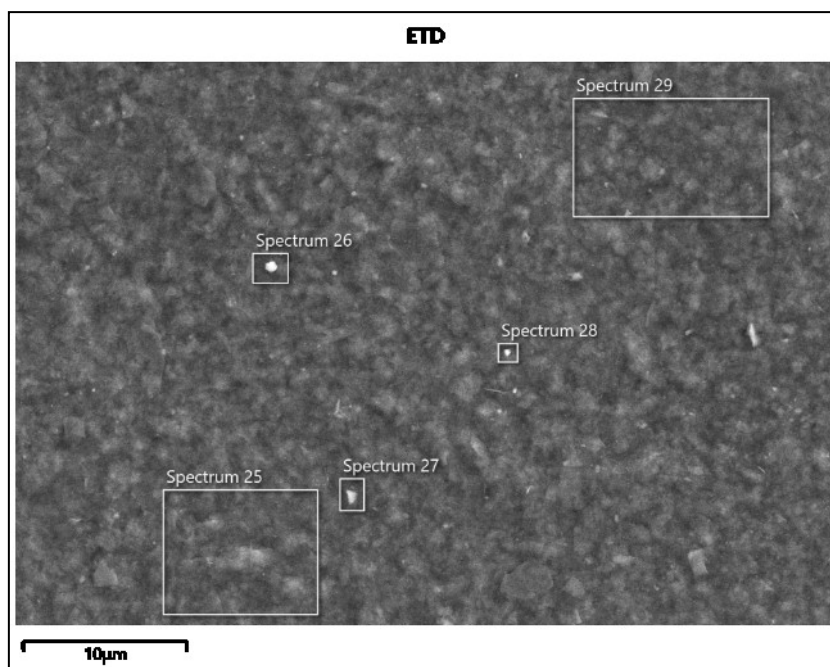


Figure A - 13. Surface SEM image of G-CNC Batch 31 electrode used for representative EDX analysis. EDX Spectra were taken from different points as shown by the boxed areas in the figure (Spectra in Figure A – 14).

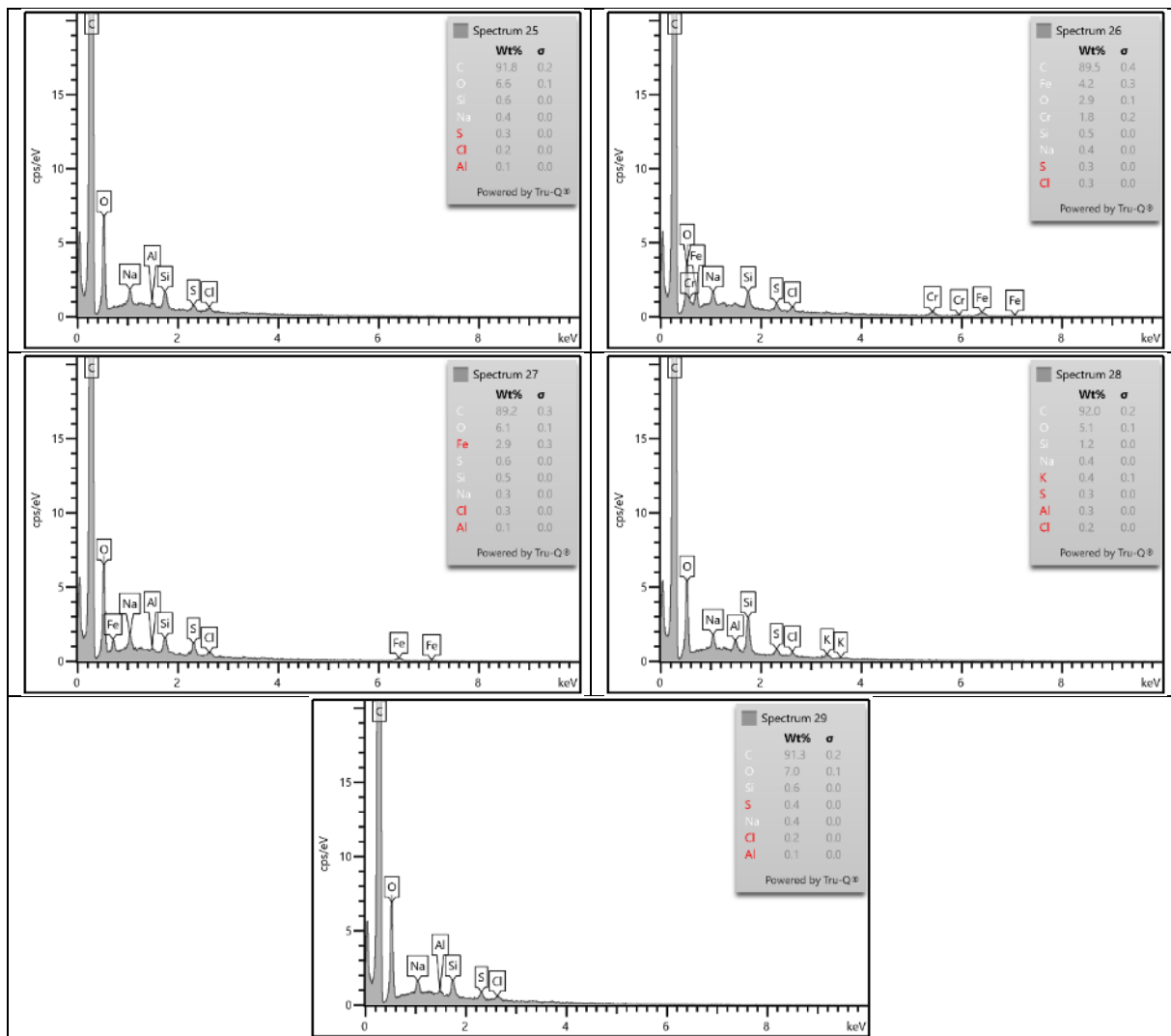


Figure A - 14. EDX Spectra collected at different points of the G-CNC Batch 31 electrode surface (Image in Figure A - 13).

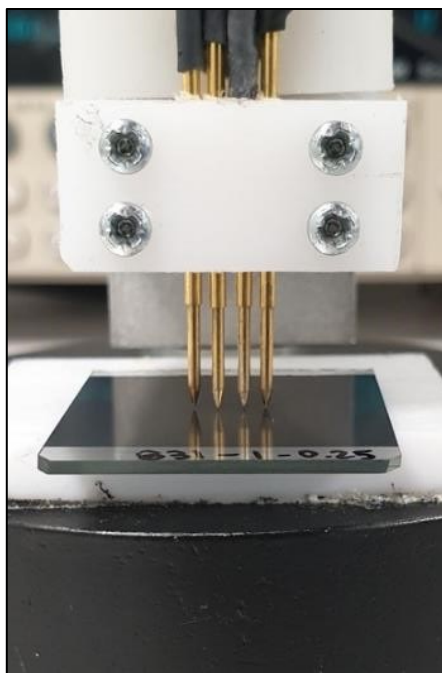


Figure A - 15. A representative image of the four-point probe measurement of electrical conductivity for the G-CNC films spray-coated on glass substrate. Measured film in this figure was from G-CNC Batch 31.

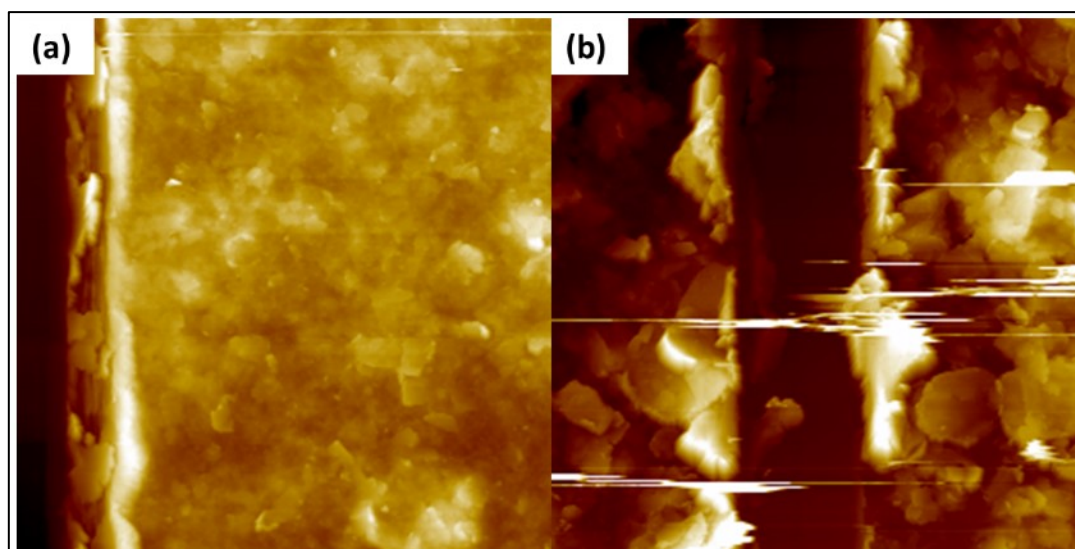


Figure A - 16. Sample AFM images taken for G-CNC Batches 11 (a) and 16 (b). The sharp, white lines in the figure indicate the surface non-uniformities in the G-CNC. They correspond to film thicknesses $>5.0 \mu\text{m}$.

D. Electrochemical Characterisations of G-CNC Electrodes

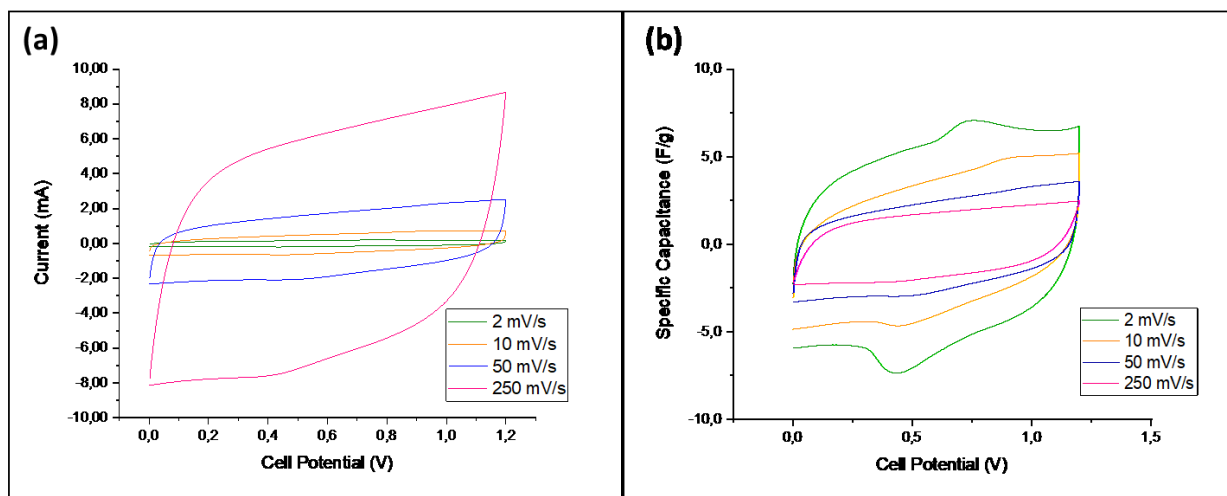


Figure A - 17. Two-electrode CV curves for G-CNC electrodes at varying scan rates using G-CNC Batch 16. CV profiles are expressed as plot of current vs. cell potential (a) and C_s vs cell potential (b). Curves were expressed as average ($n = 2$).

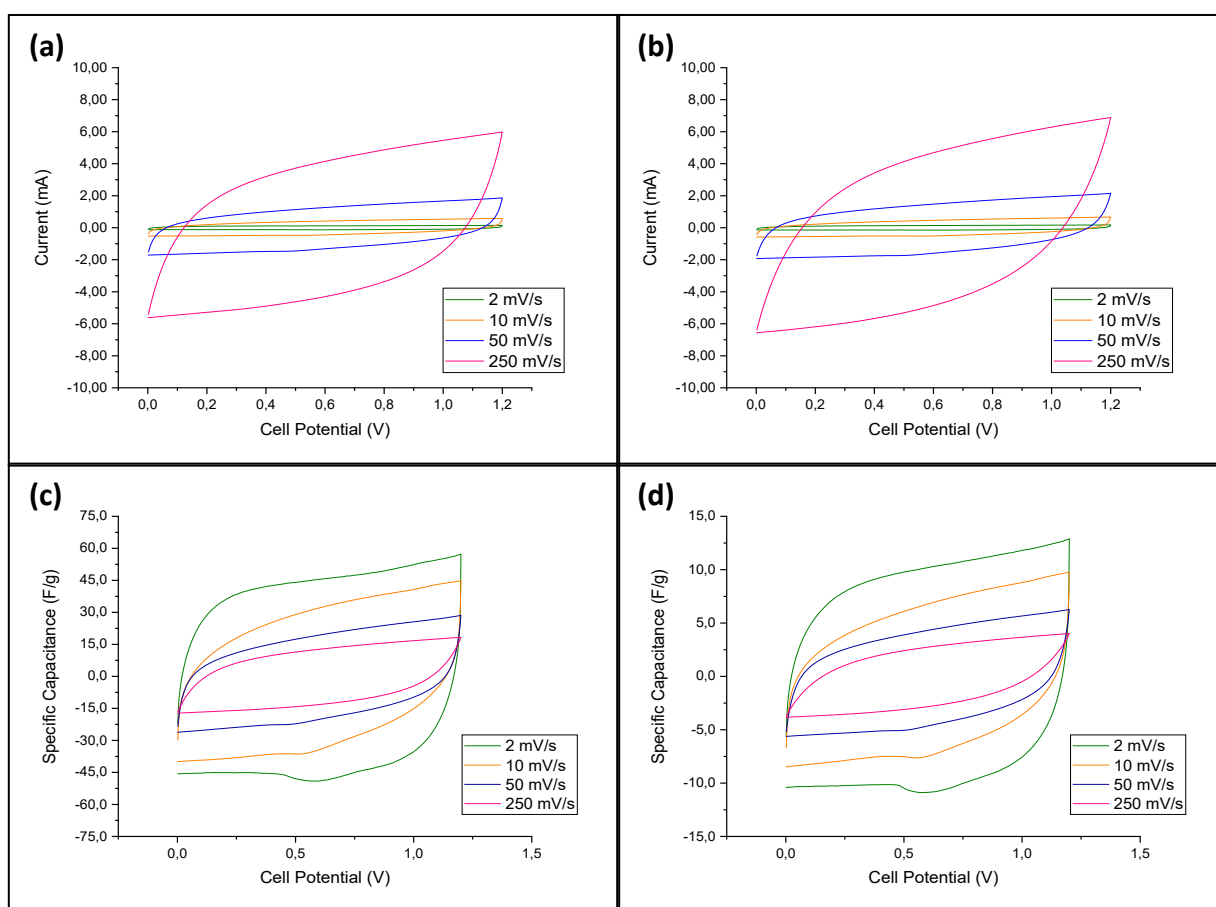


Figure A - 18. Two-electrode CV curves for G-CNC electrodes at varying scan rates using G-CNC Batch 31. CV profiles are expressed as plot of current vs. cell potential (a, b) and C_s vs cell potential (c, d). The two replicates tested were not averaged due to different G-CNC average mass loadings (a,c – 2.7 mg, b,d – 13.7 mg).

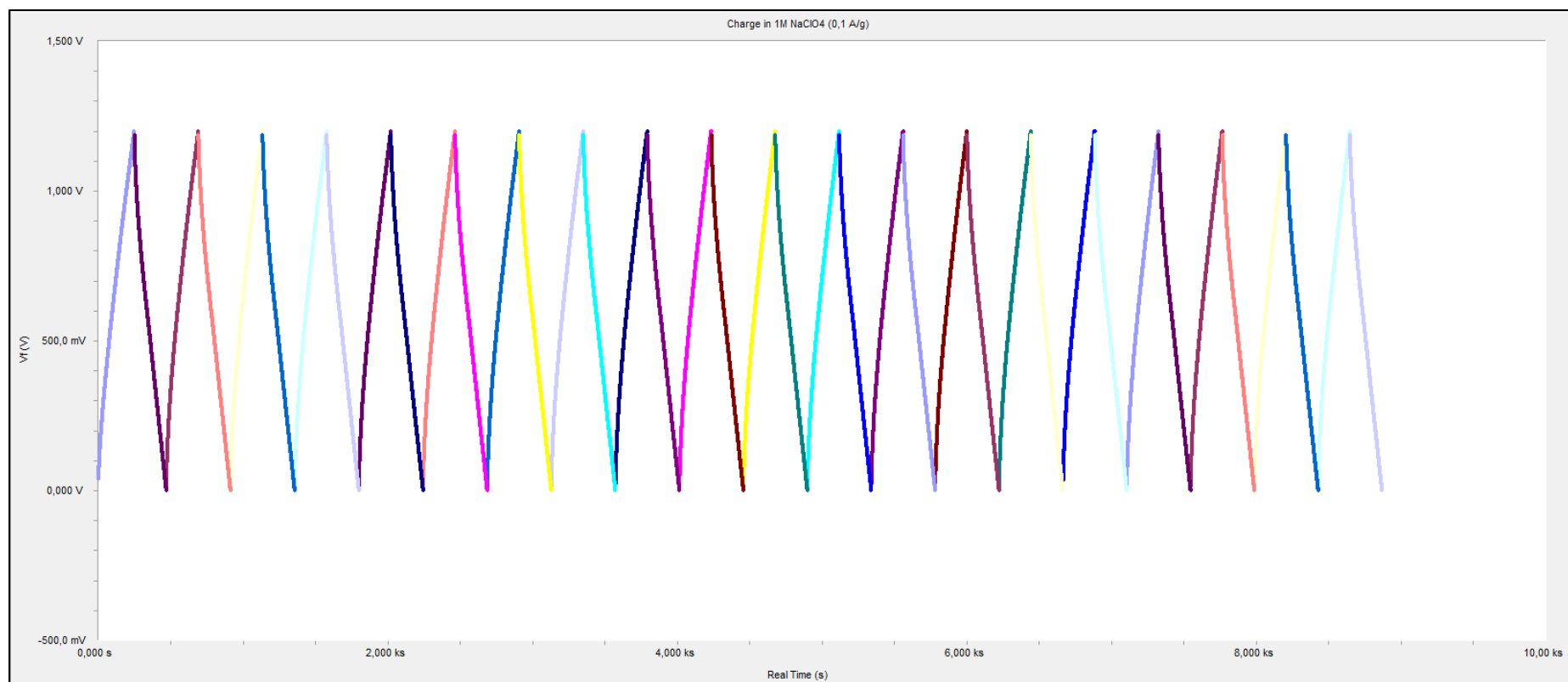


Figure A - 19. Representative GCD profile illustrating the repeatable charge-discharge cycles. Twenty (20) cycles were conducted. The experiment used in this figure was the GCD of G-CNC Batch 31 electrodes (average mass load = 2.7 mg).

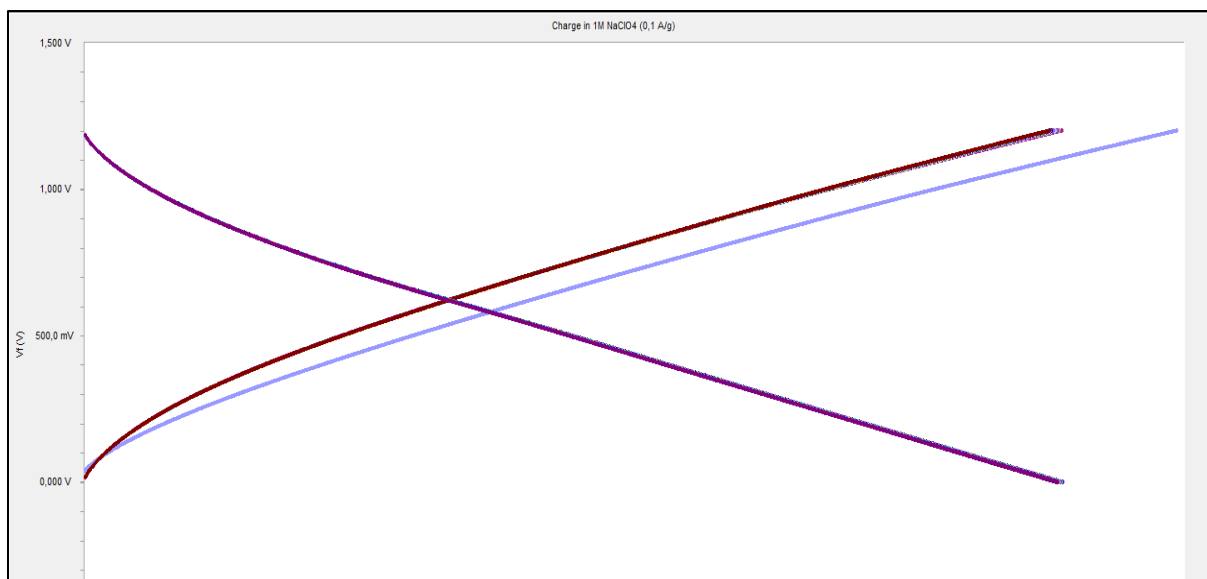


Figure A - 20. The GCD profile of the same experiment used in Figure A - 19, expressed as cell potential (V) vs. time (s). It is shown in this figure that the charge-discharge times remains consistent after the first cycle (First charging cycle shown in purple).

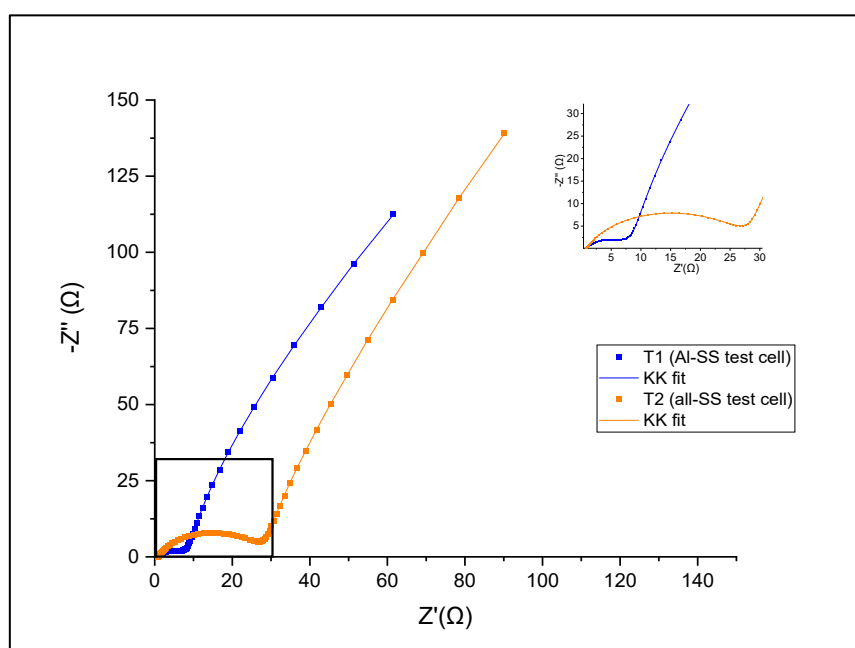


Figure A - 21. Nyquist plots for the two replicate measurements of G-CNC Batch 19 electrodes, showing the variations in R_{ct} between the replicates due to differences in the test cell and the amount of 1.0 M NaClO_4 . The inset shows a close-up image of the high-frequency impedance values and their corresponding Kramers-Kronig (KK) fits. Measurements were taken after the GCD test. Last data point corresponds to $f = 0.1$ Hz.

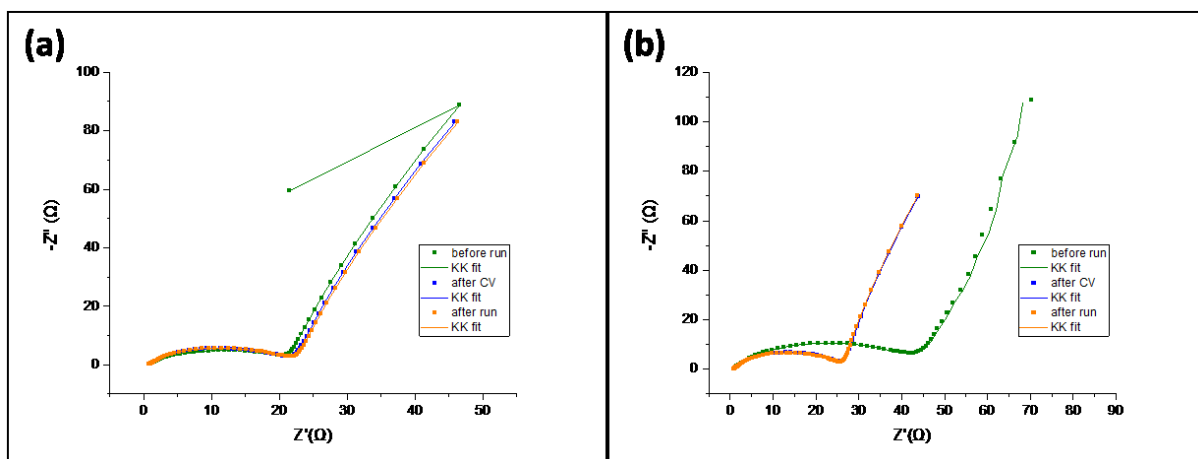


Figure A - 22. Nyquist plots at different stages of the electrochemical measurements for G-CNC Batch 31 electrodes. The two replicate measurements are shown in this figure separately due to average mass loading differences (a – 2.7 mg G-CNC b – 13.7 mg G-CNC). The last data points correspond to $f = 0.1$ Hz.